Friedrich-Alexander-Universität
Naturwissenschaftliche Fakultät

Master's Thesis
in Physics

Optimization of a Dark-Field CT setup for detecting cancerous breast tissue

Markus Kraft

Supervisor: Prof. Dr. Stefan Funk

Erlangen Centre for Astroparticle Physics

Submission date: 01.06.26

Contents

1 Introduction

Breast cancer is the leading cancer diagnosis among women globally, making reliable early detection a crucial factor in reducing mortality rates [Wor26]. The number of new cases increases each year, while the mortality rate slightly decreases [SMJ19], which is mainly due to improvements in treatments and early detection of breast cancer. The earliest signs of non-palpable breast cancer are calcifications, which are commonly associated with ductal carcinoma in situ (DCIS) and can also occur in invasive breast cancer [SMJ19]. However, conventional attenuation-based X-ray imaging is limited in visualizing very small or weakly absorbing calcifications. Grating-based X-ray imaging offers a promising addition by providing the dark-field modality. The dark-field signal originates from small-angle scattering, resulting in a sensitivity to microstructures much smaller than the spatial resolution of the imaging system, enabling a improved detection of features such as microcalcifications [Pfe+08]. Earlier investigations at the Erlangen Centre for Astroparticle Physics (ECAP) showed promising applications of dark-field imaging in breast diagnostics [Ant+13; MRA+13]. Anton et al. demonstrated that dark-field imaging is sensitive to micrometer-sized calcium phosphate grains, which enables improved visualization of tumor regions and provides quantitative information about the underlying microstructure. Michel et al. showed that micrometer-sized calcifications in the human breast, which are not visible in conventional X-ray mammography at diagnostic dose levels, can still generate a significant dark-field signal under the same imaging conditions. More recently, Aminzadeh et al. demonstrated a more distinct detection of microcalcifications in dark-field images compared to absorption images, as well as a more precise determination of their shape, size, and distribution [Ami+22]. This thesis contributes to the advancement of grating-based dark-field Computed Tomography (CT) through the optimization and evaluation of dark-field CT measurements on cancer samples embedded in formalin and paraffin. First, the acquisition parameters and signal quality in the form of the visibility of dark-field projections were systematically investigated. This includes parameters such as tube voltage, focal spot size, frame time, and phase-stepping configurations. Furthermore, CT parameters such as angle step size, angle sector, and filters were investigated for different grating setups. Measurements were first evaluated using phantoms, and, subsequently, dark-field CT measurements were performed on formalin-fixed and paraffin-embedded cancer samples provided by the "Pathologie Uniklinikum Erlangen". The reconstructed dark-field and transmission signals of the formalin-fixed samples were compared, and for the paraffin-embedded samples were correlated with histological Von-Kossa-stained sections.

The clinical use of dark-field CT in screening is currently limited by system size, scan time, and radiation dose, whereas intraoperative applications appear to be more promising. One such application of the dark-field CT could be the evaluation of the surgical margin during tumor resection, improving verification of complete tumor removal and potentially reducing the need for repeat surgery. By correlating histological DCIS calcifications with dark-field and transmission CT on paraffin-embedded cancer samples, this work provides a basis for future investigations of calcifications using grating based interferometry.

2 Theoretical Background

This chapter introduces the theoretical foundations underlying the imaging methods used in this thesis. First, the fundamental properties of X-rays and their interaction with matter are explained. Building on this, the principles of grating-based X-ray imaging are outlined, including the different imaging modalities attenuation, phase-contrast, and Dark-field. In addition, the basis of computed tomography (CT) is introduced, including data acquisition, reconstruction methods, and commonly used filters. Furthermore, another time optimized acquisition method, namely interlaced, is explained as well as the properties and advantages of the used photon-counting detector.

2.1 Fundamentals of X-rays

X-rays are high-energy electromagnetic waves characterized by short wavelengths and photon energies typically in the keV range. In matter, X-rays can interact via several energy-dependent mechanisms, including photoelectric absorption, Compton scattering, and elastic (Rayleigh) scattering [Mus+88]. The measurement of the energy deposition and phase shift in matter is the basis of signal generation in both attenuation and grating-based imaging.

2.2 X-ray Generation and Properties

In conventional X-ray tubes, photons are generated by high-energy electrons that interact with a metallic anode. The electrons emitted from a heated cathode are accelerated by an applied voltage U_B towards the anode. The anode material determines the X-ray spectrum. A commonly used material is tungsten, while in applications such as mammography molybdenum or rhodium are also used [KS+97]. At the anode, electrons either decelerate in the Coulomb field of the nuclei, producing Bremsstrahlung, or ionize atoms, resulting in characteristic emission lines through subsequent electronic transitions in the shell. As a consequence, Bremsstrahlung leads to a continuous spectrum, while characteristic radiation adds discrete spectral lines [Mus+88]. The energy range of the spectrum is determined by the applied voltage as it sets an upper limit for the kinetic energy of the electrons. Medical X-ray tubes typically use peak voltage ranges from 25 kVp to 150 kVp [Lud20]. Consequently, their maximum photon energy can be calculated as

$$E_{\mathrm{max}} = e\,U_B, \tag{1}$$

where e is the elementary charge. The photon energy is related to its wavelength λ by the Planck's law

$$E = h\nu = \frac{hc}{\lambda}, \tag{2}$$

with h denoting Planck's constant, ν the frequency, and c the speed of light. Hence, this voltage range corresponds to maximum photon energies from 25 keV to 150 keV, which in turn has wavelengths of about 50 pm to 8 pm, respectively.

2.3 Interaction of X-rays with Matter

X-rays propagating through matter undergo different interaction processes with the atoms of the medium, depending on their energy. These processes are the photoelectric effect, Compton scattering, and elastic (Rayleigh) scattering, while pair production is negligible in the energy range relevant for medical and grating-based X-ray imaging. The relative contribution of these processes is determined by the photon energy, and the atomic number and density of the material [Mus+88]. At low photon energies and for high-Z materials, the photoelectric absorption dominates. At higher energies, Compton scattering becomes increasingly relevant. Elastic Rayleigh scattering is most prominent at low energies and in low-Z materials. Electron-positron pair production can only occur at photon energies above 1.022 MeV and therefore is not relevant for this work [Mus+88]. The relevant interactions are explained in more detailed in the following.

Photoelectric effect. For low-energy photons, the photoelectric effect is the dominant interaction. In this process, a bound electron from the i-th shell absorbs the photon and is ejected with the kinetic energy

$$E_{\mathrm{kin,e}} = E_\gamma - E_{\mathrm{binding,\,i}}, \tag{3}$$

where E_γ is the photon energy and $E_{\mathrm{binding,\,i}}$ the electron binding. The effect requires bound electrons, since free electrons cannot absorb a photon while conserving momentum. The resulting vacancy is then filled by an outer-shell electron, releasing the binding-energy difference. The cross section σ_{Photo} scales strongly with the atomic number Z and photon energy as follows

$$\sigma_{\mathrm{Photo}} \propto \frac{Z^a}{E_\gamma^{7/2}}, \tag{4}$$

where a is the influence of the Z dependence and can have values depending on the material between 3 to 5. Consequently, the photoelectric effect dominates in the keV range, and in materials with a high atomic number Z [Pov+14; Mus+88].

Compton effect. The Compton effect describes the inelastic scattering of photons on quasi-free atomic electrons. The electron can be treated as free, since the photon energy is much larger than the electron binding energy, and part of the photon's energy and momentum is transferred to the electron. The scattered photon emerges with reduced energy $E_{\gamma'}$ as described with [Mus+88]

$$E_{\gamma'} = \frac{E_\gamma}{1 + \frac{E_\gamma}{m_e c}\left(1 - \cos(\Phi)\right)}, \tag{5}$$

where Φ is the scattering angle. As such, the energy loss of the photon also depends on the scattering angle, which is minimal for small angles and maximal for backward scattering, i.e. $\Phi = 180$. The cross section scales approximately as

$$\sigma_{\mathrm{Compton}} \propto \frac{Z}{E_\gamma} \ln E_\gamma. \tag{6}$$

The total linear attenuation coefficient $\sigma_{\mathrm{Compton}}$, can be decomposed into a Compton absorption coefficient $\sigma_{\mathrm{Compton},a}$, which describes the photon energy deposited in the medium through secondary electrons, while the Compton scattering coefficient $\sigma_{\mathrm{Compton},s}$ represents the scattered photons out of the beam [Pov+14; Mus+88].

Rayleigh Scattering. Rayleigh scattering describes elastic scattering of X-ray photons by bound electrons of an atom. Therefore, the photon only changes its direction slightly, but without losing energy. This scattering is coherent and a form of small-angle scattering, whose average scattering angle increases for lower photon energies. The probability of Rayleigh scattering decreases as the photon energy increases. Its cross-section σ_{Rayleigh} scales with Z^2 to Z^3, while for photon energies above 10 keV roughly follows E^{-2} [Kri12; Mus+88]. Hence, Rayleigh scattering is more pronounced in high-Z materials and can give contrast between structures such as bone and soft tissues. Since Rayleigh scattering minimally contributes to attenuation it is often neglected in conventional X-ray imaging, but as it is a form of coherent, small-angle scattering, it contributes to the contrast produced in Dark-field imaging, which is discussed in Chapter 2.5.3.

Linear Attenuation Coefficient

In conventional X-ray imaging, only the total attenuation of the radiation passing through a medium can be measured. The transmitted intensity through a homogeneous medium of thickness z is described by the Beer-Lambert law [Mus+88]

$$I(z, E) = I_0(E) \exp\bigl(-\mu(E)\, z\bigr), \tag{7}$$

where I_0 the initial intensity, $I(z, E)$ the transmitted energy, and $\mu(E)$ is the energy-dependent linear attenuation coefficient. This coefficient contains the effects of all interaction processes for a specific photon energy, as in conventional X-ray imaging they cannot be separated. The mass attenuation coefficient $\mu_m = \mu/\rho$ can also be used to express the attenuation normalized on the density of the material ρ. Also, the linear attenuation coefficient is closely related to the cross-section of interactions by the number density n as [Mus+88]

$$\mu(E) = n\sigma(E). \tag{8}$$

Therefore, for a specific material they are connected by a constant. Figure 1 shows the energy dependence of the cross-sections and the contribution of the photoelectric effect, Compton scattering, and Rayleigh scattering for the example of water. This illustrates that for low energies, the photoelectric effect is the dominant interaction and for higher energies Compton scattering becomes the increasingly more dominant process.

2.4 Complex Refractive Index of X-rays

The interaction processes of X-rays with matter can be encapsulated by the complex refractive index n, which gives a unified description of attenuation and phase-shifting effects. The complex refractive index can be defined as [Gre08]

$$n = (1 - \delta + i\beta), \tag{9}$$

where $1 - \delta$ and β are energy- and material-dependent quantities and represent the real and imaginary parts of the refractive index, respectively. Then X-rays propagating through a material can be described by an electromagnetic wave in a dielectric material with a complex refractive index as

$$\left(\frac{n^2}{c^2}\frac{\partial^2}{\partial t^2} - \nabla^2\right)\Psi = 0. \tag{10}$$

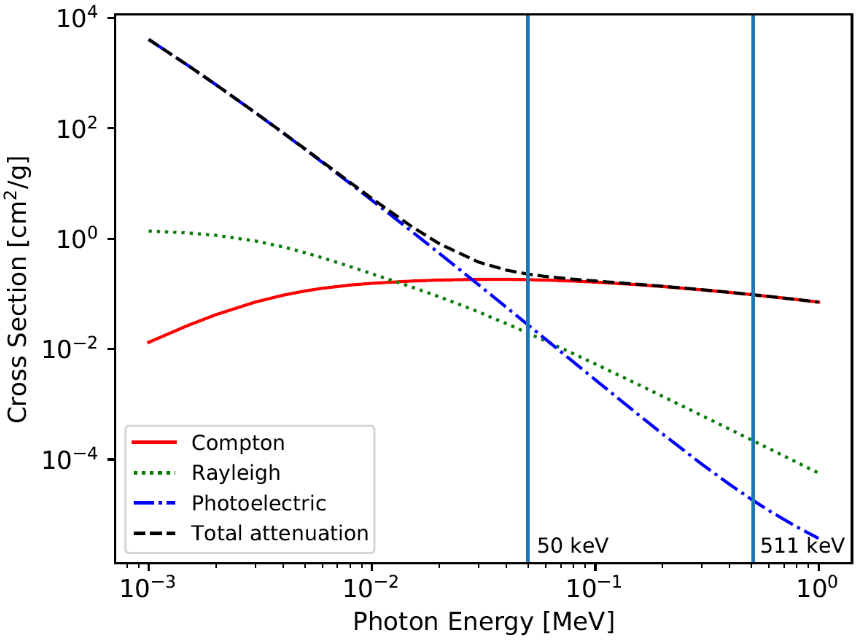

Figure 1: Energy-dependent cross-sections for the photoelectric effect, Compton scattering, and Rayleigh scattering in liquid water, together with the resulting total attenuation coefficient. Depending on the energy, either photoelectric absorption or Compton scattering is the dominant process. Marked with blue lines are 50 keV and 511 keV, where Compton scattering is more dominant at 511 keV then as 50 keV [BS23].

To solve this wave equation, a plane wave ansatz $\Psi(\vec{r}, t)$ at position $\vec{r}$ and time t of the form

$$\Psi(\vec{r}, t) = \Psi_0 \cdot \exp\left(i(\vec{k} \cdot \vec{r} - \omega t)\right) \tag{11}$$

can be used, where ω is the frequency, $\vec{k}$ is the vacuum wave vector, Ψ_0 is the initial amplitude. The wave vector in a medium $\vec{k}_n$ can then be written by modifying vacuum wave vector $\vec{k}$ with the refractive index as

$$\vec{k}_n = \vec{k}n = \vec{k}(1 - \delta + i\beta). \tag{12}$$

Substituting the vacuum wave vector $\vec{k}$ in Equation 11 and assuming propagation in z-direction as $\vec{k} = k_z$ results in:

$$\begin{aligned} \Psi(z, t) &= \Psi_0 \cdot \exp[ik_z z(1 - \delta + i\beta) - i\omega t] & (13) \\ &= \Psi_0 \cdot \underbrace{\exp[i(k_z z - \omega t)]}_{\text{vacuum propagation}} \cdot \underbrace{\exp(-i\delta k_z z)}_{\text{phase shift}} \cdot \underbrace{\exp(-\beta k_z z)}_{\text{attenuation}}. & (14) \end{aligned}$$

This shows directly that the δ term causes a phase shift, while the β term causes an exponential damping. This formulation also allows to derive the Lambert-Beer law as the intensity is the wave function squared

$$I(z) = |\Psi(z, t)|^2 = \Psi_0^2 \cdot \exp(-2\beta k_z z) \tag{15}$$

Comparison to the Lambert-Beer law yields a relation of β and the linear attenuation coefficient μ

$$\mu = 2\beta k_z. \tag{16}$$

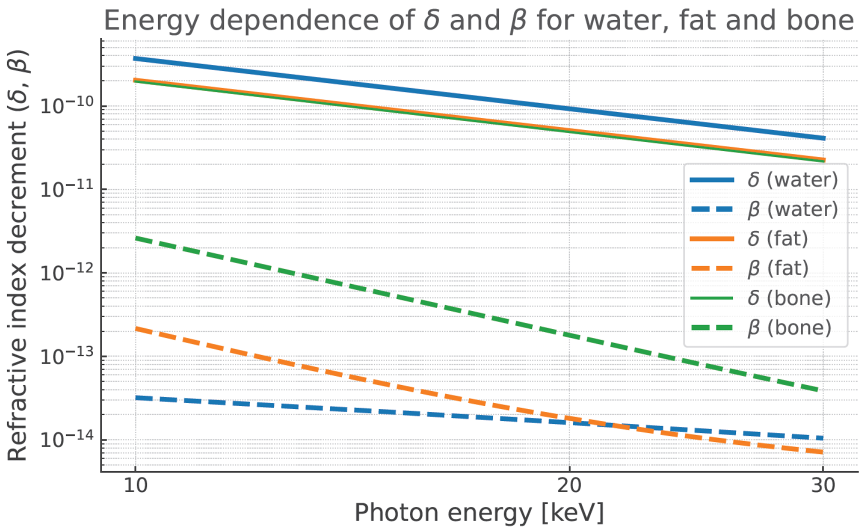

Figure 2: Refractive index decrements δ and β in dependence of photon energy for water, fat, and cortical bone. Solid lines represent the refraction index δ, dashed lines represent absorption index β [Fri25].

The phase shift introduced by propagating through matter is

$$\Delta\Phi = -\delta k_z z. \tag{17}$$

Therefore, the phase shift only depends on the material specific refractive decrement δ and the thickness of the medium. Since this term has a negative sign, the wavefront is shifted forward along the direction of propagation.

Energy and Material Dependence of β and δ

Both the refractive index decrement δ and the absorption index β feature a strong dependence on the X-ray energy and the material composition. Generally, both quantities decrease with increasing photon energy, but their exact behavior underlies the atomic number and density of the material. Typically, materials with higher atomic numbers have larger values of β, which results in a stronger absorption[HGD93]. The difference of those values between two materials forms the basis of X-ray imaging. In Figure 2 the energy dependence of δ and β for water, fat and bone is illustrated. This shows a strong absorption contrast between fat and water at photon energies of 10 keV, while at approximately 22 keV, fat and water yield nearly identical absorption.

2.5 Grating-Based X-ray Imaging

Standard X-ray imaging only measures the attenuation of X-rays propagating through an object, providing a contrast based on differences in material absorption. A Talbot-Lau interferometer can extend conventional attenuation-based methods by exploiting the interference of X-rays to measure the changes in the wavefront. This enables simultaneous acquisition of attenuation, differential phase-contrast, and dark-field signals from the same acquisition [Pfe+08]. These additional image modalities provide

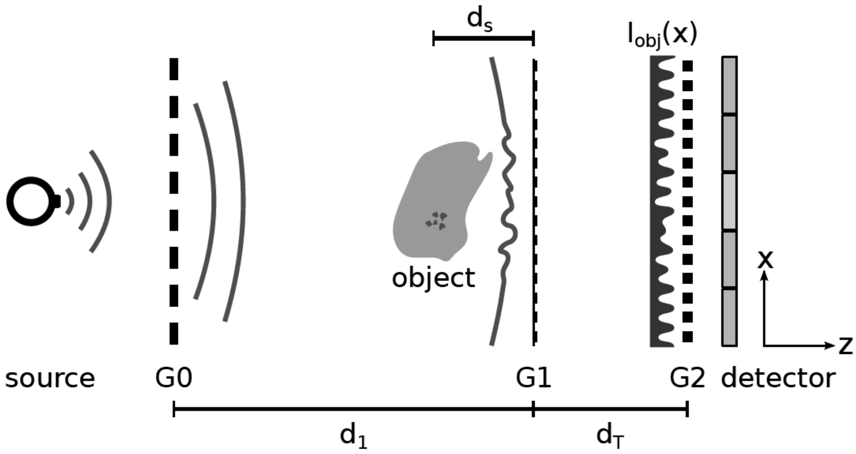

Figure 3: Setup principle of a Talbot-Lau interferometer with S X-ray source, G_0 source grating, G_1 phase grating, and the G_2 analyzer grating and D detector [Lud20].

additional information, particularly in samples with fine microstructures, and soft-tissue. This section introduces the working principle of a Talbot-Lau interferometer, the phase-stepping method to acquire projections, and the signals measured in each image modality.

2.5.1 Talbot-Lau Interferometer

A Talbot-Lau interferometer allows phase-sensitive X-ray imaging even with incoherent X-ray sources such as X-ray tubes. This is achieved by adding three gratings, that each have a separate function. The gratings are named G_0 source grating, G_1 phase grating, and the G_2 analyzer grating. Combined, they create an interference pattern that is sensitive to attenuation, phase shifts and small-angle scattering in the sample. A sketch of the full Talbot-Lau interferometer geometry is shown in Figure 3, including the X-ray source S the, gratings (G_0,G_1,G_2) and the detector.

Talbot Effect and the Phase Grating The Talbot effect describes the self-imaging of a periodic phase structure under coherent wavefronts [Tal36]. A wavefront passing through the phase grating, creates a periodic intensity patterns at the Talbot distances z_T. These Talbot distances are discrete propagation distances at which near-field diffraction produces self-images through interference. The first Talbot distance can be calculated as [Ray81]

$$d_{T1} = \frac{2p^2}{\lambda} \quad \lambda << p \tag{18}$$

where d_{T1} is the Talbot distance, and p is the grating period. This relation only holds in first order for small wavelengths in comparison to the grating period. As the G_1 is a phase grating, it introduces a spatially periodic phase modulation onto the incoming wavefront, while not attenuating the radiation in the ideal case. This phase shift depends on the grating height and the photon energy, where usually a π- or $\pi/2$-shifting grating is chosen for a specific design energy. In medical imaging those are especially preferred over absorption gratings as they do not impose an unnecessary loss in dose after a

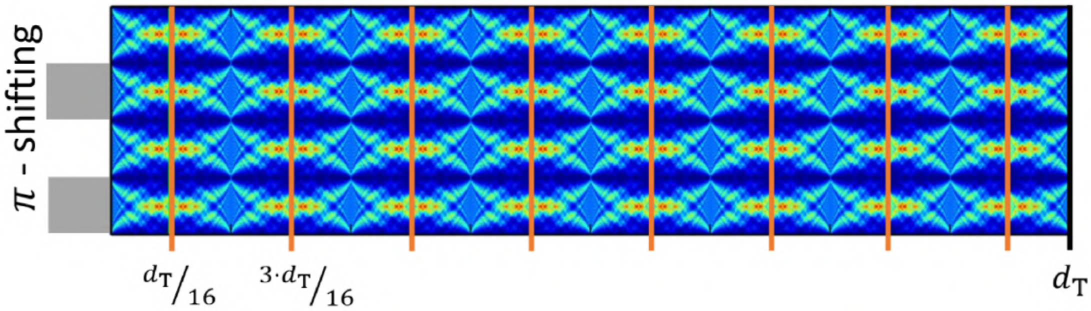

Figure 4: Simulated Talbot carpet for a π-shifting phase grating caused by by monochromatic illumination. A periodic intensity pattern along the propagation direction is visible. The orange lines indicate the fractional Talbot distances given by Equation 20, yielding high contrast fringes due to near field interference [Fri25; Sch20; Wol16].

patient compared to the also available absorption grating. Often a π-shifting grating is preferred as it exhibits frequency doubling causing Talbot patterns to occur in smaller distances behind the grating [Lud20]. As an additional parameter, the grating geometry is characterized by its duty cycle $D_c = w/p$, where w denotes the gap width and p the grating period. To maximize fringe contrast, the duty cycle is typically set to $D_c = 0.5$. At integer Talbot distances the phase grating reproduces a uniform intensity distribution without observable modulation [YVM15]. Only at specific fractional Talbot distances d_T^f high-contrast interference fringes are produced, which are different according to the grating type. For a $\pi/2$-shifting grating, usable high-contrast fringes appear at distances [YVM15]

$$d_T^f = \frac{2m-1}{4} \cdot d_{T1}, \qquad m \in \mathbb{N}, \tag{19}$$

where m is the order of the fractional Talbot distance. For a π-shifting grating, usable high-contrast fringes appear at distances [YVM15]

$$d_T^f = \frac{2m-1}{16} \cdot d_{T1}, \qquad m \in \mathbb{N}. \tag{20}$$

The simulated Talbot carpet for such a π-shifting grating in shown in Figure 4. At the full Talbot distance a self-image is formed, whereas at fractional Talbot distances high-contrast interference fringes appear.

Lau Effect and the Source Grating The source grating only serves to turn the spatially incoherent radiation produced in conventional X-ray tubes into coherent light. To this end, the Lau effect is exploited, where a grating subdivides the beam into an array of narrow, mutually coherent line-sources [Lau48]. Each of these line-sources can form its own Talbot pattern downstream. For the individual patterns to overlap constructively, the system geometry has to satisfy the condition given by the intercept theorem

$$\frac{p_0}{p_T} = \frac{d_{0,1}}{d_T}, \tag{21}$$

where p_0 is the period of G_0, p_T the period of the self image of the G_1, $d_{0,1}$ the distance between G_0 and G_1, and d_T the Talbot distance [Pfe+06].

Moiré Pattern and Analyzer Grating As the grating periods have sizes of a few microns, their Talbot pattern has the same size, but due to the increased propagation distance it is affected by a magnification. As a result, typical X-ray detector pixel sizes of several tens of micrometers cannot resolve the Talbot pattern. Therefore, to detect the interference pattern, the analyzer grating G_2 is used at exactly a fractional Talbot distance d_T^f downstream of G_1. Through the superposition of the Talbot pattern and the G_2 a moiré pattern can arise. The moiré pattern is formed when two periodical patterns, which have a slightly different period or a relative tilt angle, superimpose. The moiré pattern then allows for an indirect detection of the intensity modulation, so that the attenuation, differential phase, and Dark-field can be determined using the phase-stepping technique explained in Chapter 2.5.2. These additional modalities can be measured, as refraction within the sample causes a shift of the moiré patten, while small-angle scattering causes a local reduction in its fringe visibility.
The period of the moiré pattern p_M can be calculated using by

$$p_M = \frac{p_2\, p_T}{\sqrt{p_2^2 + p_T^2 - 2p_2 p_T \cos\alpha}}, \tag{22}$$

where p_2 is the period of G_2, p_T the period Talbot pattern, and α the relative tilt angle [**Amidror2009moir**]. Those fringes can be adjusted to have periods of hundreds of microns, thus cover multiple pixels and can be well differentiated in a detector. The strength of the moiré fringes, which corresponds to the signal quality of the setup, is defined by the visibility V as

$$V = \frac{I_{\max} - I_{\min}}{I_{\max} + I_{\min}}. \tag{23}$$

2.5.2 Phase-Stepping Technique

Using the phase-stepping technique, the changes in the interference pattern can be extracted by measuring the moiré pattern at several phase-steps. A phase-step is the translation of either grating G_0 or G_2 in discrete steps, where multiple phase-steps over at least one grating period build a phase-stepping scan. At each step, an image is acquired, and the intensity recorded for every detector pixel. Hence, a phase-stepping scan gives the intensity as a function of the grating position for each pixel. The stepping of G_0 and G_2 is mathematically equivalent, as only the relative phase between the interference pattern and the analyzer grating is relevant. In this work, the source grating G_0 is stepped. For a monochromatic point source and perfect gratings, the measured intensity curve has the form of a triangular shape. However, a finite source size and the polychromatic spectrum result in a blurring of the interference pattern, which can be well approximated by a sinusoidal function

$$I(x) = \bar{I} + A \sin\bigl(2\pi x + \Phi\bigr), \tag{24}$$

where x is the position of the grating normalized by its period, $\bar{I}$ the mean intensity, A the amplitude, and Φ the phase. This fit of the measured intensity curves for each pixel yields the parameters $\bar{I}, A$, and Φ. To measure the changes caused by an object, an object scan and a reference scan or flat-field measurement have to be performed. The changes of those parameters then yield separate corresponding image modalities. An example of a fitted object and reference curve is shown Figure 5.

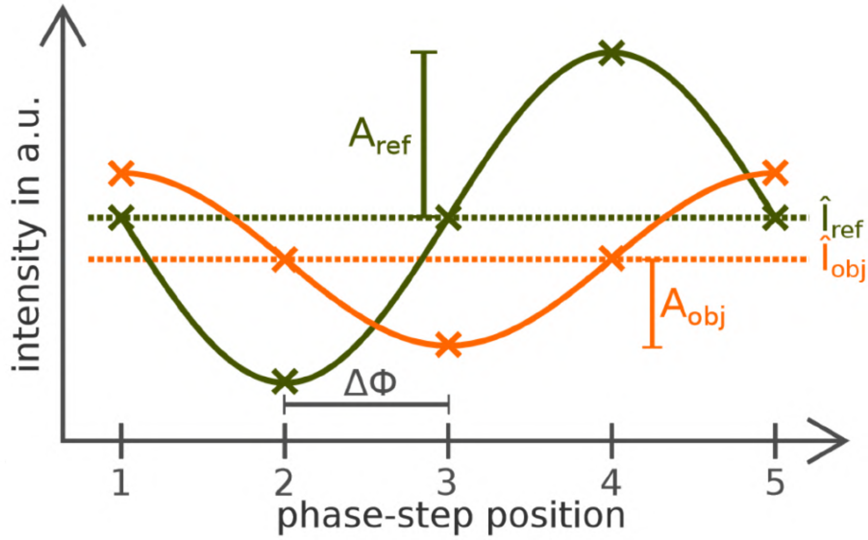

Figure 5: Intensity of the object and reference scan at different phase-step positions and fitted with the sinusoidal function to extract their amplitude mean intensity and relative phase-shift [Lud20].

2.5.3 Signal Modalities: Attenuation, Phase, Dark-Field

Attenuation image The attenuation image represents the damping of the X-ray waves. As such, it can be calculated by the reduction of the mean intensity $\bar{I}$ of the object phase-stepping scan. It is defined as

$$\Gamma = -\ln\left(\frac{\bar{I}_{\text{obj}}}{\bar{I}_{\text{ref}}}\right) =: \mu. \tag{25}$$

This image corresponds to the one obtained in conventional X-ray imaging. Depending on the material, particular Z, and thickness more X-rays are absorbed, creating a contrast that is particularly sensitive to materials with different Z. In medical X-ray imaging the absorption caused by the photoelectric effect is the main measured signal, as the strong dependence on the atomic number of the photoelectric effect allows for a good differentiation between bone-like material ($Z_{\text{Ca}} = 20$) and the surrounding soft tissue ($Z_{\text{tissue}} \approx 7$).

Differential phase image The difference of the obtained phases of object to reference phase-stepping curve yields the differential phase image as

$$\Delta\Phi = \Phi_{\text{ref}} - \Phi_{\text{obj}}. \tag{26}$$

The phase shift is caused by the refraction of X-rays at material interfaces within the object. As the wavefront propagates through regions of different thickness or composition, it is slightly deflected, which produces a measurable shift in the interference fringes of the phase-stepping curve. The differential phase is directly related to the refractive index decrement $\delta(z)$ of the complex refractive index and can be expressed as [Lud20]

$$\Delta\Phi_{\text{abs}} \approx \frac{2\pi d_T}{p_T}\,\partial_x \int_0^s \delta(z)\,dz, \tag{27}$$

where s is the path length through the material, ∂_x is the derivative along the phase-stepping direction, p_T is the grating period, and d_T the distance between the phase grating and the detector. Since δ is proportional to the electron density and more sensitive to small variations in low-Z materials than the absorption coefficient β, differential phase imaging highlights subtle structural features, such as soft-tissue or air boundaries, which are often invisible in conventional attenuation images [Pag06]. In this study, the differential phase images are recorded but not further analyzed.

Dark-field image and visibility The dark-field image results from the relative reduction in visibility V of the measured intensity curve. The visibility for a sinusoidal phase-stepping curve with $I_{\max} = \bar{I} + A \quad$ and $\quad I_{\min} = \bar{I} - A$, is defined by

$$V = \frac{I_{\max} - I_{\min}}{I_{\max} + I_{\min}} = \frac{A}{\bar{I}}. \tag{28}$$

The dark-field signal Σ is then defined as

$$\Sigma = -\ln\left(\frac{V_{\text{obj}}}{V_{\text{ref}}}\right) = \ln\left(\frac{A_{\text{obj}} \cdot \bar{I}_{\text{ref}}}{A_{\text{ref}} \cdot \bar{I}_{\text{obj}}}\right). \tag{29}$$

As a quality parameter for Dark-field imaging, the reference visibility can be directly taken, as high reference visibility allows more pronounced reductions in the object visibility. This reduction is mainly caused by very small structures inside the object that cannot be directly resolved by the imaging system. Microstructures such as fibers, pores, or granular structures do not cause significant absorption or refraction, but rather cause ultra-small-angle scattering. This causes slight angular deviations of the wavefront, which locally blurs the moiré pattern and reduces visibility. This makes dark-field imaging particularly sensitive to micro-structures that remain undetectable in conventional attenuation or phase-contrast images.

Dark-field sensitivity and correlation length

Next to the visibility there is another main parameter influencing the image quality, which is the sensitivity. The sensitivity of a Talbot-Lau setup describes the degree, where deviations in the wavefront are measurable, whereas the visibility describes the signal quality. For the Dark-field image this specifically means the small-angle scattering originating from microscopic structures within the sample, which can also be interpreted as unresolved phase shifts or small-angle scattering contributions [Lyn+11]. This sensitivity is not solely dependent on the micro-structure size, but also strongly depends on system geometry and setup parameters such as the X-ray wavelength, grating periods, and propagation distances[Koe+16].
The Dark-field signal sensitivity can be described with the correlation length, which for a sample-grating configuration is

$$\xi = \frac{\lambda d_T}{p_T}\left(1 - \frac{d_{s,1}}{d_{0,1}}\right), \tag{30}$$

where λ is the wavelength, d_T the Talbot distance, p_T the Talbot period, $d_{s,1}$ the distance between sample and G_1, and $d_{0,1}$ the distance between the G_0 and G_1[Str14]. From this correlation length the dark-field signal can be linked to the real-space correlation

function of the sample and, equivalently, to a macroscopic scattering cross section. As the correlation length determines the signal strength of specific structures, by tuning the correlation length scattering structures with different sizes, shapes, and volume fractions can be characterized [Str14].
The sensitivity of the dark-field imaging can be increased primarily by reducing the sample to G_1 distance $d_{s,1}$. However, the maximum sensitivity is limited by the Talbot distance d_T and the grating period p_2, as p_2 equals the at distance d_T magnified period of the Talbot pattern, yielding

$$S_{\max} = \lambda \frac{d_T}{p_2}, \tag{31}$$

for the case where the sample is placed as close as possible to the first grating $d_{s,1} = 0$. However, d_T also affects fringe visibility, so in practice a compromise must be found between sensitivity, visibility, and geometric constraints of the imaging setup [Lud20].

Medical applications of Dark-field imaging Dark-field imaging having a sensitivity to structures below the spatial resolution of the imaging system gives advantages in several applications and allows the use of X-ray imaging in new fields.
One important application of dark-field image is in medical imaging, especially in breast imaging. There a crucial focus is the detection of microcalcifications, which are tiny calcium deposits that can indicate the presence of breast cancer. These structures often have sizes of only a few micrometers, so that they may not produce sufficient attenuation contrast in conventional mammography. For mammography, it has already been shown that Dark-field imaging provides additional structural information beyond standard attenuation imaging [MRA+13; Ant+13]. Specifically, Michel et al. demonstrated that some microcalcifications produce a strong dark-field signal because of their fine internal microstructure, which were invisible in the conventional attenuation image at comparable radiation dose levels [MRA+13]. Another promising application for Dark-field imaging is lung diagnostic, as the alveolar microstructure of healthy lung tissue causes strong ultra-small-angle scattering, which results in a dark-field signal. Hellbach et al. demonstrated that the severity of acute lung injury due to inflammation in mice can be clearly visualized using Dark-field imaging, whereas those changes in attenuation X-ray imaging often are to weak to detect. Further, unlike the Dark-field signal the attenuation signal also depends greatly on the overlying chest wall [Hel+18].

Linear Diffusion Coefficient Analogous to the linear attenuation coefficient quantifying the X-ray absorption, the visibility loss causing the Dark-field signal can by quantified by the linear diffusion coefficient ϵ [Bec+10]. As such, it is a material-specific property that describes the scattering strength per unit length. The linear diffusion coefficient depends on the standard deviation σ of the angular scattering distribution $A(\theta)$, which depends on the material and its slice thickness Δz, and can be defined as

$$\epsilon = \frac{\sigma^2}{\Delta z}. \tag{32}$$

Consequently, the scattering width along a beam path is

$$\sigma^2 = \int \epsilon(z)\, dz. \tag{33}$$

For a Gaussian scattering distribution, the visibility loss can be expressed as

$$V = \exp\left(-\frac{2\pi^2 d_{1,2}^2}{p_2^2}\int \epsilon(z)\,dz\right), \tag{34}$$

where p_2 is the period of the G_2 and $d_{1,2}$ the distance between the phase grating G_1 and the analyzer grating G_2. This shows an exponential decrease for a linear increased scattering strength [Bec+10]. Since conventional CT reconstructions spatially resolve the linear absorption coefficient through the intensity loss along the entire X-ray path through the object, Equation 34 allows an analogous spatial reconstruction of the diffusion coefficient using Dark-field images.

2.6 Computed Tomography

Computed tomography (CT) is an invaluable tool for the nondestructive investigation of objects belonging to life, environmental, and in material sciences. CTs allow for the reconstruction of a three-dimensional representation of an object from multiple X-ray projections acquired at different angles through computational processing. The following subsections outline acquisition geometry, detector technology, reconstruction methods, common used filters, and typical artifacts.

Acquisition Geometry

For computed tomography systems projection data from multiple viewing angles has to be acquired. For those, only the relative rotation of the sample to the X-ray source and detector is needed. As such, In clinical CT setups, the X-ray source and detector are mounted on a gantry that rotates around the patient, which allows for a still standing patient/sample, and a fixed angle between the source and detector, that allows for rapid data acquisition. In CT systems such as the one used in this work, a fixed source-detector setup is employed, while the sample is rotated stepwise or continuously to obtain the projections at each angle. This allows a more compact and simpler mechanical implementation of the CT. Additionally, For proper CT reconstruction, projections over at least angle sector of $a_{\text{sector}} = 180°$ have to be recorded, to achieve a full sampling the object [Tra22]. By increasing the number of projections within the angle sector the sampling density is increased, which improves the spatial resolution of the reconstructed object. In this work a setup with a rotating sample is used, which allows an easier implementation of the Talbot-Lau interferometer and a flexible adjustment its parameters.

Radon Transform

The measured projection data of a CT can be described analytically using the Radon transform. For this, only the set of projections of a single detector row, e.g. a projection line, corresponding to a two-dimensional reconstructed area is considered. Then the absorption coefficients of the object to reconstruct can be expressed as an object function $f(x, y)$. For simplicity, a single X-ray beam corresponds to a pixel. The beam propagates through the object along a straight line, and the pixel measures the accumulated attenuation along the ray path. A projection line is then parameterized by the line equation

$$x \cos\theta + y \sin\theta = t \tag{35}$$

where θ is the projection angle and t the detector position. Here, a pixel would correspond to a discrete value of t, but t itself is continuous. The detector value measured $Rf(t, \theta)$ corresponds to the line integral of the object function along this path. Consequently, the Radon transform of $f(x, y)$ can be defined as [Rad17]

$$Rf(t, \theta) = \int_{x \cos\theta + y \sin\theta = t} f(x, y)\, d\ell \tag{36}$$

where $d\ell$ denotes integration along the X-ray line. To obtain a complete representation of the object in the projection space, additional projections form each projection angle θ_i are needed. This representation is commonly called a Sinogram, as it transforms a single point object into a sinusoidal curve in projection space [Rad17; KS01].

Fourier Slice Theorem

Analytical reconstruction methods in CT are based on the Fourier Slice Theorem, which yields the relationship between projection data and the Fourier representation of the object. The Fourier Slice Theorem states that the one-dimensional Fourier transform of a projection acquired at angle θ corresponds to a line through the two-dimensional Fourier domain of the object at the same angle. This relationship is expressed as with the two dimensional Fourier transform $\hat{f}(\omega \cos\theta, \omega \sin\theta)$ of $f(x, y)$ as

$$\mathcal{F}_t\{Rf(t, \theta)\}(\omega) = \hat{f}(\omega \cos\theta, \omega \sin\theta) \tag{37}$$

This theorem results in each measured projection providing one radial slice through the Fourier domain of the object. More projections gradually fill the Fourier space. In theory, once the Fourier domain has been sufficiently sampled, the original object can be reconstructed using the inverse two-dimensional Fourier transform

$$f(x, y) = \mathcal{F}^{-1}\{\hat{f}(\omega_x, \omega_y)\}, \tag{38}$$

where $\omega_x = \omega \cos\theta$ and $\omega_y = \omega \sin\theta$. However, this results in dense sampling of low frequencies and sparse sampling at higher frequencies. Since low frequencies describe smooth image structures while high frequencies contain fine details and edges, this direct Fourier reconstruction only yields blurred objects. Therefore, the frequencies have to be filtered before reconstructions, and the Fourier Slice Theorem forms the theoretical basis for reconstruction methods such as filtered backprojection [KS01].

2.6.1 Filtered Backprojection

Filtered backprojection reconstructs the object from its projection data in two steps: filtering of frequencies and backprojection across the image domain.
The backprojection distributes each detector value back along the corresponding X-ray path through the image domain. For a projection $p(t, \theta)$, the backprojected image is obtained by integrating the detector values over all projection angles [KS01],

$$b(x,y) = \int_0^{\pi} p(x\cos\theta + y\sin\theta, \theta)\, d\theta \tag{39}$$

This process effectively smears each projection across the image domain, so that with many projections the general structure of the object becomes visible. However, this still yields blurred images as low spatial frequencies are overrepresented in the reconstruction. To compensate for this, the projection data is filtered before backprojection. In FBP, the detector function is first transformed into the frequency domain using the Fourier transform. The resulting spectrum is then multiplied by a high-pass filter, commonly the Ram-Lak filter,

$$H(\omega) = |\omega| \tag{40}$$

to amplify high-frequency components responsible for edges and fine details. Other commonly used filters are explained in Chapter 2.6.2. The filtered projection is then given by

$$Q(t,\theta) = \mathcal{F}^{-1}\left\{|\omega|\,\mathcal{F}\{p(t,\theta)\}\right\}. \tag{41}$$

Finally, the filtered projections are backprojected to obtain the reconstructed image,

$$f(x,y) = \int_0^{\pi} Q(x\cos\theta + y\sin\theta, \theta)\, d\theta. \tag{42}$$

With sufficient projections this yields sharp reconstructions with well-defined edges. Reconstructing all acquired detector rows sequentially, generates a complete three-dimensional CT volume.
The CT reconstruction using FBP of the Dark-field signal can be performed analogous as shown in [Bec+10] with a map of the linear diffusion coefficient as

$$\epsilon(x,y) = \int_0^{\pi} Q(x\cos\theta + y\sin\theta, \theta)\, d\theta. \tag{43}$$

2.6.2 Frequency filters

The general frequency response used in the filtered backprojection algorithm can be written as

$$H(\omega) = |\omega| \cdot h(\omega), \tag{44}$$

where $|\omega|$ represents the ramp filter and $h(\omega)$ is a function that modifies the frequency response to control noise and resolution. The factor $h(\omega)$ differs depending on the chosen filter and is defined for a few example filters as:

$$h(\omega) = \begin{cases} 1, & \text{Ram-Lak filter,} \\ \operatorname{sinc}(\omega), & \text{Shepp-Logan filter,} \\ \cos\left(\frac{\pi\omega}{2}\right), & \text{Cosine filter,} \\ \alpha + (1-\alpha)\cos(2\pi\omega), & \text{Hann } (\alpha = 0.5) \text{ and Hamming } (\alpha = 0.54) \text{ filters.} \end{cases} \tag{45}$$

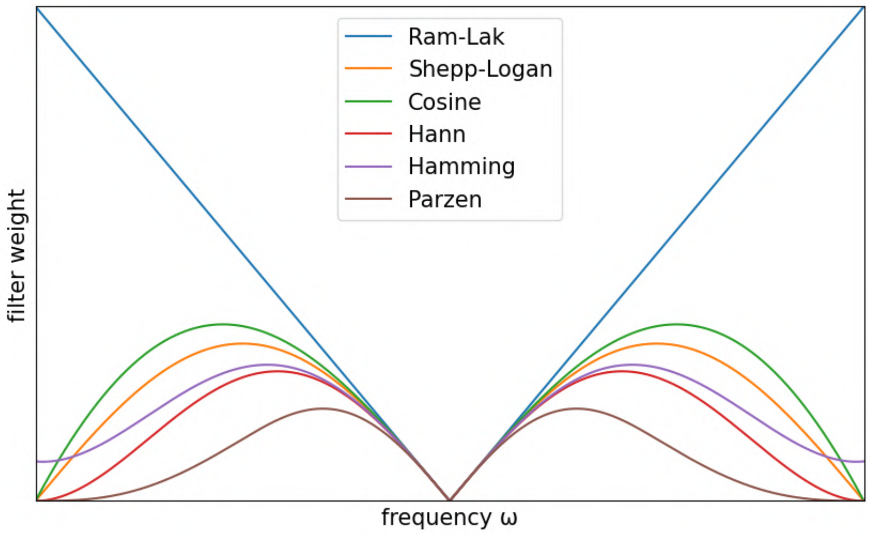

Figure 6: Filter weight of different frequencies for commonly used filters in filtered backprojection. The Ram-Lak filter assigns increasing weight to higher frequencies, whereas other filters suppress very high frequencies, resulting in a maximum weight of a specific frequency.

For the Parzen filter, $h(\omega)$ is defined as

$$h(\omega) = \begin{cases} 1 - 6|\omega|^2 + 6|\omega|^3, & 0 \leq |\omega| < \frac{1}{2}, \\ 2(1 - |\omega|)^3, & \frac{1}{2} \leq |\omega| \leq 1, \\ 0, & |\omega| > 1 \end{cases} \tag{46}$$

[Buz08a]. The overall frequency response of each filter is shown in Figure 6. The Ram-Lak filter is a high-pass filter that reduces blurring caused by low-frequency components. The other filters apply lower weighting to high-frequency components than the Ram-Lak filter, resulting in less suppression of low-frequency data. This causes a general reduction of noise at the cost of spatial resolution [Buz08b; KS88].

2.6.3 Interlaced method

In CT reconstructions, high frequency artifacts are generated away from the center. Those artifacts can be reduced by tangential averaging of the data, blurring the information that is far from the projection center. This can be classically achieved by rotating the sample at constant speed during image acquisition. In X-ray grating interferometry, a similar method can also be applied to the phase-stepping scan by applying a sample rotation simultaneously with the phase stepping scan, as shown in Figure 7.
Hence, in this interlaced approach, the frames of a phase-stepping scan are all recorded at different viewing angles instead of at the same angle as in the standard method.
Using the interlaced approach significantly reduces the high-frequency artifacts without affecting the sharpness of the features. For the same dose deposited in the sample, interlaced CT yields better quality reconstructions than standard phase-stepping CT.

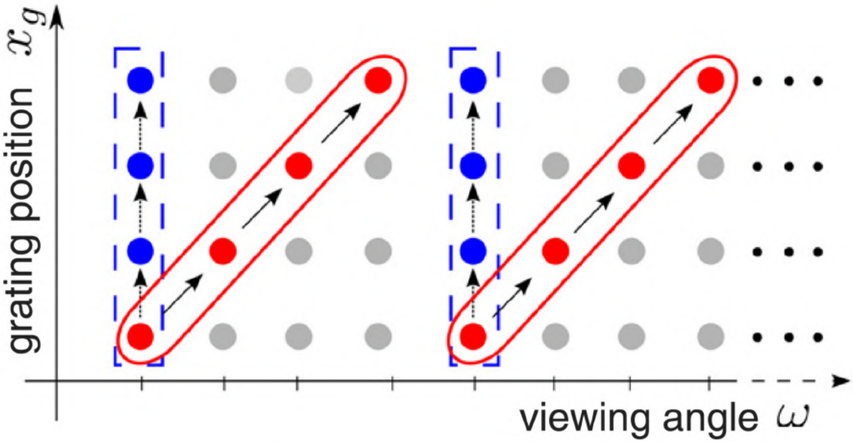

Figure 7: The grating position in dependence of the viewing angle for interlaced phase-stepping (red) and standard phase-stepping (blue) [Zan+11].

Hence, the interlaced method offers a better reconstruction quality per dose, or measurement time [Zan+11]. Therefore, by reducing the reconstruction quality of interlaced phase-stepping CT through the use of a lower dose, the measurement time can be reduced while maintaining a quality similar to that of standard phase-stepping CT.

2.7 Detector properties

Currently, most clinical CT systems use solid state Energy-Integrating Detectors (EIDs) to convert X-rays to electrical signals. Those clinical CT detectors use an indirect conversion, where first a scintillator layer converts X-ray photons to visible light, which is then measured by a photodiode layer [Lel+15; Sar+23]. Hence, it is converted to an electric output signal proportional to the energy deposited in the measurement interval. Since the energy of all photons is integrated over the interval, there is no information about the energy of the individual photons or amount in the output signal. The spatial resolution is also limited, as scintillators and optical coupling produce a lateral light shift. Furthermore, reducing pixel size requires septa to separate them, which leads to a larger fraction of inactive detector area. This leads to more absorbed X-rays, not contributing to the measured signal. Therefore, it produces a reduced dose efficiency, which is particularly a problem in medical applications. Those problems can be improved by using Photon-counting detectors (PCDs). They consist of a single semiconductor layer, commonly CdTe, CdZnTe, or silicon, that converts the X-ray photons into electron-hole pairs. A bias voltage is applied to guide the electrons to the pixelated anode at the bottom of the semiconductor, whereas the cathode is at the top. Therefore, X-rays are directly converted into an electrical pulse, whose amplitude is proportional to the photon energy. Since each photon creates a separate electrical signal, they can be discriminated using pre-set energy thresholds. The spatial resolution can be improved, as there is no scintillator and consequently optical septa, leading to smaller pixel sizes. Furthermore, the detective quantum efficiency (DQE) is roughly constant as a function of X-ray energy and yields photon counts. Hence, low-energy photons are not under-weighted as with EIDs, which can improve the material-contrast [Sar+23]. These advantages can make PCDs especially beneficial for Dark-field imaging.

For CdTe-based PCDs, as in this work, streaks appearing over time due to populating charge traps and activation of charge-sharing mechanisms have to be taken into account. Carge trapping describes when electrons or holes are captured by defects in the crystal, which leads to a loss in the measured charge. Those effects and their time dependence for the detector in this work are extensively covered in [Fri25].

3 CT Setup

In this work a Talbot-Lau interferometer CT setup consisting of a X-ray source (Comet MXR 160/22), a photon-counting detector (Dectris Eiger2 R 1M CdTe), and three gratings (G_0, G_1, G_2) mounted on a rail-based optical table was used. The grating arrangement follows the typical Talbot-Lau setup. G_0, the source grating, is positioned next to the X-ray tube. Downstream of the beam is the sample placed, followed by the phase grating G_1, then analyzer grating G_2 and finally the detector. Two different grating configurations and individual distances were employed in this work. The first configuration, labeled CT setup 1, had gratings with the following specifications:

- G_0: $p_0 = 24.39\,\mu$m, $h_0 = 200\,\mu$m, $dc_0 = 0.5$, Gold
- G_1: $p_1 = 4.37\,\mu$m, $h_1 = 14\,\mu$m, $dc_1 = 0.5$, Nickel
- G_2: $p_2 = 2.4\,\mu$m, $h_2 = 90\,\mu$m, $dc_2 = 0.5$, Gold

Their individual distances are approximately 600 mm between G_0 and G_1, and 59 mm between G_1 and G_2, resulting in a total interferometer length of 659 mm. For the CT the relevant distances are source-detector-distance SDD = 1298 mm and source-origin-distance SOD = 864 mm. The second configuration, labeled CT setup 2, only the G_1 and the grating distances were changed resulting in the following specifications:

- G_0: $p_0 = 24.39\,\mu$m, $h_0 = 200\,\mu$m, $dc_0 = 0.5$, Gold
- G_1: $p_1 = 4.37\,\mu$m, $h_1 = 6.4\,\mu$m, $dc_1 = 0.76$, Gold
- G_2: $p_2 = 2.4\,\mu$m, $h_2 = 90\,\mu$m, $dc_2 = 0.5$, Gold

Their individual distances are approximately 1175 mm between G_0 and G_1, and 115 mm between G_1 and G_2, resulting in a total interferometer length of 1290 mm. For the CT the relevant distances are SDD = 1552 mm and SOD = 1244 mm. The G_1 gratings have a π phase shift. All gratings are mounted on a dedicated holder that allows manual tilting through two adjustment screws.
The currently used CT setup 2 is shown in Figure 8 with the components marked. The X-ray tube is not shown as it is somewhat hidden behind a the filter-wheel at the right edge of the image. The G_1 is held by two separate stages, that were used to increase the stability of the setup and are covered in Chapter 5.3.1.

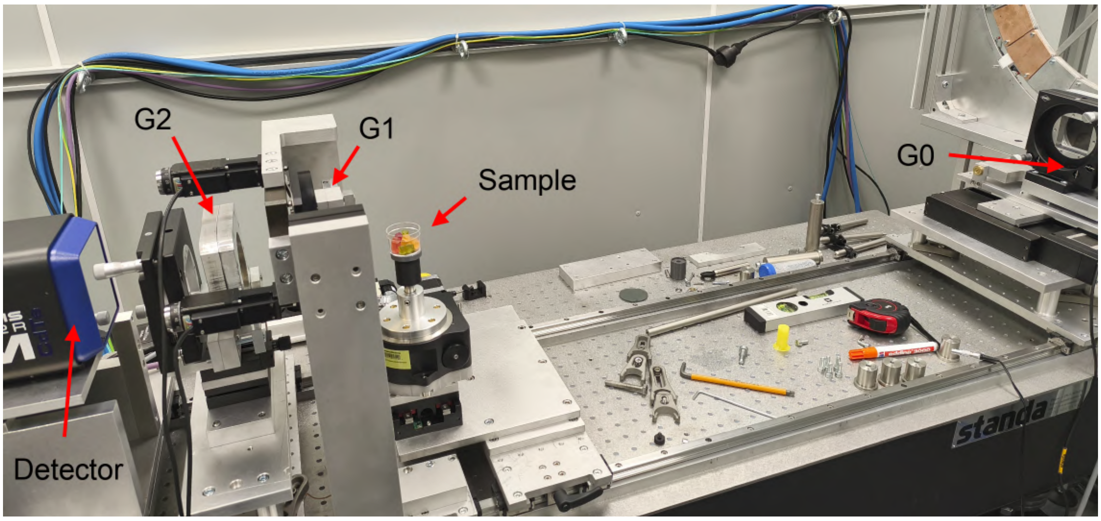

Figure 8: Photograph of the Talbot-Lau interferometer setup including the gratings G_0, G_1, and G_2, the sample with its stage, and the detector. The view of the X-ray tube is blocked by the filter-wheel next to the G_0

4 Workflow of CT acquisition and reconstruction

By using a Talbot-Lau interferometer, the projections have to be performed as phase-stepping scan, with either the standard method or interlaced method. In the standard method, a projection is acquired by laterally shifting the source grating G_0 in discrete steps over at least one full grating period ($p_0 = 24.39\,\mu$m). For a CT, after a phase-stepping scan, the sample is rotated and another phase-stepping scan is performed. In the interlaced method, this object rotation is performed with each phase-step, and the phase-steps used for multiple projections. In this work, mostly the configuration of 7 phase-steps with 5 per period, e.g. the distance of 5 phase-steps correspond to the grating period was used, but others were also compared. The acquisition time for each phase-step was adapted for different samples, while it was in the range of $t = 1\,$s and $t = 60\,$s. The CT measurements were performed over a total angle sector of either $a_{\text{sector}} = 185°$ or $a_{\text{sector}} = 360°$, usually sampled in angle steps of $a_{\text{step}} = 0.5$, but this was also further reduced to $a_{\text{step}} = 0.2°$ to improve reconstruction quality using the interlaced method. The tube voltage was mostly kept $U = 39\,$kVp with a tube current of $I = 16\,$mA. CT measurement using the standard method had flat-field images taken every 60°, which was increased to every 30° for measurements with long acquisition times. In the interlaced method either only at the start or at the start and end a flat-field was performed. This was mainly done, as the interlaced method allows a projection acquisition without resetting the position of the source grating.

Image processing

The flat-fields or reference scans and the object scans use the same stepping protocol as the corresponding object scan. Before signal extraction, the vertical intra-module gap in the detector images was interpolated. Depending on the sample the images were cropped to a 300 px × 650 px, 370 px × 650 px, 200 px × 720 px region covered by the G_1 grating, where a moiré pattern was visible. The image modalities were first determined using a custom algorithm as described in [Kae+17], which was implemented by Constantin Rauch and Markus Schneider, and later through the X-Aid DPC tool [MIT26]. In the custom algorithm for each phase-stepping scan, a pixel-wise sinusoidal fit was performed, whose full period corresponding to the phase-steps range is adjustable. This yields the mean intensity $\bar{I}$ the visibility $V = A/\bar{I}$, and phase-shift Φ for every pixel and every phase-stepping scan for the object and reference images. Using these values, the attenuation, phase-shift and Dark-field signal were computed. The X-Aid DPC yields only the image modalities, which have less moiré artifacts in the final images, as a correction to the phase-step position is applied, but all the phase-steps must be contained within a single period.

CT reconstruction

The sets of projections were subsequently processed first utilizing the ASTRA Toolbox in parallel geometry using the filtered backprojection algorithm and afterwards with a cone-beam vector geometry using the FDK algorithm [AST25]. For each measurement, the attenuation and Dark-field datasets were reconstructed and saved as 3D-numpy arrays. The resulting volumes were visualized and analyzed using Dragonfly [Com26]. Since those reconstruction showed errors, as pointed out in Chapter 5.4, reconstruction with the commercially available software X-Aid were tested [MIT26]. Those reconstructions did not show reconstruction errors. in X-Aid were performed using the FDK algorithm, whereas the FDK algorithm used a 0.5 px Hamming filter. The files used in X-Aid, where all in .tiff, and the reconstruction yielded 2D-slices corresponding the number of height voxels, which can be directly loaded into Dragonfly as 3D-volume.

Figure 9: Gelatin phantom with three regions of different powder particle sizes and a piece of wood. The region in the front has a particle size of $d_p = 24.55\,\mu\text{m}$, the one on the right $d_p = 1.89\,\mu\text{m}$, and on the left $d_p = 5.61\,\mu\text{m}$. A piece of wood is located in the middle.

5 Parameter Determination

Before analyzing cancer tissue samples, the parameters for CT acquisitions are investigated and optimized. In this chapter, the quality of the phase-stepping scans is first evaluated under various parameter settings. Based on these results, the signal and noise characteristics of a CT reconstruction of a phantom are then analyzed for different angle step sizes, angle sectors, and frame times. This was motivated by the expectation that better projections lead to better CT quality.

5.1 Evaluation of projection and reference images

5.2 CT setup 1

5.2.1 Investigation of the influence of focal spot size, tube current and particle size using a Gelatin phantom

To test the influence of various parameters such as, particle size d_p, focal spot size f and tube current I, a gelatin phantom is created. After the gelatin solution is heated in a cooking pot, it is filled in a sample holder and cooled down. When the gelatin is hard enough so that the inserted powder does not diffuse but also becomes enclosed after it is inserted, aluminum-oxide powder of sizes $d_p = 1.89, 5.61, 24.55\,\mu\text{m}$, as well as a piece of wood was inserted. The phantom is shown in Figure 9. It is assumed, that the particle size separation of the aluminum-oxide powder was achieved by sieving, so the exact size distribution is unknown, and the particle size therefore represents a limit rather than a precise value. For this phantom, CT measurements with an step acquisition time $t = 1\,\text{s}$, angle step size of $0.5°$, an angle sector of $185°$, 6 phase-steps with 5 per G_0-period. The combinations of focal spot size and tube current parameters used are $f = 1.0\,\text{mm}$ $I = 10\,\text{mA}$, $f = 5.5\,\text{mm}$ $I = 10\,\text{mA}$, $f = 5.5\,\text{mm}$ $I = 40\,\text{mA}$, and their impacts on visibility and dark-field determination is investigated. Every

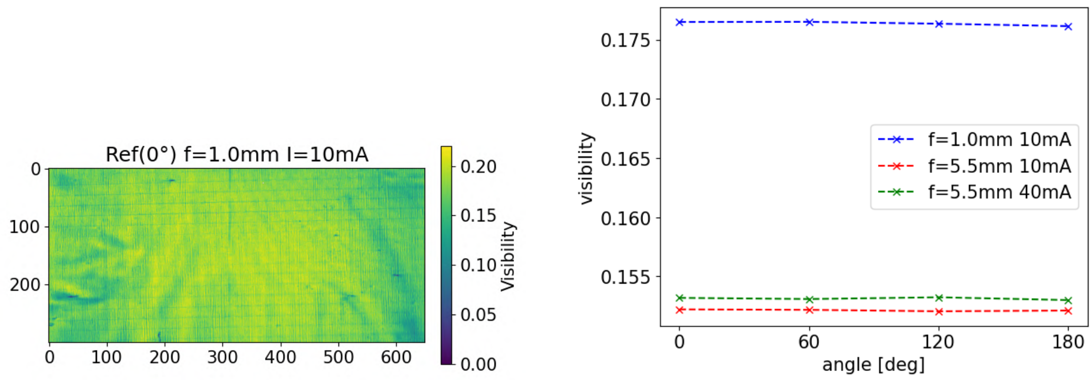

(a). (b).

Figure 10: Shown is the first visibility map of a CT measurement using $U_{\mathrm{B}} = 55\,\mathrm{kVp}$, $I = 10\,\mathrm{mA}$, $\mathrm{Th} = 20\,\mathrm{keV}$, $t = 1\,\mathrm{s}$, 6 phase-steps with 5 per G_0-period, $a_{\mathrm{step}} = 0.5°$ over $a_{\mathrm{sector}} = 185°$. The investigated parameter here is the focal spot size, where in (a) is $f = 1.0\,\mathrm{mm}$ and in (b) is $f = 5.5\,\mathrm{mm}$.

60° a reference image was acquired as shown in Figure 10a, and the corresponding mean visibilities for each measurement are shown in Figure 10b. The results show that a focal spot size of $f = 1.0\,\mathrm{mm}$ provides higher visibility than $f = 5.5\,\mathrm{mm}$, since a smaller focal spot enhances the spatial coherence of the X-ray beam, hence increasing phase contrast and, consequently, the visibility. The measurement with a tube current of 40 mA has a slightly higher visibility than that with 10 mA, which could be due to reduced relative noise in the determination of visibility. The overall visibility remains mostly constant within a CT measurement, but there are small changes and to investigate those differences in more detail the later visibility maps are subtracted from the first one. The difference between the visibility maps at 0° and 60°, which means Vis_Ref(0°) − Vis_Ref(60°), is shown in Figure 11a. The corresponding difference between 0° and 180°, Vis_Ref(0°) − Vis_Ref(180°), is shown in Figure 11b. Both images show moiré artifacts on the left, which have a higher amplitude in Figure 11b, and on the right side more grain like artifacts. Since there are more deviations with a larger value on the right side, it is assumed that something causes a larger change there, which might be explained by tiny tilts of a grating, expansions to due temperature changes, or a drift of the focal spot. Additionally, the change of visibility from the $f = 1\,\mathrm{mm}$ to the $f = 5.5\,\mathrm{mm}$ focal spot size is further investigated by analyzing the results of the mean visibility map of $f = 1.0\,\mathrm{mm}$ and $I = 10\,\mathrm{mA}$ divided by the mean visibility map of $f = 5.5\,\mathrm{mm}$ and $I = 10\,\mathrm{mA}$, as shown in Figure 12. This shows a massive gradient from top to bottom, where at the bottom the values are close to one; hence, no change occurs. However, at the top, the visibility is up to a factor of ≈ 1.5 higher for the $f = 1.0\,\mathrm{mm}$ spot size than for $f = 5.5\,\mathrm{mm}$. Such an effect might be caused by a spatial variation in the coherence properties of the wavefront arriving at the G_1 grating, for example, due to beam divergence and a different effective grating orientation.

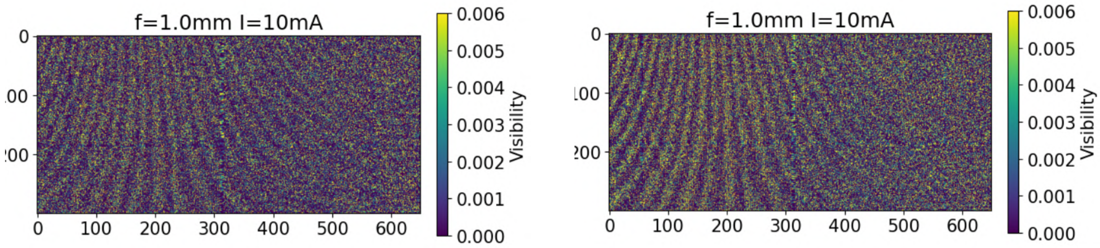

(a). (b).

Figure 11: (a) Visibility difference from the reference image of a CT measurement taken at an angle 0° and 60°, also written as Vis_Ref(0°) − Vis_Ref(60°). The used reference images have a recorded time difference of $t_{diff} \approx 18\,\text{min}$. (b) Difference of Vis_Ref(0°) − Vis_Ref(180°) with a time difference of $t_{diff} \approx 72\,\text{min}$.

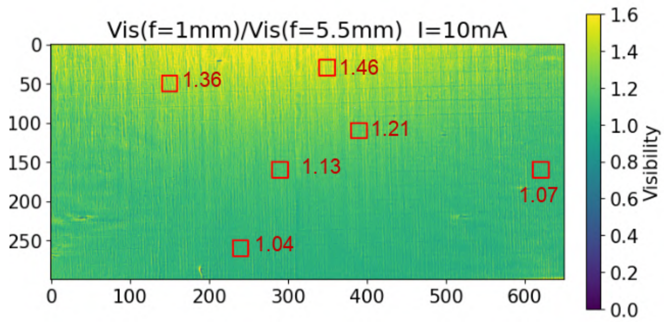

Figure 12: Division of the visibility maps shown in Figure 10. To show the visibility differences red rectangles with the mean values of the pixel within written next to it.

Dark-Field and transmission Imaging of the gelatin phantom

After analyzing the visibilities of the reference images, now from projection resulting dark-field images and transmission images are investigated. In Figure 13a, the dark-field image shows the powder areas as bright yellow areas where the middle has $d_p = 24.55\,\mu\text{m}$, the one on the right $d_p = 1.89\,\mu\text{m}$, and on the left $d_p = 5.61\,\mu\text{m}$. In comparison, the corresponding transmission image in Figure 13b barely shows the powder regions on the left or right, because the gelatin itself through the whole volume also produces a large absorption signal. This highly increased contrast of gelatin and powder already demonstrates the massive advantage of dark-field images to standard transmission imaging.

The dark-field images using $f = 5.5\,\text{mm}$ in Figure 13c show significant smearing of the powder area. Especially at the left powder area, where for $f = 1.0\,\text{mm}$ the edges are much sharper, which is the expected influence of the focal spot size. With $f = 5.5\,\text{mm}$ and $I = 40\,\text{mA}$ in Figure 13d has a more continuous gradient at the edges of the left powder area, because of less noise compared to the measurement with $f = 5.5\,\text{mm}$ and $I = 10$.

To better compare the acquired modalities, Figure 14 shows a line plot of the pixel column $x = 320$, smoothed using a Savitzky-Golay filter. This allows a direct comparison

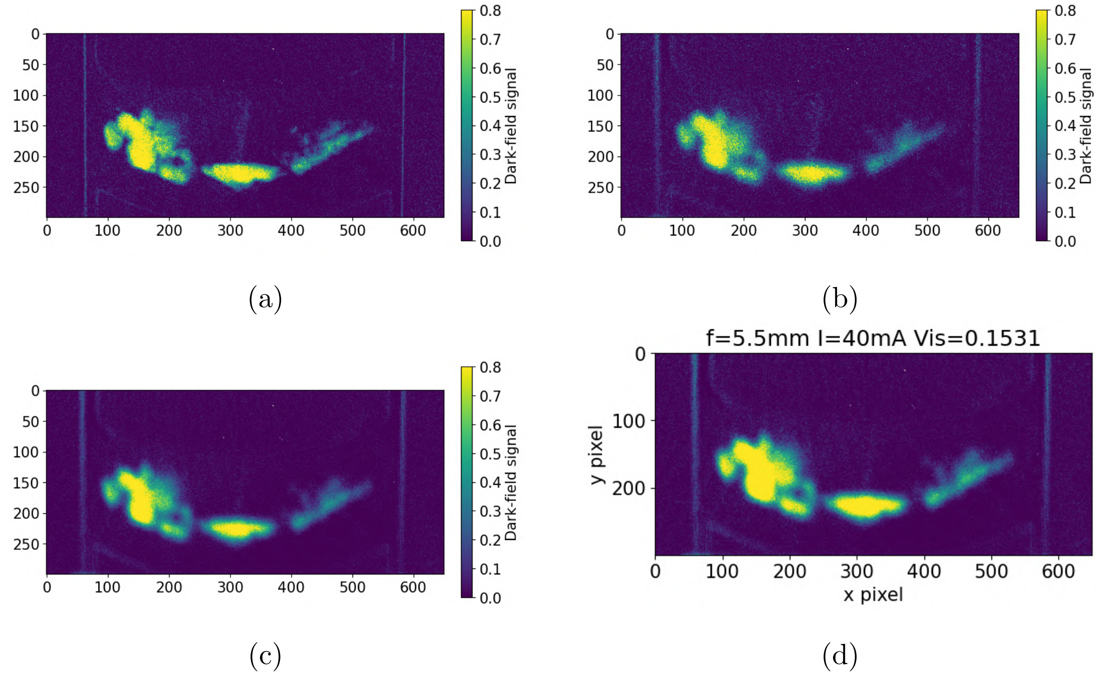

Figure 13: Dark-field (a) and transmission (b) image of a projection from a CT measurement of the gelatin phantom under tube parameter $f = 1.0\,\mathrm{mm}$ $I = 10\,\mathrm{mA}$. (c) Dark-field image with a different focal spot size $f = 5.5\,\mathrm{mm}$ $I = 10\,\mathrm{mA}$. (d) Dark-field image with a different focal spot size and current $f = 5.5\,\mathrm{mm}$ $I = 40\,\mathrm{mA}$.

of signal behavior across the powder region. For this powder region, a signal can be identified in dark-field and transmission, but the gelatin causes a large transmission signal, making the dark-field signal significantly more pronounced. After rotation of the sample by 129° the powder region corresponding to $d_p = 1.89\,\mu\mathrm{m}$ is centered, as shown in Figure 15a. This displays a more diffuse region which is investigated by showing the line plots of pixel column $x = 291$ in Figure 15b. This does not show a significant signal in the transmission, unlike the dark-field, where a clear signal is still visible. Therefore, it has a much larger contrast in the dark-field as in the transmission modality. At y pixel 145 and 190 the line of the dark-field with $f = 1.0\,\mathrm{mm}$ shows peaks, whereas for $f = 5.5\,\mathrm{mm}$ there are no clear peaks. For both those peaks in $f = 1.0\,\mathrm{mm}$, the signal of $f = 5.5\,\mathrm{mm}$ keeps ascending towards higher y pixels. This can be attributed to the smearing caused by the larger focal spot size. Since d_p is assumed to be only a limit, the distribution of the exact powder particle sizes is unknown, and additionally it is also assumed that the signal strength in the projections is solely due to the powder amount, no assertions about the correlation of powder size to signal strength is made with this phantom.

5.2.2 Visibility as a function of tube voltage

The visibility of a Talbot-Lau setup depends on the photon energy primarily due to the energy dependence of the Talbot effect, the resulting change in Talbot distance, the energy-dependent phase shift of the phase grating, and the coherence conditions. Additionally, it is also affected by instrumental effects such as the energy-dependent

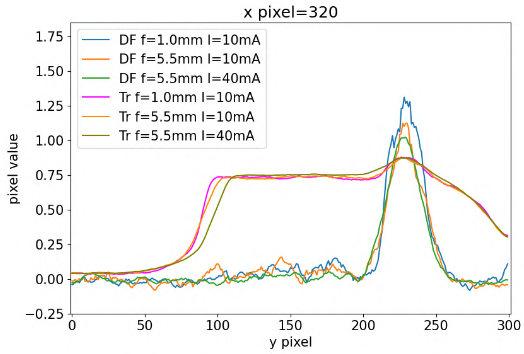

(a).

Figure 14: Line plots through the dark-field and transmission images of a single projection of different focal spot sizes and tube currents of the pixel column $x = 320$ in the images of Figure 13, resulting in a line through the powder region with $d_p = 24.55\,\mu\text{m}$.

absorption of the gratings, the spectrum of the source, and the detector quantum efficiency. Here, multiple reference images, as shown in Figure 16, were taken with tube voltages from 38 kVp to 55 kVp using an acquisition time of $t = 1\,\text{s}$, focal spot size $f = 1\,\text{mm}$, and 6 phase-steps with 5 steps per G_0-period. To compare the visibility at different tube voltages, the mean visibility is determined and plotted as shown in Figure 17. This unexpectedly yields a behavior similar to a landau distribution as such a moyal function of the form

$$\xi = \frac{x - \mu}{\eta}, \tag{47}$$

$$f(x) = \frac{A}{\exp(-0.5)} \cdot \exp\left(-\frac{1}{2}(\xi + \exp(-\xi))\right), \tag{48}$$

was fitted to the data, where μ denotes the peak position, A the amplitude, and η describes the shape of the tail. The fit yields $\mu = 47\,\text{kVp}$ corresponding to the highest visibility, which is attributed to the combined influence of the effects described above. Generally, such a behavior is not expected and does not hold and the fit matching is just coincidence.

5.2.3 Influence of frame time on the free field of dark-field images

The photon counts arriving at the detector should increase linearly with the frame time. The counts are affected by Poisson statistics, so their relative error decreases for more counts. From the measured counts at different phase-steps, the visibility is determined by a sinusoidal-fit, which improves with less relative error of the intensities. To be able to create meaningful CT data, those visibility determinations of the reference and object scans have to be sufficiently accurate also for following scans. Additionally, an increased frame time can also average out short variations or vibrations from the setup. The influence of frame time on the free field of dark-field images of a gummy-bear phantom is analyzed and shown in Figure 18. In Figure 18a are the mean values of the free field, which are expecetly close to zero and much smaller than the corresponding standard deviation shown in Figure 18b. The standard deviation decreases with longer frame

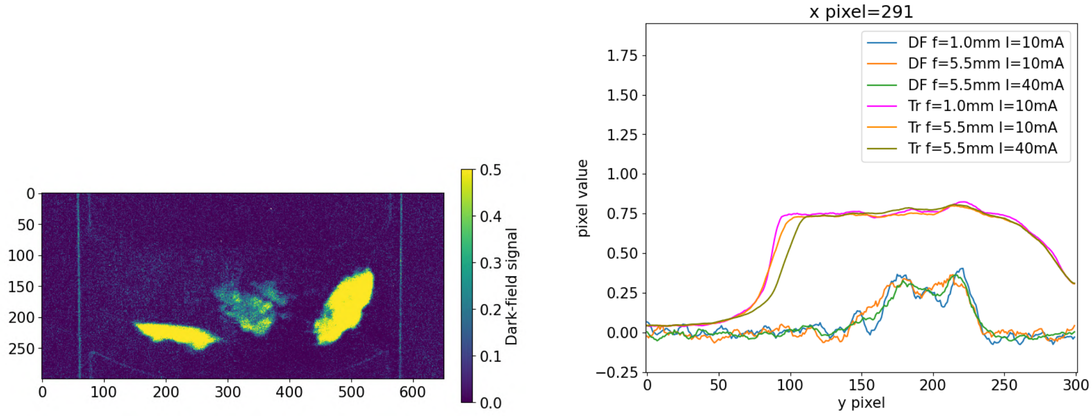

(a). (b).

Figure 15: (a) Projection of the gelatin sample after a rotation of 129°, compared to Figure 13. The rotation causes the $d_p = 1.89\,\mu\text{m}$ aluminum-oxide powder region to be centered in the image. Due to a different powder amount and placement, the powder region appears more diffuse. (b) Corresponding line plot of the pixel column $x = 291$, resulting in a line through the powder region with $d_p = 1.89\,\mu\text{m}$ for the dark-field and transmission.

acquisition times, where a square-root dependence of the noise on the acquisition time is expected due to Poisson statistics. As such, for $t = 4\,\text{s}$ half the standard deviation of $t = 1\,\text{s}$ is expected, but a measured standard deviation is at ≈ 0.59 of the value. This could indicate that either the Poisson statistics does not directly translate into the visibility determination or that there is another noise factor next to the Poisson statistics. Those noise sources could be a non constant G_0 phase-step distance, or vibrations leading to uncertainties in the measured intensity.

5.2.4 Comparison of CT-filter

To investigate the influence of different reconstruction filters on the CT volume, the dataset of a gummy-bear phantom with embedded aluminum-oxide powder is recon-

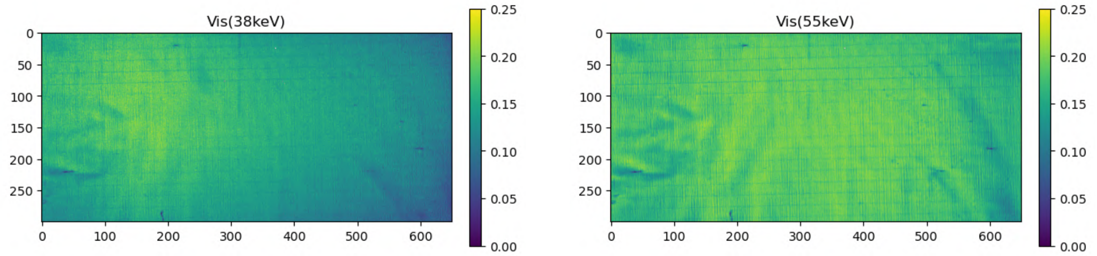

(a). (b).

Figure 16: Different visibility maps of a reference image using $f = 1.0\,\text{mm}$, Th $= 20\,\text{keV}$, $t = 1\,\text{s}$ and 6 phase-steps with 5 per G_0-period. In (a) for a tube voltage of $U_\text{B} = 38\,\text{kVp}$ and in (b) for $U_\text{B} = 55\,\text{kVp}$.

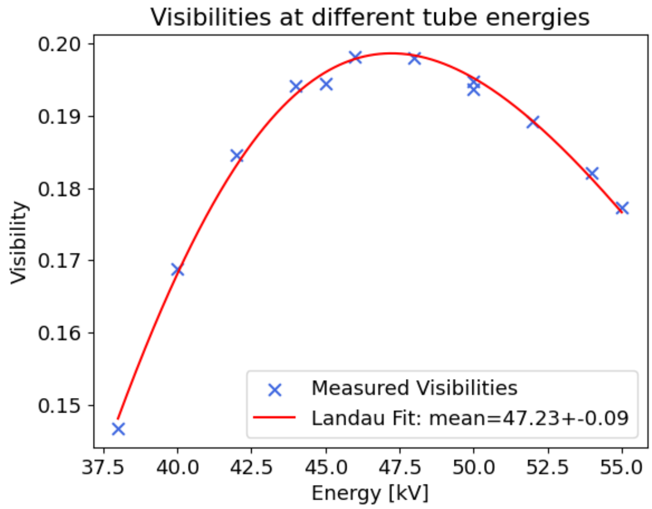

Figure 17: Different measured mean visibilities cquired with $f = 1.0\,\mathrm{mm}$, $\mathrm{Th} = 20\,\mathrm{keV}$, $t = 1\,\mathrm{s}$ and 6 phase-steps with 5 per G_0-period under different tube voltages. Due to the curve of the measured values a Landau (Moyal) fit is applied to determine the peak position.

structed using a set of commonly used filters in filtered back-projection algorithms available in the ASTRA Toolbox, such as the Ram-Lak, Shepp-Logan, Hann, Hamming, and additionally a Parzen filter. These filters differ in their frequency suppression as explained in Chapter 2.6.2, hence they have different spatial resolutions and noise in the reconstructed volume.

Figure 19 shows a 2D slice of the reconstructed 3D volume for the applied filters Ram-Lak in Figure 19a and Parzen in 19b, which is then used for a quantitative evaluation. The gummy-bear lies in the middle of the image, where on the right side the air-transitions of its feet are visible, and in the middle its arms with a region of aluminum-oxide powder inserted.

All reconstructions show a consistent overall structure of the phantom, but clear

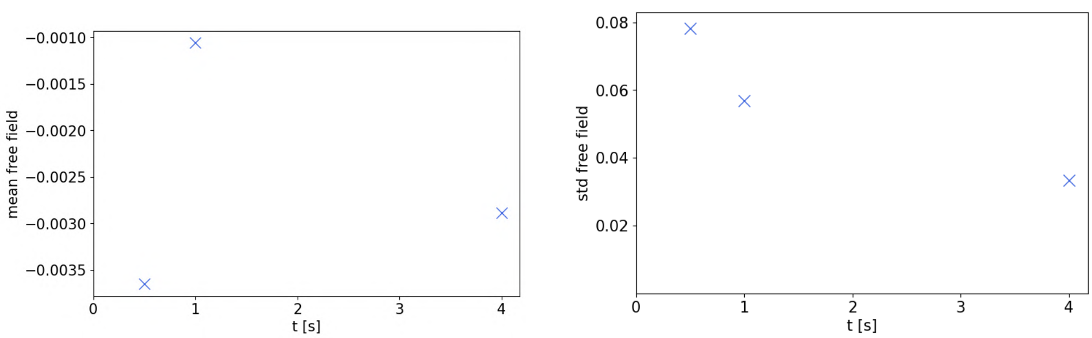

(a). (b).

Figure 18: Mean (a) and standard deviation (b) of the free field for different frame acquisition times.

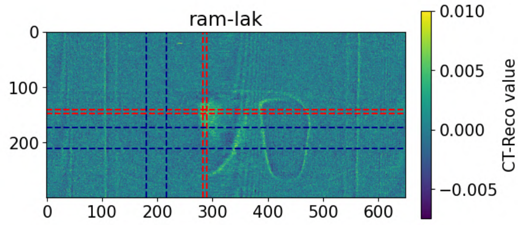

(a).

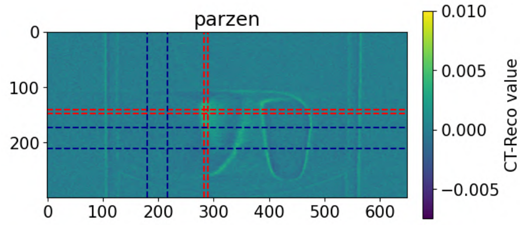

(b).

Figure 19: Slices of a CT reconstruction using the ASTRA toolbox of a measurement with $f = 1.0\,\mathrm{mm}$, $\mathrm{Th} = 20\,\mathrm{keV}$, $t = 1\,\mathrm{s}$, 6 phase-steps with 5 per G_0-period, $a_{\mathrm{step}} = 0.5°$ over $a_{\mathrm{sector}} = 185°$. In (a), the Ram-Lak filter has been applied, while in (b) the Parzen filter is used. Additionally, the areas used for SNR determination is marked with the aluminum-oxide signal in red and gummy bear noise/background in blue.

differences in edge sharpness and noise are visible. In particular, the Ram-Lak filter preserves the most high-frequency details, leading to sharper edges, but also to increased noise, whereas smoother filters such as the Parzen filter introduce strong smoothing, which significantly reduces noise at the cost of spatial resolution.
For a quantitative evaluation, an aluminum-oxide powder area is defined in the 2D slices, as the rectangle resulting of the red lines in Figure 19. This is used to determine the SNR of the aluminum-oxide powder region and the background signal in the surrounding gummy bear material marked by the blue lines. The SNR is computed from the mean powder signal p and its standard deviation Δp, and the mean bear signal b in the marked area, and its standard deviation Δb as

$$\mathrm{SNR} = \frac{p - b}{\sqrt{\Delta p^2 + \Delta b^2}}; \quad \Delta\mathrm{SNR} = \sqrt{\left(\frac{\Delta b}{\sqrt{\Delta p^2 + \Delta b^2}}\right)^2 + \left(\frac{\Delta p}{\sqrt{\Delta p^2 + \Delta b^2}}\right)^2}. \tag{49}$$

The results for each reconstruction are shown in Figure 20.
This shows that the Parzen filter achieves higher SNRs by strongly smoothing the data, resulting in a worse spatial resolution, which could lead to blurring of very small objects making them invisible. Hence, when very small objects are of interest, sufficient details must be preserved to detect them. Consequently, the optimal filter choice depends on the expected size and desired contrast of the structures of interest.

5.2.5 Comparison of CT reconstruction of a gummy bear phantom using different angle step sizes

Reducing the angle step size increases the number of projections acquired over a full rotation, which can lead to a more accurate reconstruction, especially when using methods such as Filtered Back Projection. However, this also results in increased CT measurement time, as well as higher computational cost. To compare the impact on the reconstructed CT volume of using different angle step sizes, a measurement of a gummy-bear with aluminum-oxide powder inserted is performed using an angle step size of $a_{\mathrm{step}} = 0.25°$ and an angle sector of 185°. Based on this measurement, projections were selectively removed to create CT reconstructions corresponding to those with angle

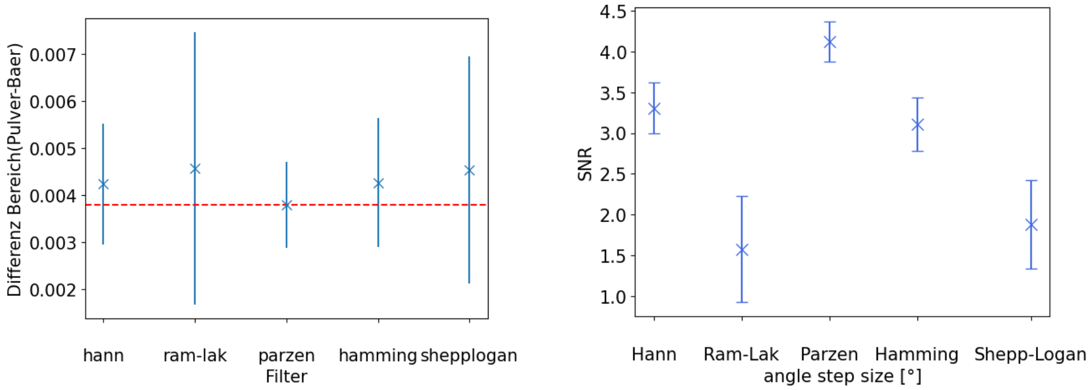

(a). (b).

Figure 20: Quantitative evaluation of different filters, where the values have been determined as marked in 19. (a) Signal difference between aluminum-oxide and background, and in (b) the corresponding SNR.

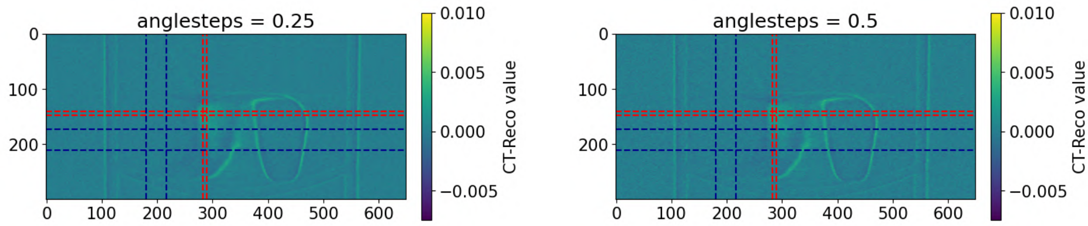

(a). (b).

Figure 21: Slices of a CT volume that has been reconstructed with angle step sizes (a) $a_{\text{step}} = 0.25°$ and (b) $a_{\text{step}} = 0.5°$. The reconstructions were performed using the same dataset, where for the reconstruction corresponding to (b) projection are excluded. The base dataset had parameters $U_{\text{B}} = 55\,\text{kVp}$, $I = 10\,\text{mA}$, $\text{Th} = 10\,\text{keV}$, $a_{\text{sector}} = 185°$, $a_{\text{step}} = 0.25°$ and 6 step with 5 per G_0-period, and a Parzen filter applied on the CT reconstruction.

step sizes $a_{\text{step}} = 0.25°, 0.5°, 1.0°, 1.5°, 2.0°, 2.5°, 3.0°, 3.5°, 4.0°$. The influence of the angle step size is illustrated in Figure 21, where Figure 21a shows the reconstruction using $a_{\text{step}} = 0.25°$ and the Parzen filter. This illustrates that especially the free field has less noise than in Figure 21b, where $a_{\text{step}} = 0.5°$ was used.

Using the SNR, as shown in Figure 22, the quantitative impact of the angle step size on reconstruction quality can be evaluated. An overall increase in SNR for smaller angle step sizes is observed, as expected, only the cases $a_{\text{step}} = 1.5°, 2.5°$ deviate from this and appear as outliers. It is unclear if those outliers are due to an uneven behavior of the reconstruction algorithm, or an effect due to the phantom structure, or just a statistical effect due to the small signal area. A more detailed analysis, particularly considering the reduction in measurement time by maximizing the SNR for a given measurement time through optimization of the angle range, angle step size, and frame acquisition time, is presented in Chapter 5.4.

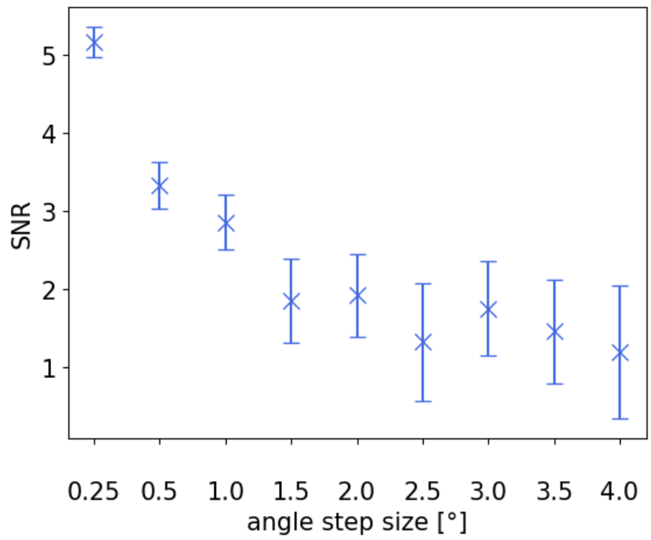

Figure 22: SNR in dependence of the angle step size used for reconstruction of the CT volume. All reconstructions were performed using the same dataset, where for larger angle step sizes projection are excluded. The base dataset had parameters $U_{\mathrm{B}} = 55\,\mathrm{kVp}$, $I = 10\,\mathrm{mA}$, $\mathrm{Th} = 10\,\mathrm{keV}$, $a_{\mathrm{sector}} = 185°$, $a_{\mathrm{step}} = 0.25°$ and 6 step with 5 per G_0-period, and a Parzen filter applied on the CT reconstruction.

5.3 CT setup 2

In this part, measurements using the CT setup 2 are discussed. This setup had various problems with stability of the obtained phase-stepping that were improved. Further, with the measurements using this setup, the influence of different phase-steps amounts in a scan, the visibility in dependence of the tube voltage and set detector threshold, were investigated. Then CT reconstructions are compared using Mitos X-Aid and the ASTRA-Toolbox. Additionally, the interlaced method as a way to decrease measurement time is introduced and finally the parameters affecting measurement time in the interlaced method are evaluated.

5.3.1 Investigation of the stability of the CT setup

The stability of the setup is affected by the changes of the measured intensity over time. This is particularly important as in interferometric X-ray imaging slight shifts of the moiré-pattern over time already degrade the quality of measurements. The moiré-pattern can be shifted by any vibration in the setup, for example the water cooling of the detector, the motorized stage holding the sample or drifts of the focal spot. Additionally, when a phase-stepping scan is performed also inaccuracies of the positions of the stage moving the G_0 could lead to an inaccurate visibility determinations. After the CT setup 2 was assembled, stronger moiré-artifacts were found in the dark-field images. Hence, to quantify the changes, a measurement of 900 frames without object of each $t = 1\,\mathrm{s}$ at $35\,\mathrm{kVp}$, $\mathrm{Th} = 15\,\mathrm{keV}$, $I = 10\,\mathrm{mA}$ was performed, while not moving any stages. The measured counts of a single pixel over all frames with their mean and standard deviation marked is shown in Figure 23a. The relative noise of this distribution is further analyzed in Figure 23b. There the x-axis depicts the number of frames used to

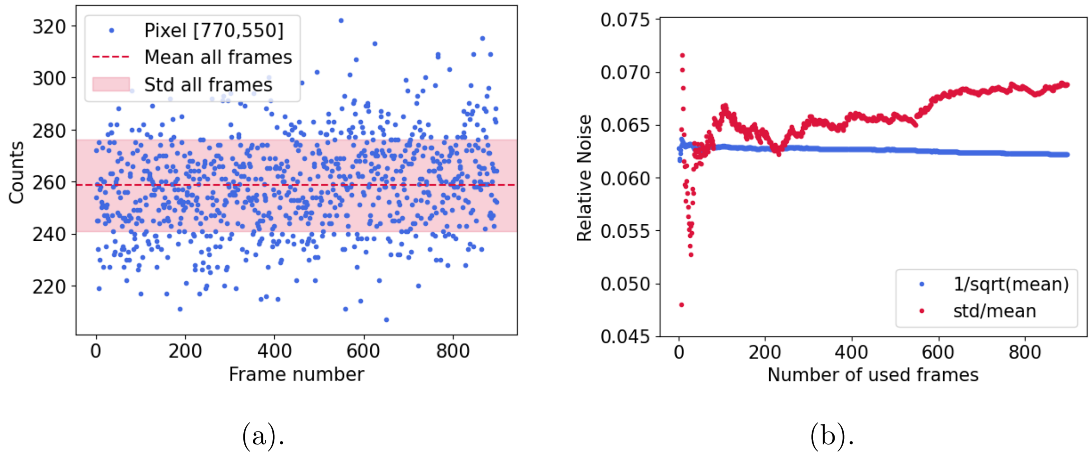

Figure 23: (a) Measured counts of single pixel over 900 frames each. (b) Relative noise of the counts of the same pixel over the amount of frames used to calculate their mean and standard deviation.

calculate its mean and standard deviation. From those is then the relative Poisson-error marked in blue calculated and compared with the relative standard deviation in red. For few values the behavior of the standard deviation is expectantly without a clear trend, but overall is the standard deviation larger than one expected from a Poisson-statistics. This indicated that there are other error sources besides Poisson-statistics. Also the relative Poisson-error decreases slightly over time, coming from a slight increase in counts over the measured time. Deviations of two frames can be evaluated by dividing one through the other. In Figure 24a is the zeroth frame divided through the third frame, which shows a moiré-pattern with an intensity of up to 10%, but such a large moiré-pattern intensity only appears for a few frames.

To detect changes over all frames the pixel row $x = 400$ is plotted for all frames in Figure 24b. Since for the stability the time window is essential, the frame number is converted to their acquisition time. Overall this shows no significant changes in the moiré-pattern within 15 min. Hence, dividing both images leads to a more sensitive evaluation of the changes, and no larger shifts occur without moving a stage within 15 min. The variations during phase-stepping are investigated by recording several reference scans in succession and determining their visibility over a certain pixel area (150x200 pixels). Since a change even on short scales is expected, only 13 reference in succession using parameter $U_B = 35\,\text{keV}$, Th $= 15\,\text{keV}$, $I = 16\,\text{mA}$, $t = 1\,\text{s}$, and 6 steps with 5 per G_0-period. The mean visibilities of this measurements over the measurement time is shown in Figure 25a, which shows large changes of visibilities. Afterwards, a foam was placed to reduce the vibrations caused by the water cooling and the thin cylinder mount holding the G_1 grating replaced by an aluminum L-mount. This L-mount is located in front of the G_1 in Figure 8. The results of the repeated measurement after the modifications as shown in Figure 25b. This lead to a decrease in standard deviation of the mean visibilities, but there are still problematic fluctuations remaining.

To further decrease any vibrations affecting the grating, a similar measurement was performed using 50 reference in succession using parameter $U_B = 39\,\text{keV}$, Th $= 20\,\text{keV}$, $I = 16\,\text{mA}$, $t = 1\,\text{s}$, and 6 steps with 5 per G_0-period. The results only with the

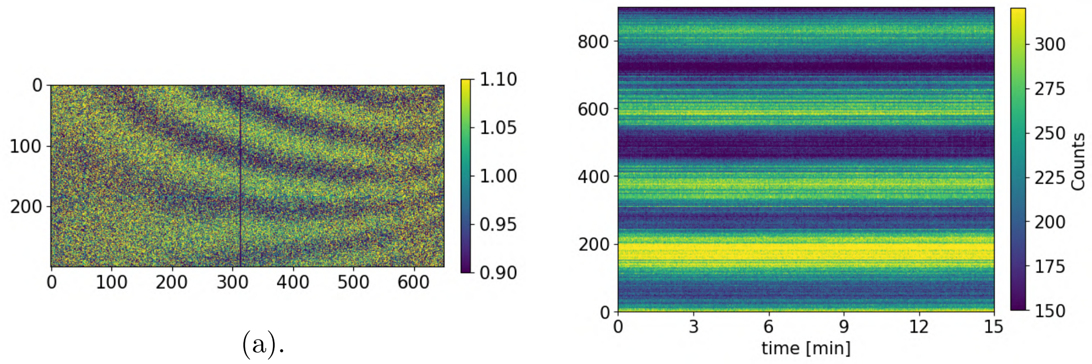

(a).

(b).

Figure 24: (a) Counts of the zeroth frame divided by the third frame, where a frame corresponds to $t = 1\,\mathrm{s}$ and the setup is not moved. (b) Counts of the pixel row $x = 400$ of each frame. The frame number is converted to time to showcase the time difference.

aluminum L-mount are shown in Figure 26a and after adding a second mount for the G_1 in Figure 26b. This further decreased the standard deviation of the mean visibilities by a factor of 2.38. Also, before the second mount there appear two large jumps in visibility, where afterwards a more gradual change is measured.

5.3.2 Investigation of different phase-step configuration

The dark-field is obtained from the parameters of a fitted sinusoidal function applied to the measured intensities of a pixel during the reference and object phase-stepping scan. Hence, to get meaningful dark-field images, sufficiently stable or accurate phase-stepping scans have to be produced. In principle, the accuracy of such fits can be improved either by using more data points equivalent to the number of phase steps or by measuring the sinus period with more steps per period. In a similar way, such a fit can also be improved by having less relative error or noise on the data points, which can be achieved through improving the detector statistics by increasing the frame acquisition time or count rate. To investigate the improvement in the stability of visibility determination in different phase-step combinations, reference images were acquired for various phase-step configurations. Only the visibilities of reference images were compared here, since it is expected that consecutive reference images are very similarly affected as a following object image. For each configuration, four reference images were taken, resulting in four visibility maps with slightly different mean visibilities as shown in Figure 27a. Such a shift in mean visibility of a pixel area directly corresponds to instabilities in the setup that were too large to "average" them out in the fit or affect the whole phase-stepping scan. To enable clearer identification of phase-step combinations, they are labeled in this section as phase-steps/phase-steps per G_0-period. For example, 6 phase-steps with 5 steps per G_0-period are denoted as 6/5. Here, the graphs of 6/5 and 10/10 have the highest fluctuations, while some configurations with less than 10 phase-steps have smaller fluctuations in their mean visibility. This could indicate that only 4 reference images each is too low for an accurate determination of the mean visibility fluctuation and only serves as a lower limit. Interestingly, phase-stepping scan combinations with

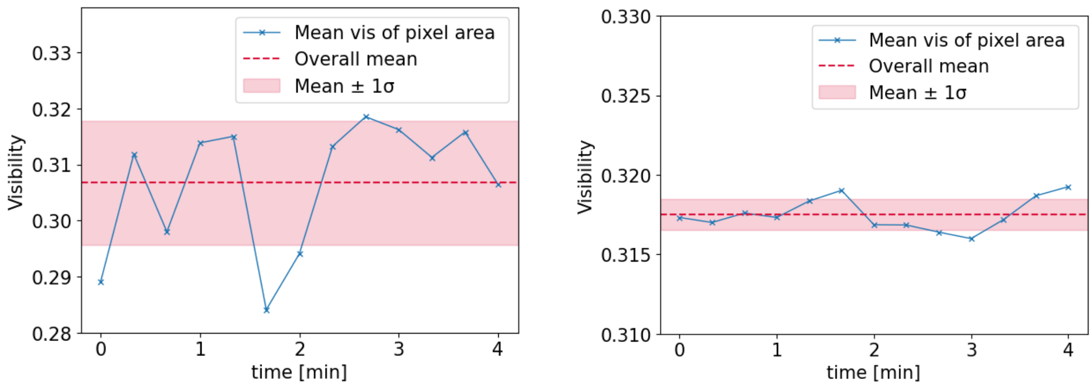

(a). (b).

Figure 25: Mean visibilities of reference images taken in succession over their measurement times for (a) before and (b) after adding a aluminum L-mount for the G_1 and foam at the water cooling.

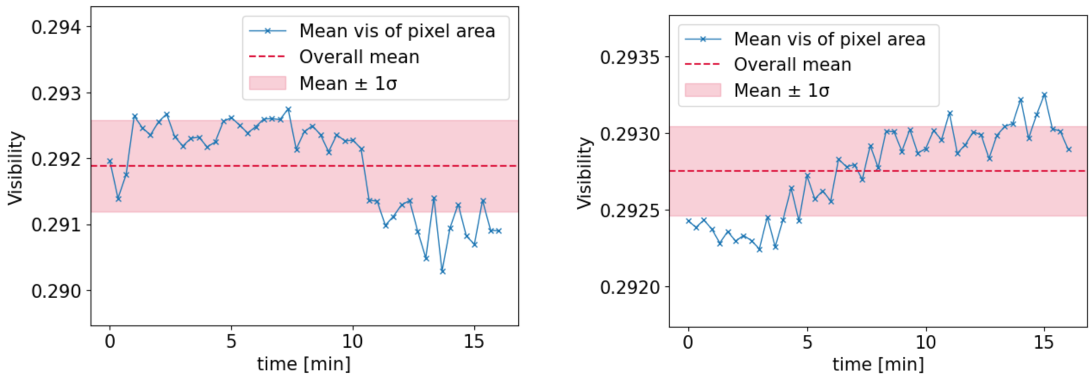

(a). (b).

Figure 26: Mean visibilities of reference images taken in succession over their measurement times for (a) before and (b) after adding a second mount for the G_1.

periods from 5 to 7 have greater visibility when the same visibility of all measurements would be expected. To determine the spread of the measured visibilities, the standard deviation of the same pixel area is calculated as shown in Figure 27b. This yields the highest standard deviations for 6/5, 20/5 the lowest, and 10/10 between them. Both 7/6 and 7/7 have very close standard deviations, where 7/6 is overall slightly lower. Also, the standard deviation of 20/5 is slightly lower as the one of 20/20, which shows a trend that more phase-steps than more phase-steps per period have a slightly less fluctuating visibility determination.
To further evaluate the influence of adding phase-steps while keeping the phase-steps per period at 5, the measurement with 20/5 is taken. From this measurement, the last phase-step was repeatedly removed and the visibility calculated. The same was also done by repeatedly removing the first phase-step. The mean visibility and standard deviation of the visibility for a pixel area (30x30 pixels) is shown in Figure 28a.

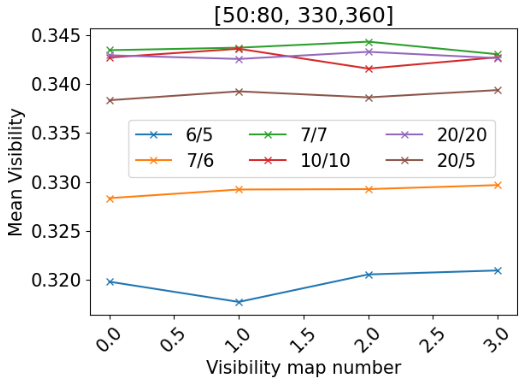

(a).

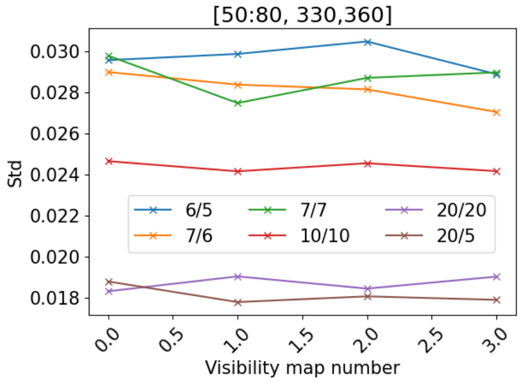

(b).

Figure 27: (a) Mean visibility of a pixel area for four reference images that were acquired for different phase-step combinations. (b) Standard deviation of a pixel area for four reference images that were acquired for different phase-step combinations. All measurements were taken with $t = 1\,\mathrm{s}$, $\mathrm{Th} = 20\,\mathrm{keV}$, $U_\mathrm{B} = 39\,\mathrm{kVp}$ and $I = 16\,\mathrm{mA}$.

This shows a mostly constant behavior for the mean visibilities where the end phase-step is kept. The behavior of the plot where the first phase-step is kept is different as starting with the second removed phase-step the visibility rises, and is higher till the 17 removed phase-step. Such differences could be due to G_0 phase-stepping distances not being exactly constant or the tilt of any grating during the measurement. The standard deviation increases gradually, but to better compare their increase, they are plotted separately in Figure 28b. The behavior of both plots appears to be an exponential function. Generally, phase-steps covering at least one period should be used to determine the visibility and dark-field images, so they are only presented in the plot for completeness and are generally not considered. The decreases with more phase-steps used becomes smaller for each additional phase-step. Hence, no direct optimum in phase-steps for a specific period can be found, and at a certain point increased acquisition time is more costly as the resulting improved imaging quality. Therefore, the combination of 7/5 was chosen for future measurements, as it still offers a larger decrease in standard deviation compared to 6/5. Relative to the 5/5 configuration, 6/5 reduces the standard deviation by approximately 2.26%. This is further reduced for 7/5 by approximately 2.47% relative to 6/5, whereas 8/5 yields a slightly smaller additional reduction of approximately 2.37% relative to 7/5. A comparison of phase-steps with an adapted frame time to acquire phase-stepping scans with the same overall scan time might yield a more significant result.

5.3.3 Visibility as a function of tube voltage and photon energy threshold

Also, for the CT setup 2, the visibility function over energy is investigated using reference images with $f = 1.0\,\mathrm{mm}$ $t = 1\,\mathrm{s}$ and 6 steps with 5 steps per G_0-period, as in this setup a different G_1 is employed. However, this has been extended to also include detector energy thresholds, as shown in Figure 29a. This generally shows an increase with smaller tube voltages, but in the selected range no clear visibility peak as function of energy was observed. For tube voltages 35-37 kVp the visibility also increases with

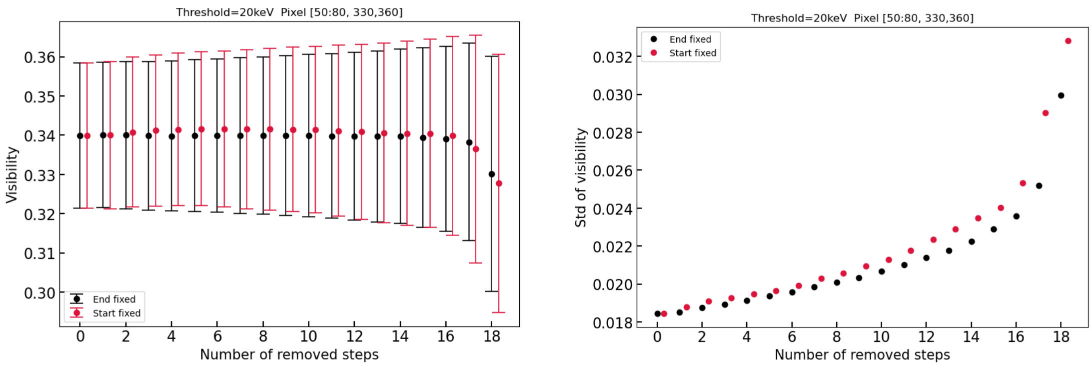

(a). (b).

Figure 28: (a) Mean and standard deviation of visibility of a pixel area. For this a dataset using 20 phase-steps with 5 per G_0-period was acquired. From this dataset once the last phase-step and once the first phase-step was repeatedly removed and the visibility map determined for every removal. The dataset with that keeps the same first phase-step has been moved slightly on the x-axis for better comparison. (b) Standard deviation of the visibility in a pixel area as determined in (a).

larger thresholds, but for 39 kVp and 40 kVp the visibility only increases to a threshold of 22.0 keV and decreases for higher ones. Such an effect could be caused by the grating setup being optimal for a specific spectra, which can not be perfectly matched by a X-ray tube. Hence, there exists an optimal spectra and the visibility increases as this spectra is approached closer.

To better compare similar visibility values, and since decent statistics are needed for proper imaging, as demonstrated in Chapter 5.3.3, the counts from the frames of a reference image have also been determined, as shown in Figure 29b. By neglecting the standard deviation of the visibility as well as Poisson noise of the counts, visibilities corresponding to similar counts can be directly compared in order to optimize the image quality.
Similar counts can be found for $U_\mathrm{B} = 37\,\mathrm{kVp}$, $\mathrm{Th} = 22.0\,\mathrm{keV}$ and $U_\mathrm{B} = 36\,\mathrm{kVp}$, $\mathrm{Th} = 21.0\,\mathrm{keV}$. Interestingly, similar counts can also be found at the same thresholds and increased tube voltage, which is the case for the full threshold row. For those, always the lower energy and lower threshold entry have a better visibility, suggesting a better signal quality at the same statistics. Additional pairs like $U_\mathrm{B} = 39\,\mathrm{kVp}$, $\mathrm{Th} = 22.5\,\mathrm{keV}$ and $U_\mathrm{B} = 37\,\mathrm{kVp}$, $\mathrm{Th} = 20.5\,\mathrm{keV}$ can be found, where the lower energy and lower threshold entry also has a higher visibility. This is also the case for the pair $U_\mathrm{B} = 39\,\mathrm{kVp}$, $\mathrm{Th} = 23.0\,\mathrm{keV}$ and $U_\mathrm{B} = 36\,\mathrm{kVp}$, $\mathrm{Th} = 20.0\,\mathrm{keV}$. Exceptions to this only appear in the recorded data points for 35 kVp and 36 kVp., where from the pair $U_\mathrm{B} = 36\,\mathrm{kVp}$, $\mathrm{Th} = 21.5\,\mathrm{keV}$ and $U_\mathrm{B} = 35\,\mathrm{kVp}$, $\mathrm{Th} = 20.5\,\mathrm{keV}$, the higher tube voltage and threshold has a better visibility. It is expected that this trend changes for lower thresholds as the mean intensity wavelength of the tube gets shifted away from the optimal wavelength of the setup, but for confirmation more data are needed.

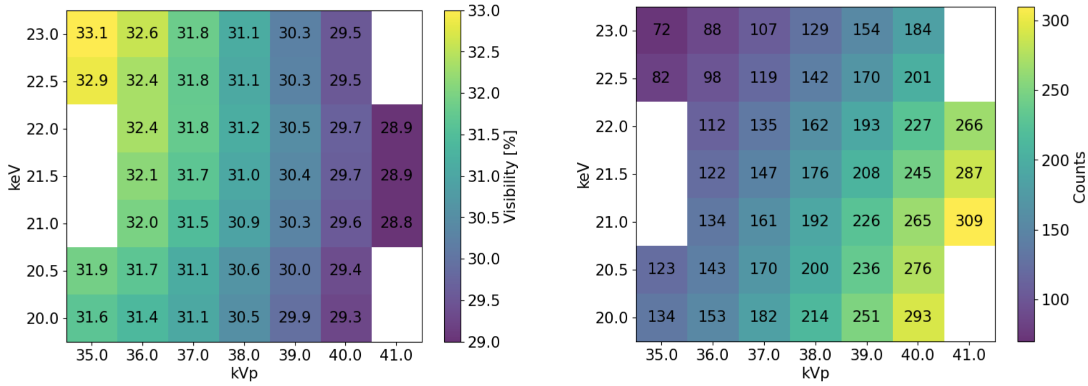

(a). (b).

Figure 29: Results of reference images using $I = 10\,\text{mA}$, $t = 1\,\text{s}$, 6 phase steps with 5 per G_0-period and a various set of tube voltages and detector thresholds. In (a) are the resulting mean visibilities displayed, while in (b) are the mean counts of a pixel of a single frame shown. Only the pixel in upper center area (336×380 pixel) are used for this evaluation.

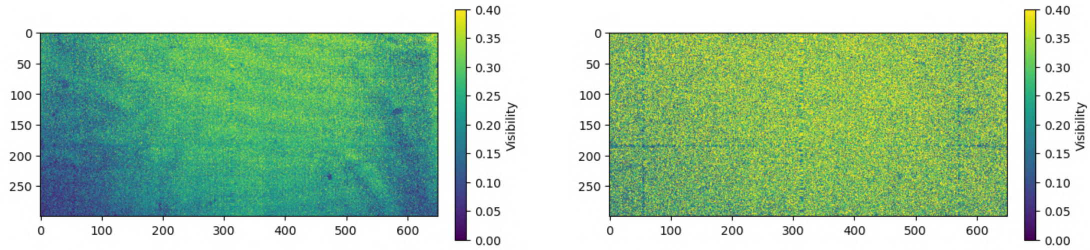

(a). (b).

Figure 30: Visibility maps obtained using $U_\text{B} = 35\,\text{kVp}$, $I = 10\,\text{mA}$, $t = 1\,\text{s}$, 6 phase steps with 5 per G_0-period. (a) Was taken with a threshold of $\text{Th} = 20\,\text{keV}$ and (b) with threshold $\text{Th} = 28\,\text{keV}$

Visibilities of lower energies

While investigating the highest visibility for the new setup, higher visibilities were found at lower energies. The visibility maps of reference images using $f = 1\,\text{mm}$, $U_\text{B} = 35\,\text{kVp}$, $t = 1\,\text{s}$, 6 phase-steps with 5 per G_0-period are shown in Figure 30a for a threshold $\text{Th} = 20\,\text{keV}$ and in Figure 30a for a $\text{Th} = 28\,\text{keV}$. Figure 30a in principle has a very good mean visibility, but while even some moiré artifacts and lower intensity regions due to the grating can still be seen the visibility map already exhibits heavy grain noise. Figure 30b in principle has an even better mean visibility, but no features of the gratings can be identified and the visibility map is dominated by its standard deviation. To further analyze the statistics leading to grain noise dominated visibility maps that have higher mean visibilities, the pixel count values for detector thresholds $\text{Th}{=}20, 23, 24, 25, 26, 27, 28\,\text{keV}$ are investigated. For this the fraction of pixels above a certain pixel count value threshold onto the pixel counts is plotted in Figure 31 for each

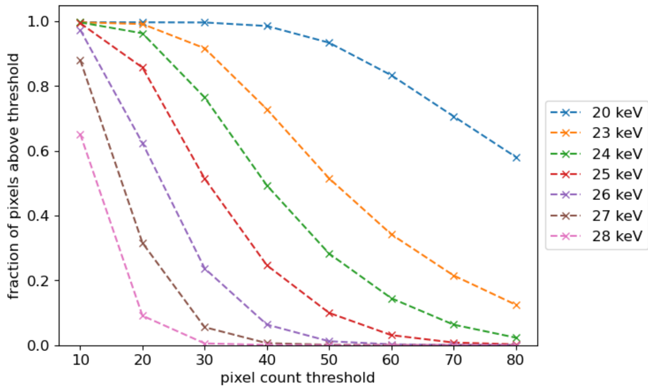

Figure 31: Fraction of pixel counts above a given threshold for a reference frame using $U_{\mathrm{B}} = 35\,\mathrm{kVp}$, $I = 10\,\mathrm{mA}$, and $t = 1\,\mathrm{s}$ for several different detector thresholds.

different measured detector threshold.
This shows that for $\mathrm{Th} = 20\,\mathrm{keV} \approx 60\,\%$ of the pixels have values above 80 and $\approx 38\,\%$ have counts from 40 to 80. Such rather broad distributions of pixel values are expected due to the moiré fringes. The fraction of pixels above a certain pixel count threshold decreases for every detector threshold increase. For $\mathrm{Th} = 28\,\mathrm{keV} \approx 90\,\%$ of pixel have values below 20 resulting in a possible inflated determination of visibility. Even for $\mathrm{Th} = 20\,\mathrm{keV}$ there is heavy grain noise due to insufficient counts for a stable visibility determination. Hence, increasing the frame acquisition time would be required to improve the photon statistics and stabilize the visibility determination. Due to the energy dependent absorption of photons in the object, there are less photons in the object image, which should be considered, when aiming for a photon statistics.
As a result $U_{\mathrm{B}} = 39\,\mathrm{kVp}$ with $\mathrm{Th} = 20\,\mathrm{keV}$ was chosen as the standard tube parameters, as it had a near-target visibility 30% of mean_vis $\approx 29.9 \pm 5.0$, with the highest counts compared to the other measurements, resulting in a decent compromise of visibility and counts.

5.4 Parameter evaluations using CT reconstructed phantoms

Comparison of CT reconstruction using the ASTRA-Toolbox and Mitos X-Aid

This work initially used CT reconstructions with the ASTRA-Toolbox, but this showed artifacts, like moon-like shapes of signals and double-image ghosting artifacts observed in the reconstructed volume. This hinted at errors in the reconstruction parameters. Therefore, reconstructions were performed using the commercially available Mitos X-Aid software to verify the geometry, and compared with the ASTRA-Toolbox reconstruction adapted with the parameters used in the X-Aid reconstruction. As a phantom, a cup containing six gummy-bears was used, as shown in Figure 32.
In two aluminum-oxide powder of size $d_p = 1.89\,\mu\mathrm{m}$ was placed in a cut after heating them in a cooking pot, two with powder placed in a cut without heating, and two with cuts without powder to investigate the dark-field signal caused by the cutting. As dataset, a measurement with parameters $U_{\mathrm{B}} = 39\,\mathrm{kVp}$, $\mathrm{Th} = 20\,\mathrm{keV}$, $I = 16\,\mathrm{mA}$, $a_{\mathrm{step}} = 0.5°$, $a_{\mathrm{sector}} = 360°$ and 7 phase-steps with 5 per G_0-period was used. Therefore, only

Figure 32: Plastic cup with six gummy-bears. Four gummy-bears contain aluminum-oxide powder of size $d_p = 1.89\,\mu\text{m}$. The upper right red and green gummy-bear do not contain aluminum-oxide powder. Image taken by Markus Schneider.

differences directly from the reconstructions are compared. The reconstructions were performed using cone-beam geometry and the FDK algorithm with an Hamming-filter applied in both reconstructions, since this filter was used for all Mitos reconstructions, as described in Chapter 4. The slices of the reconstruction volumes are shown in Figure 33.

A slice of the top view is shown in Figure 33a using X-aid, which shows overall clear signals of the gummy-bears and the powder within them. The corresponding slice of the ASTRA-Toolbox reconstruction is shown in Figure 33b. There, the gummy-bears can still be roughly made out, but the contours of some of them appear to be doubled and slightly mismatched. However, the signals of the powder objects are far spread out in curved lines, and no proper estimations can be made about their size. To better illustrate the doubling, the side view is shown in Figure 33c for Mitos and Figure 33 for the ASTRA-Toolbox. This is especially prominent in the powder of the left gummy-bear and the contour of the right gummy-bear. It is assumed that the error is caused by the still not correct projection geometry used, where the positions of the source and detector are represented as polar-coordinates relative to the position of the sample. This assumption is mainly based on the fact that when a reconstruction is performed with an angle sector of 180°, there appears an open side of the cup wall and on the opposite site a doubled cup wall, as shown in Figure 34. This reconstruction was obtained using the first half of the projections used for the reconstruction in Figure 33. This shows that the cup holding the gummy-bears is not a complete full circle and has a mismatch on the left side, where the doubling of the objects for $a_{\text{sector}} = 360°$ reconstructions is mainly caused by the mismatch of the projections with the ones shifted by 180°.

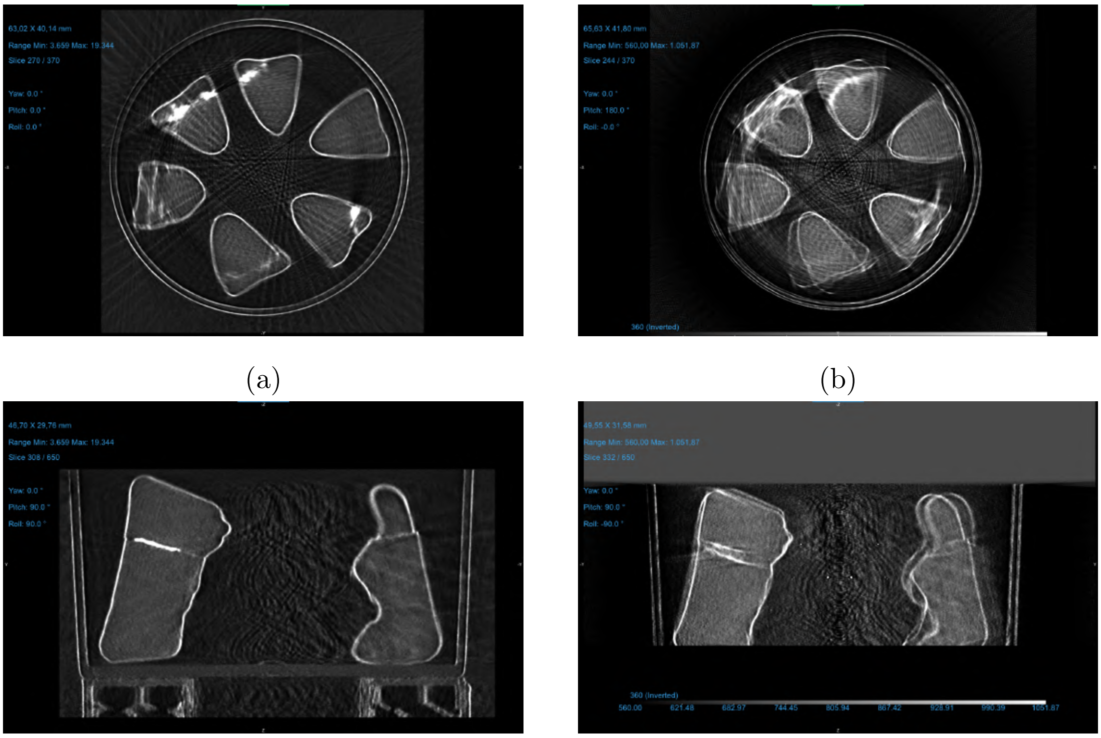

(a) (b) (c) (d)

Figure 33: Slices of the reconstructions from the top view in (a) using X-Aid and (b) using the ASTRA-Toolbox. Slices of the reconstructions from the side view in (c) using X-Aid and (d) using the ASTRA-Toolbox.

Comparison of standard and interlaced phase-stepping methods

As discussed in Chapter 2.6.3, the interlaced phase-stepping method generally achieves better reconstruction quality, when the same total number of frames is used for the reconstruction. This is due to the averaging of uncertainties at the cost of spatial resolution [Zan+11]. This indicates a higher time efficiency in terms of reconstruction quality in the interlaced method compared to the standard method. As such, an interlaced CT can potentially reach the same reconstruction quality in less time. To evaluate the measurement time reduction capability of the interlaced method, two measurements were performed with the same parameters, one using the standard method and one using the interlaced method. The same phantom as in Chapter 5.4 is used. Since both measurements have the same angle step size, the interlaced acquisition yields fewer overall object frames, reduced by a factor corresponding to the number of phase steps per scan. From this, a blurring of the reconstruction for the interlaced CT is expected and its extent is evaluated. The measurement parameters were $U_{\mathrm{B}} = 39\,\mathrm{kVp}$, $\mathrm{Th} = 20\,\mathrm{keV}$, $I = 16\,\mathrm{mA}$, $t = 5\,\mathrm{s}$, $a_{\mathrm{step}} = 0.25°$, $a_{\mathrm{sector}} = 185°$ and 7 phase-steps with 5 per G_0-period. The interlaced CT had a measurement time of $t_{\mathrm{M,interlaced}} \approx 70\,\mathrm{min}$, while the standard CT had a measurement time of $t_{\mathrm{M,standard}} \approx 511\,\mathrm{min}$. This corresponds approximately to the number of phase steps per scan, but is slightly larger due to additional time required in the standard CT for repositioning G_0 to its base position

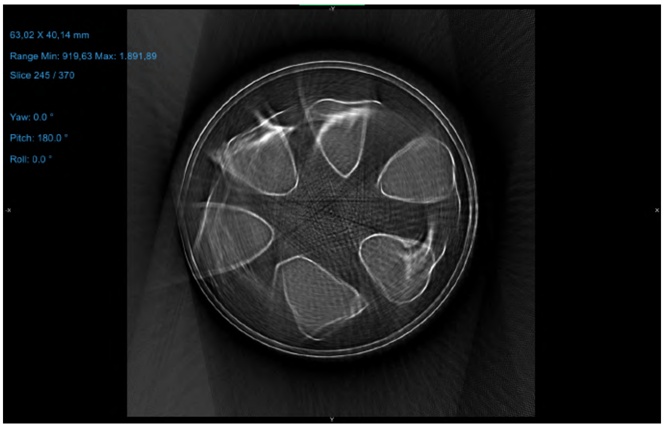

Figure 34: Slice of the reconstructions from the top view using an angle sector of 180° with the ASTRA-Toolbox.

after each scan. 2D slices of the reconstructed CT volumes, showing both dark-field and transmission images for the standard and interlaced measurements, are presented in Figure 35. Figure 35a shows a part of a 2D slice of the reconstructed dark-field volume acquired with the standard method, where Figure 35b was acquired with the interlaced method. Both are displayed over the same value range using a linear intensity mapping. The powder can be clearly differentiated from the gummy-bear in both, but the powder in the interlaced reconstruction appears more smeared compared to the standard reconstruction. In addition, small artifacts appear in Figure 35b spread over most of the image. These artifacts are more pronounced relative to the powder signal. Also, only in Figure 35a the gummy-bear is in contact with the side of the cup, because other measurements were performed between them and the phantom was moved. Therefore, they are not perfectly identical.

The transmission slices corresponding to these dark-field slices are shown in Figure 35c for the standard and in Figure 35d for the interlaced method. Compared to its dark-field slice, Figure 35c only shows the larger powder regions and the gummy bear exhibits a much stronger signal, whose grain-like noise further reduces the contrast to surrounding structures. In the transmission slice of the interlaced reconstruction, most powder structures are not identifiable within the noise of the gummy-bear itself. The grain-like noise is overall more prominent in the gummy-bear, and it also has a larger structure size than for the standard transmission slice. As a result, even the largest powder structures are barely visible.
Hence, the interlaced and standard phase-stepping method was compared, where the interlaced measurement time was shorter by roughly a factor of seven. Overall, the images of the standard method have a higher edge sharpness, which is due to the interlaced method recording by a factor of seven fewer phase-steps and using acquisitions of different angle positions. For the interlaced method, this time reduction leads to a significant degradation of the transmission reconstruction, where the powder regions are not identifiable anymore. In contrast, the interlaced dark-field reconstruction shows smeared but still identifiable powder regions. This indicates that, even with such a reduction in measurement time, the powder regions are still identifiable in the dark-field reconstruction. By using phase steps at closer angle positions in the interlaced

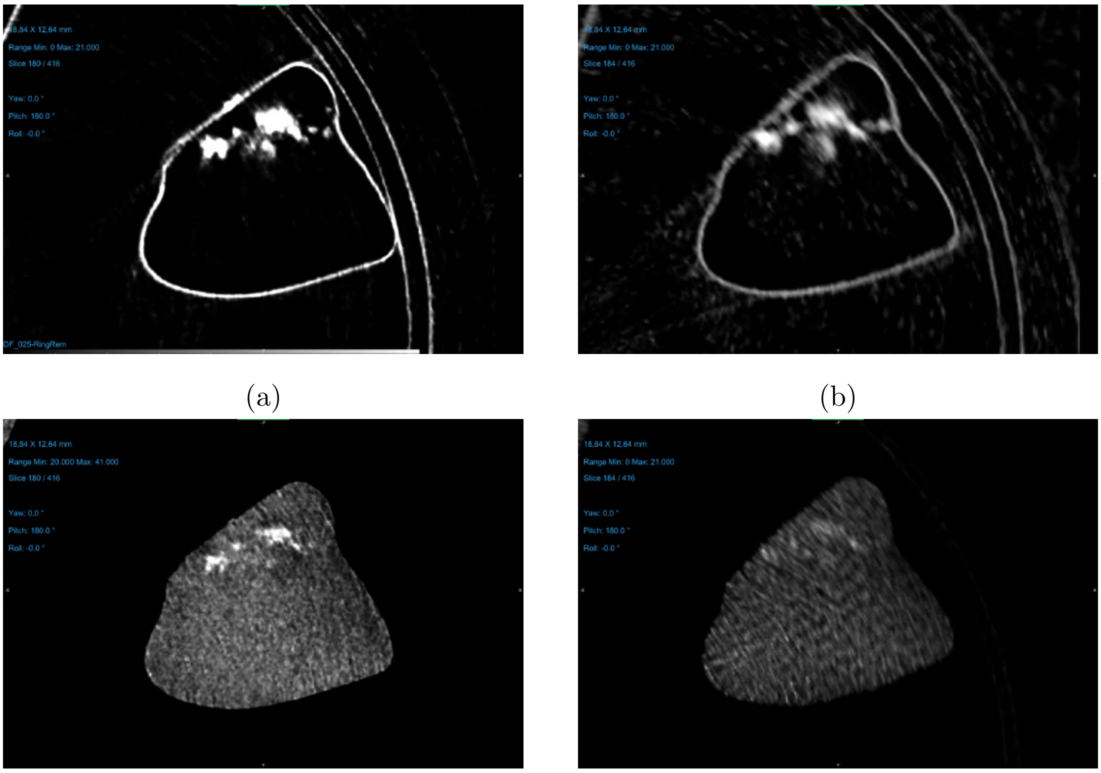

(a) (b) (c) (d)

Figure 35: Dark-field and transmission slices of the CT of a gummy bear phantom acquired with standard and interlaced scanning methods. Each figure corresponds to a slice of a CT reconstruction (a) dark-field of the standard method, (b) dark-field of the interlaced method, (c) transmission of the standard method, and (d) transmission of the interlaced method. Both scans were acquired using the same angle range and angle step size and all images are displayed over the same range of values of the reconstructions values with a linear mapping.

acquisition, effectively increasing the number of acquisitions, the edge sharpness could be improved. However, there would still be a gradient from a sharp center to a lower sharpness away from the center, which does not appear for the standard method. This also demonstrates the advantage of dark-field imaging over transmission imaging, as it yields a significantly higher contrast between the powder and the gummy bear.

Comparison of measurement time affecting parameters of CT reconstructions using the interlaced method

To investigate the optimal way to extend the measurement time for image quality, the interlaced method is used to perform CT measurements with different frame acquisition times and angle step sizes over an angle sector of $a_{\text{sector}} = 360°$. In contrast to the standard method for the interlaced method requires for each angle step size a separate measurement. Smaller angle sectors, however, can still be reconstructed from a 360° measurement by removing the additional projections. The same phantom as in Chapter

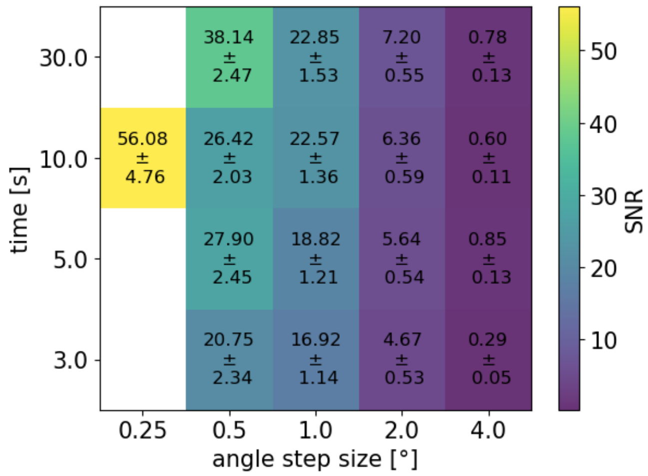

Figure 36: SNR as a function of frame acquisition time t_{acq} and angle step size a_{step}. The determined SNRs are displayed in color as well as with values, where the error is calculated from the standard deviation of the noise region.

5.4 is used. The measurements were performed using parameters $U_{\mathrm{B}} = 39\,\mathrm{kVp}$, $\mathrm{Th} = 20\,\mathrm{keV}$, $I = 16\,\mathrm{mA}$, $a_{\mathrm{sector}} = 360°$, $t = 3\,\mathrm{s}, 5\,\mathrm{s}, 10\,\mathrm{s}, 30\,\mathrm{s}$, $a_{\mathrm{step}} = 0.25°, 0.5°, 1.0°, 2.0°, 4.0°$ and 7 phase-steps with 5 per G_0-period. Since the CT reconstructions were achieved with Mitos, effectively 5 phase-steps with 5 per G_0-period were used. From the reconstructed volume, a 2D slice with powder region is selected, and used as the signal region, while an empty gummy-bear is used as the background region. The contrast between these regions divided by the standard deviation of the background is then evaluated using two-dimensional parameter maps.

In Figure 36 the SNR is shown as a function of frame acquisition time and angle step size, where each point represents a unique measurement and reconstructed CT volume based on the combination of the corresponding parameters. The SNR is determined by the contrast between a powder signal and an empty gummy-bear divided by the standard deviation of the empty gummy-bear. The standard deviation of the powder signal is neglected as additional details in the powder region also lead to an increased standard deviation, making the standard deviation of the powder region not comparable. The error of the SNR is calculated by the SNR times the standard deviation diveded by the mean of the empty gummy-bear.As expected, an increased frame acquisition time generally improves the SNR as a result of enhanced photon statistics. Similarly, smaller angle step sizes, corresponding to a higher number of projections, also lead to improved SNR due to increased sampling of the object, and can also improve the statistics due to statistical averaging of the used projections. A halving of the angle step sizes results in double the number of projections used in the reconstruction. For time entries, the increase from 3 s to 5 s is less than a factor of two, from 5 s to 10 s it doubles, and from 10 s to 30 s it triples. Generally, for reconstructions using $a_{\mathrm{step}} = 4°$ the edges of the gummy-bears are too smeared, so only their rough positions can be identified, which is also shown in the SNR being lower than 1. Hence, they are used only to demonstrate too low sample densities and only the smaller angle step sizes are further compared. Generally, an increase in measurement time improves the SNR, where

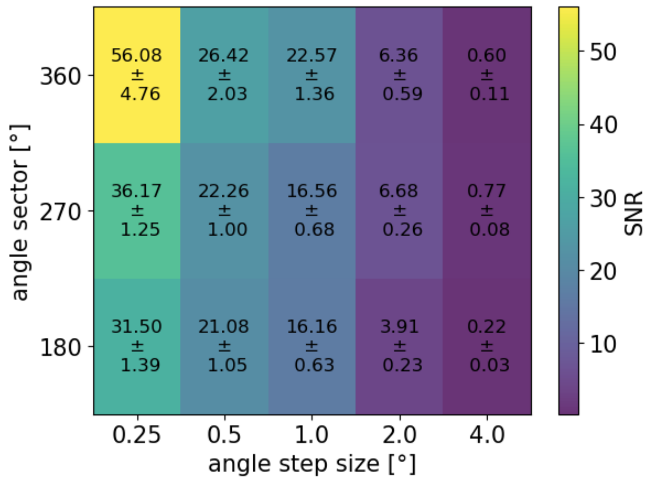

Figure 37: SNR as a function of angle sector a_{sector} and angle step size a_{step}. The determined SNRs are displayed in color as well as with values.

only $a_{\text{step}} = 0.5°$ and $t = 10$ is an outlier, but the frame time increase for $a_{\text{step}} = 0.5°$ and $t = 30$ also leads to a marginal increase in SNR, compared to other cases. The measurement time of the CT with $a_{\text{step}} = 1°$ and $t = 5\,\text{s}$ can be compared to one with double measurement time such as $a_{\text{step}} = 0.5°$ and $t = 5\,\text{s}$ and $a_{\text{step}} = 1°$ and $t = 10\,\text{s}$. While both measurements with the doubled measurement time have an increased SNR, the increase of the one with a smaller angle step size is much larger compared to the frame time. For $a_{\text{step}} = 2°$ and $t = 3\,\text{s}$, even a tenfold increase in frame time leads to a worse SNR compared to a twofold increased number of projections through a smaller angle step size. Such a large difference is not the case anymore for $a_{\text{step}} = 1°$ and $t = 3\,\text{s}$ and $t = 30\,\text{s}$, but halving of the angle step sizes still leads to higher SNRs compared to the frame time increases chosen.

In addition, the influence of the angle sector in combination with the angle step size is analyzed, as shown in Figure 37. The angle sector determines the total angle range over which projections are acquired. Therefore, more projections are used in the reconstruction, which improves the statistics. In the case of scattering, this could also lead to a different signal when X-rays are scattered before or after propagating through a larger portion of the phantom.

This shows only small improvements when increasing the angle sector from 180° to 270° at the same angle step size, with only a larger increase for $a_{\text{step}} = 0.25°$ and $a_{\text{step}} = 2.0°$. This might be due to the fact that, in FDK, projections beyond 180° increase the statistics and introduce weighting effects, which only influence all projections when a full 360° scan is used. Hence, in contrast this can even improve the 360° measurements. When comparing the increase in a 180° reconstruction to one requiring double the measurement time, either by doubling the angle sector or by doubling the number of projections through halving the angle step size, the reconstructions with the smaller angle step size show a slightly higher SNR in all cases, except for $a_{\text{step}} = 0.5°$ and $a_{\text{sector}} = 180°$ compared with $a_{\text{step}} = 1.0°$ and $a_{\text{sector}} = 360°$. Interestingly, for $a_{\text{step}} = 0.25°$ the increase from 180° to 360° is far larger compared to the other measurements. This could indicate that at such a high sampling density the additional information of 180°

shifted projections becomes significantly more beneficial.
It is assumed that the exact behavior differs significantly among different sample types, such as a gummy-bear with aluminum-oxide powder, tissue with calcifications, or tissue with calcifications embedded in another material. Therefore, to draw conclusions regarding calcifications of a given size in cancerous breast tissue, these functions should be measured on the specific calcification regions that are intended to be detected.

6 Samples embedded in formalin

In this chapter, five lamellae embedded in formalin are presented. Those were first analyzed using the scanner setup and then through CT measurements. Finally, the grating-based attenuation imaging is directly compared to conventional X-ray imaging by removing the gratings and recording projections. The aim of analyzing the samples was to detect DCIS calcifications within the cancerous lamella. This could only be achieved to some extend, as pathological confirmation of calcifications was only available for neighboring lamellae.

6.1 Measurements of samples embedded in formalin with the scanner setup

The formalin samples were first analyzed using the scanner, to investigate the image quality with higher visibility and the influence of the sample thickness by exploiting the different sample fill heights. The scanner only allows for the acquisition of single phase-stepping scans, where the phase-steps are recorded while continuously moving the object, instead of moving one of the gratings. The scanner setup is extensively covered in [Bal25]. The scanner setup also allows for an adjustable region of interest of roughly $40 \times 80\,\mathrm{cm}$, so that the projection resulting from the scans can contain all samples in the same measurement. All samples were measured using parameters $U = 50\,\mathrm{kVp}$, $I = 12.8\,\mathrm{mA}$, $f = 1\,\mathrm{mm}$ and 80 phase-steps with 40 steps per period. Overall, no significant structures could be identified within those measurements. Therefore, only the results of Sample 4 are presented here, which has an optical image shown in Figure 38.

In this sample, a piece of tissue protrudes from the formalin, which results in a slightly different signal compared to the tissue soaked in formalin, as observed in the other samples. The dark-field projection is shown in Figure 39 (left), while the transmission image in Figure 39 (right). A significant signal corresponding to the tissue protruding out of the formalin is observed, which is more pronounced in the transmission image. The other regions appear mostly homogeneous with small contrast deviations in the transmission image, that can be partly attributed to tissue, as it absorbs less than formalin. None of the samples yielded images containing significant objects that could be identified as calcifications.

In general, a limiting factor for this and further evaluation of such samples could be an excessive overall loss of intensity within the samples, mainly caused by the formalin. As such, for each sample an area was chosen as marked red in Figure 39 (left) to determine the absorption coefficient of the tissue-Formalin mixture, as shown in Figure 40. The absorption coefficient was calculated individually for each sample from the intensity loss and the sample fill height, since the tissue-formalin composition varies between samples and therefore leads to different effective path lengths of the absorbing material. Even with unknown different amounts of tissue in the chosen regions for each sample, a relatively similar absorption coefficient is obtained. An exponential fit of the form $f(x) = \exp(-\mu x)$ to the fraction of remaining photons, result in an overall absorption coefficient of $\mu = 0.27 \pm 0.01\,\mathrm{cm}^{-1}$, which results for the diameter of the sample in a remaining intensity of$I(3.2) \approx 42\%$. For other setups, tube voltages, detector and gratings, this is expected to differ.

6.2 CT measurements of formalin samples

This section presents the CT measurements of the formalin samples using the interlaced phase-stepping method. The interesting regions of each sample are analyzed. All measurements were performed with $U = 39\,\mathrm{kVp}$, $\mathrm{Th} = 20\,\mathrm{keV}$, $I = 16\,\mathrm{mA}$, $a_{\mathrm{step}} = 0.2°$, $a_{\mathrm{sector}} = 183.8°$ and 7 phase-steps with 5 per G_0-period. An angle sector of $a_{\mathrm{sector}} = 185°$ was recorded in the measurement, but for this measurement series, the interlaced acquisition was not yet adjusted. Therefore, only an angle sector of $a_{\mathrm{sector}} = 183.8°$ is used for the CT reconstruction, since acquisitions before and after the angle position are needed for an interlaced phase-stepping scan.

Sample 1

In the first sample, only a large metal wire was identified, causing strong streaking artifacts. As such, no interesting objects could be observed, and the detailed description of the reconstructed sample in dark-field and attenuation starts with Sample 2. The dark-field reconstruction shown in Figure 41 illustrates the metal wire and the plastic cup containing the lamella and Formalin. The wire most likely originated from a surgical compress used during sample preparation. No other objects besides the wire could be clearly identified, either because the streaking artifacts obscure surrounding regions or because the strong contrast spreads the maximum CT values over a larger area, reducing the contrast of small signal differences. Trivially, since only confirmation of calcification in the neighboring lamella to the observed one exists, it could also be possible that no calcification are present in this sample.

Sample 2

A rough overview of the highly absorbing or scattering regions can be made by illustrating the maximum CT values over a volume in a single 2D view using Dragonfly. As the dark-field usually shows a strong signal from the sample cup, the top-view is more suited to display the sample, as the cup walls overlap with itself instead of the sample. The display of the maximum values of multiple slices is called the maximum slab, which effectively represents the maximum values of a volume in a 2D view. In Figure 42 (left), a slice of the transmission CT reconstruction is shown, which has the height marked in purple used for the maximum slabs shown in 42 (middle) for the transmission and in 42 (right) for the dark-field. Here, the following dark-field images are all shown with a red color-scheme, while the transmission images are displayed as grayscale. Maximum slabs allow large signal structures to be compared between dark-field and transmission images, similar to a top-view projection that does not preserve information about the depth and whether the signal originates within tissue or Formalin. Therefore, using the slabs the signal regions are classified, and from the interesting regions also a 2D slice is shown for comparison. The regions are classified by numbers for each sample, and by color to indicate a pronounced transmission contrast with small or no dark-field signal (green), a similar contrast between dark-field and transmission (yellow), and a stronger dark-field contrast (blue). For this sample, six larger interesting structures were found, whereas some tiny spherical objects appearing in both modalities have not been labeled. Region 3 shows multiple spherical objects assumed to be calcifications, that are both visible in transmission and dark-field, which is expected for larger solid calcifications generally of

size > 100 µm. Additionally, this region also contains a diffuse line-like structure that is also both visible in dark-field and transmission, which cannot be clearly categorized. Region 6 contains a large object that is only visible in the dark-field, which is from the pathology assumed to be a cotton thread from the preparation of the sample.
Regions 1 and 2 are further analyzed using side view slices, as shown in Figure 43. Generally, it is difficult to compare the signal strengths inside a CT reconstruction between different modalities such as dark-field and transmission, as they depict completely different value ranges. Further, the reconstruction values are stored as 16-bit values, where the minimum value corresponds to 0 and maximum value to 65535. With a strong dark-field signal like from the cup wall, this could spread out the values leading to a smaller value difference between calcifications and background. This could be partially adjusted by clipping of values, but this can also introduce errors. Since the highest and lowest values different between modalities, their effective value range of signals also corresponds to different signals strengths. As such, only the relative contrasts of objects of different modalities can be compared. The CT volume could also be displayed with their original values, but this leads to worse contrasts and a more difficult display of small changes, and not used here. As a result the CT values are linearly color mapped over a range that shows a contrast between calcifications, tissue and formalin, and effectively only the relative contrast between calcifications and tissue or formalin can be compared. In this case the dark-field shows a range of 5843 and the transmission over a range of 10292.
The presented slices demonstrate a large contrast between the tissue and formalin in the transmission images. This contrast is reduced in the dark-field modality as both materials yield a signal close to the background, which can result in a larger contrast of calcifications in the dark-field. Region 1 shows a calcification at the edge of the tissue that has a more pronounced contrast in the transmission image compared to the dark-field. This is possible for larger dense objects, whose internal structure is relatively homogeneous on the microscopic scale. Region 2 shows a diffuse signal region in the dark-field and in the transmission a signal comparable to the highest formalin signals, but partially higher than the surrounding formalin. Oddly, a small object with lower transmission signal is visible within the central region of the higher transmission signal region. Therefore, the whole region could be formalin with a piece of tissue floating in the middle, or a small region without calcifications surrounded by a region with calcifications that slightly increase the absorption. Since there is no confirmation of the exact object, it could also be a material similar to the cotton thread in Region 6. Ideally for this investigation, this region could correspond to a diffuse cloud of microcalcifications that is well visible in the dark-field but produces only a weak transmission signal. Region 4 is shown in Figure 44 and displays a region with greater contrast in the transmission image located at the edge of the tissue. Opposite to region 1, this is not a particularly dense object, as the transmission contrast is also weaker, but the signal covers a larger area. As there is no ground truth for this object, it could not be further identified.

To highlight and compare stronger dark-field signals with transmission signals, they can also be visualized simultaneously in Dragonfly, as shown in Figure 45a. Here, the display of the dark-field values has been adjusted so that only higher dark-field values are displayed in red, whereas lower dark-field values are hidden behind the transmission image. The object chosen to highlight was region 2, as it is assumed to be the most relevant region to investigate microcalcifications. To illustrate the contrast between the modalities for this sample, a line plot through the slice is shown in Figure 45b. It should be noted that the CT values are determined by the maximum and minimum values of the measured volume and saved as 16-bit numbers. Therefore, only the relative contrast of each measurement can be compared, and not the direct values between measurements of different modalities. This shows a large dark-field signal at the air to sample cup transition, as there is a large refractive index gradient between the cup and air and possible microscopic surface roughness of the sample cup. Further, only a significant peak corresponding to the object in region 2 can be seen in the dark-field. A peak can also be seen at this location in the transmission, but also several other peaks of the same height and an overall stronger signal from formalin in the center of the sample.

Sample 3

Sample 3 contained several objects that yielded larger signals in the dark-field than in the transmission reconstruction, as shown in Figure 46. In regions 1, and 2, the objects in the dark-field image show a slightly larger area and contrast, whereas region 4 only shows an improved contrast due to less homogeneous surroundings. Region 3 has been marked yellow as in the transmission reconstruction additional artifacts are introduced in the center of rotation, which mainly improved the display of this region.
In Figure 47 the side view of regions 1 and 2 is displayed.
This shows especially for region 1 a better identifiable object in the dark-field image, whereas the object in region 2 also shows a clearer signal, but can already be well identified in the transmission image. Also, both objects are located at the edge of the tissue.
The side view of regions 3 and 4 is shown in Figure 48. Neither object can be clearly identified in the transmission reconstruction, as reconstruction artifacts produce more pronounced signals. Only for the dark-field image object in region 3 can an object in the transmission image be associated. For region 4, the dark-field signal appears more diffuse, and in the transmission image it appears as formalin region, whose values are in the lower range for the formalin in the sample. Therefore, region 4 is another strong candidate for a diffuse cloud of microcalcifications producing a scattering signal, similar to Sample 2 region 2. The side view of Regions 5 and 6 is presented in Figure 49. Region 5 shows left the wire and right the larger object, which can be well identified in both modalities. Region 6 shows an overall more pronounced signal in the transmission.

Figure 38: Optical photo of Sample 4. In a plastic cup tissue is embedded in formalin. For this sample, on the right, a piece of tissue sticks out of the formalin.

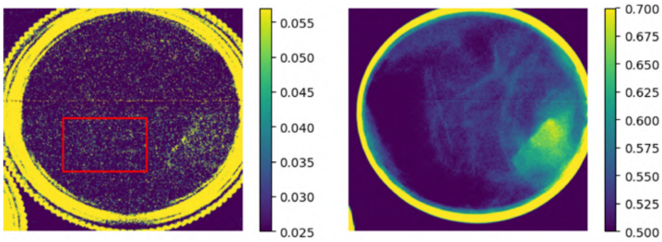

Figure 39: Projections of Sample 4 acquired using the scanner setup. Dark-field (left) and transmission (right) image right. The contrasts of both images have been narrowed to display changes within the cup. This has a significant signal corresponding to the piece protruding the formalin. The transmission also shows a darker region on the left from tissue absorbing less than formalin.

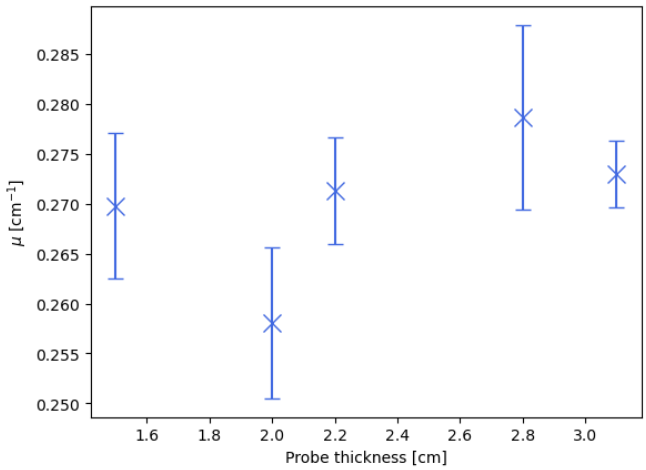

Figure 40: Absorption coefficients calculated from the remaining photons propagating through a sample and their different fill heights.

Figure 41: 3D image of the dark-field reconstruction of Sample 1. A strong dark-field signal originates from the air-cup transition and a large metal wire. This wire is a contamination of the sample and is surrounded by its strong streaking artifacts.

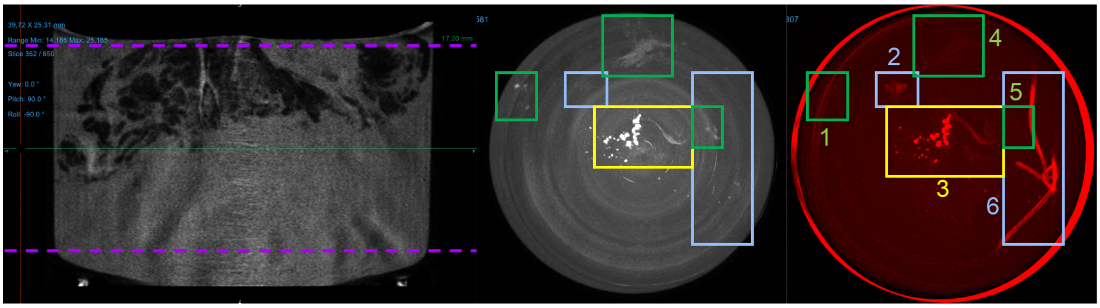

Figure 42: (Left) transmission slice of the reconstructed volume of Sample 2. In purple are the heights used to create a maximum slab to show the high signal objects in the whole volume. (Middle) transmission slab and (right) dark-field slab with the regions containing significant objects marked, depending on the contrast of the modalities. In yellow are the objects marked with a strong contrast in both modalities, green with stronger contrast in transmission, and blue with stronger contrast in the dark-field image.

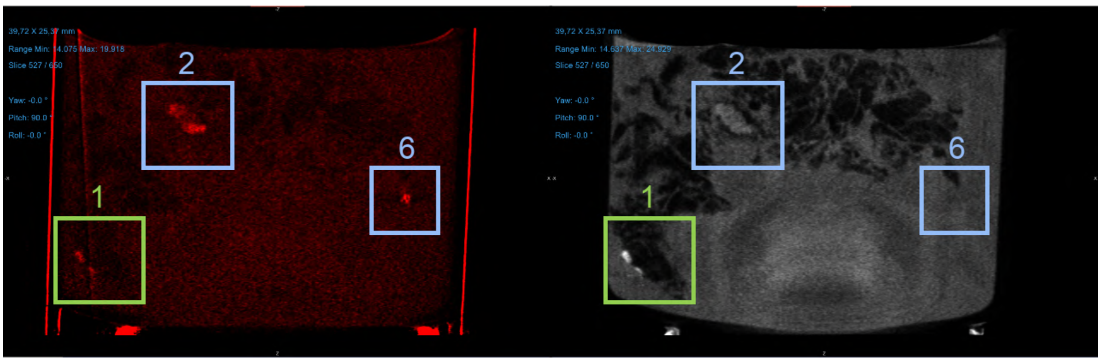

Figure 43: Slices of the reconstructed volumes of Sample 2 displaying the position and surrounding of regions 1, 2 and 6. (Left) dark-field and (right) transmission image.

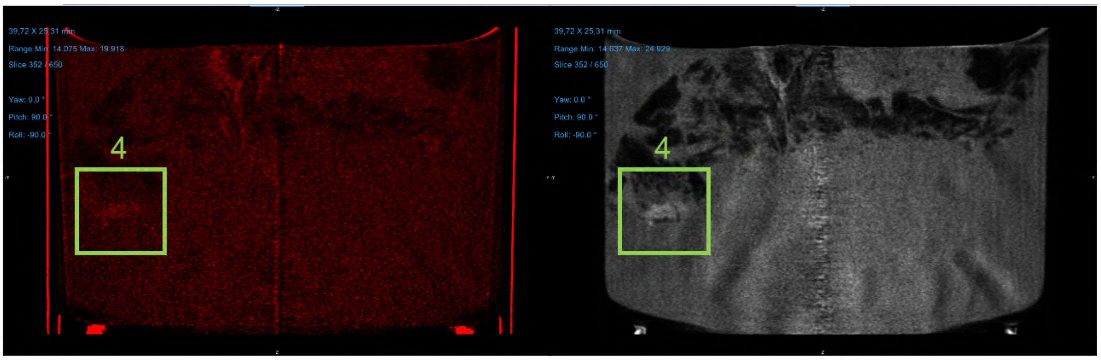

Figure 44: Slices of the reconstructed volumes of Sample 2 displaying the position and surrounding of regions 4. (Left) dark-field and (right) transmission image.

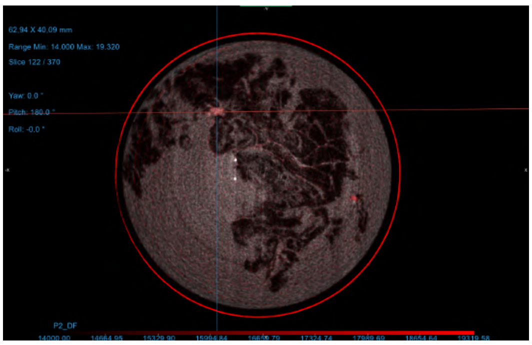

(a).

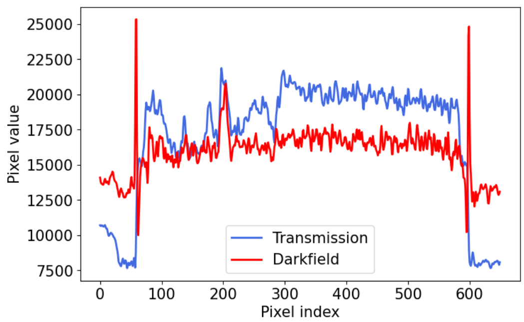

(b).

Figure 45: (a) Top view slice of Sample 2, whose height corresponds to region 2. Both image modalities are displayed, whereas it was adjusted to only overlay the transmission with large dark-field signals. (b) Line plot of CT values of the vertical marked line in 45(a).

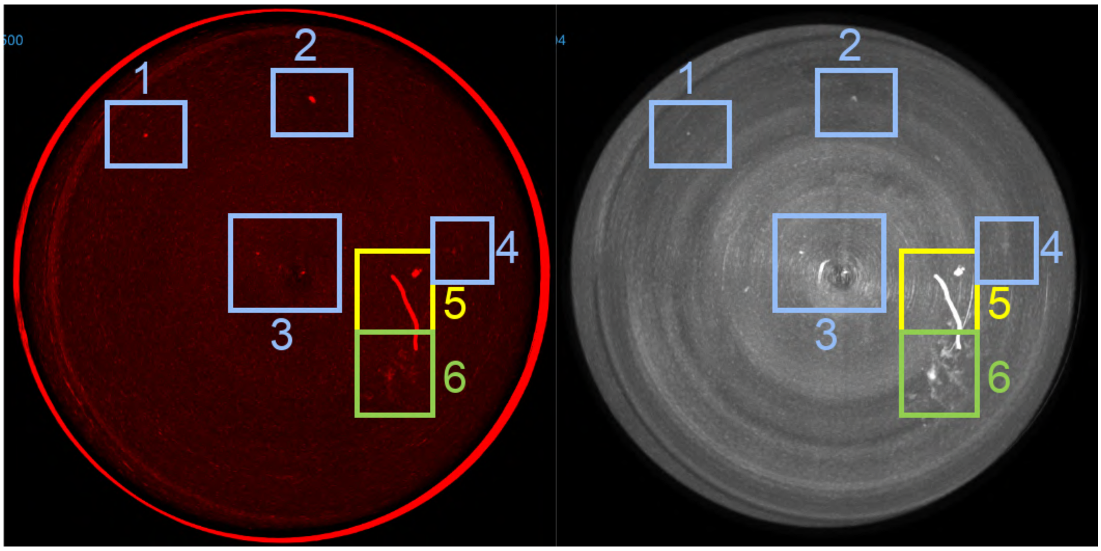

Figure 46: (Left) dark-field slab and (right) transmission slab of Sample 3 with the regions containing significant objects marked. In yellow are the objects marked with a strong contrast in both modalities, green with stronger contrast in transmission, and blue with stronger contrast in the dark-field image.

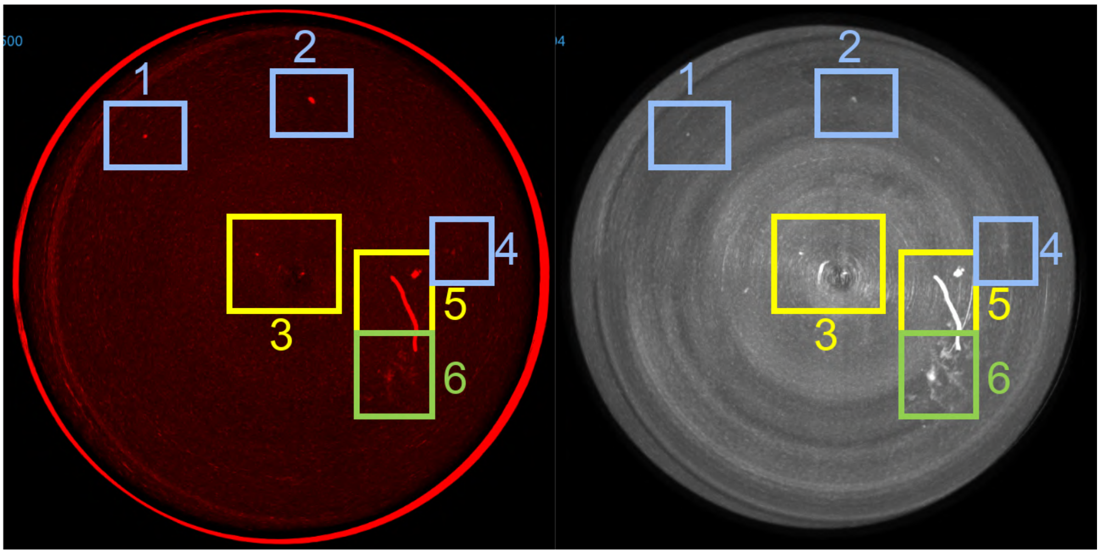

Figure 47: Slices of the reconstructed volumes of Sample 3 displaying the position and surrounding of regions 1, 2. (Left) dark-field and (right) transmission image.

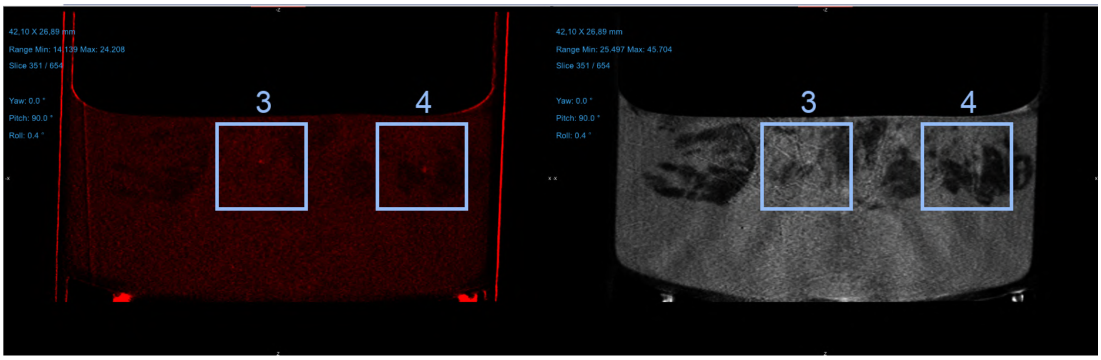

Figure 48: Slices of the reconstructed volumes of Sample 3 displaying the position and surrounding of regions 3, 4. (Left) dark-field and (right) transmission image.

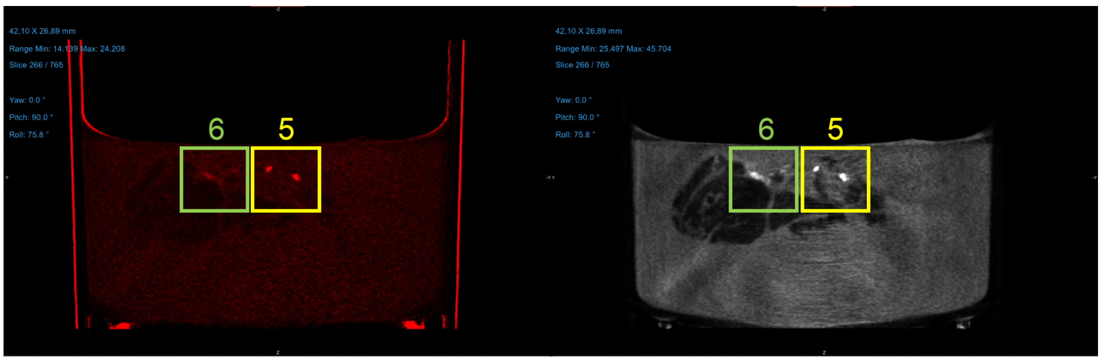

Figure 49: Slices of the reconstructed volumes of Sample 3 displaying the position and surrounding of regions 5, 6. (Left) dark-field and (right) transmission image.

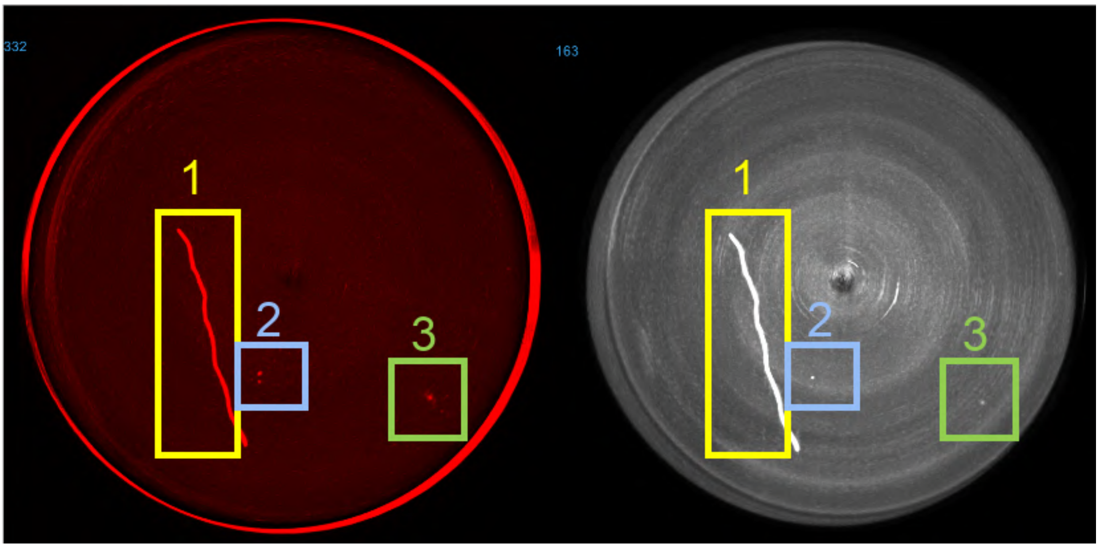

Figure 50: (Left) dark-field slab and (right) transmission slab of Sample 4 with the regions containing significant objects marked. In yellow are the objects marked with a strong contrast in both modalities, green with stronger contrast in transmission, and blue with stronger contrast in the dark-field image.

Sample 4

For Sample 4, the maximum slabs with the large contrast objects marked are shown in Figure 50. In region 1 another metal wire is visible that originates from the pathologic preparation of the sample.

Regions 2 and 3 show small spherical objects whose surrounding material is presented in Figure 51. The object in region 3 is visible in both the dark-field and the transmission image. In region 2, only in the dark-field image three objects are barely visible, where one object is directly over another, resulting in a slightly larger object in Figure 50 through projective overlap.

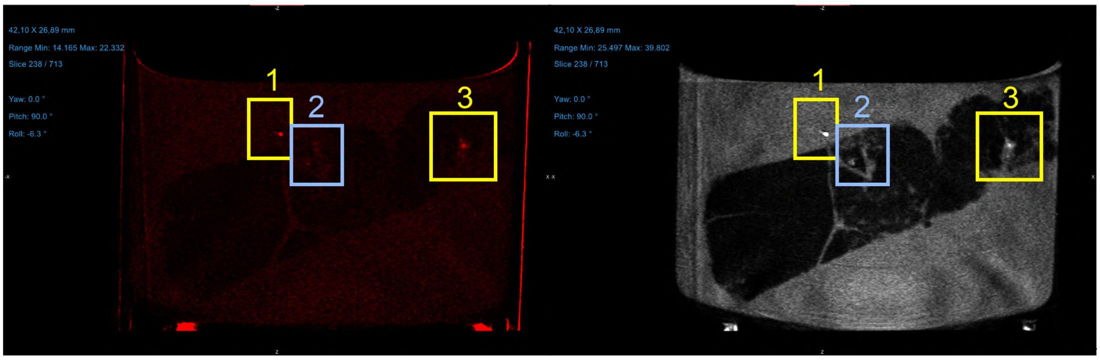

Figure 51: Slices of the reconstructed volumes of Sample 4 displaying the position and surrounding of regions 1, 2, and 3. (Left) dark-field and (right) transmission image.

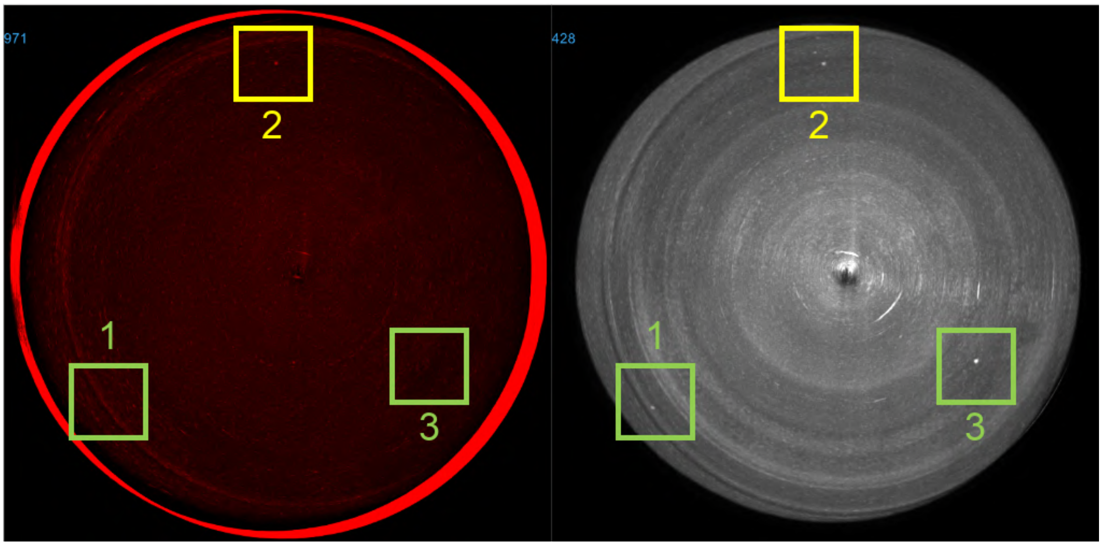

Figure 52: (Left) dark-field slab and (right) transmission slab of Sample 5 with the regions containing significant objects marked. In yellow are the objects marked with a strong contrast in both modalities, green with stronger contrast in transmission, and blue with stronger contrast in the dark-field image.

Sample 5

The maximum slabs of sample 5 with the large contrast objects marked are shown in Figure 52. For this sample, only small spherical objects were detected, whose surroundings and location are shown in Figure 53. In the upper images of Figure 53, region 2 is displayed, which shows a small spherical object decently visible in both modalities, that is located at the edge of the tissue. In the lower images of Figure 53, regions 1 and 3 are presented, while region 1 cannot be associated with any tissue and might have detached itself from the tissue. It could also be just a contamination of the sample as it is located at the bottom of the sample container. Region 3 shows a small spherical object that has a larger contrast in the transmission and is located at the edge of tissue.

6.3 Comparison of X-ray imaging and grating based X-ray imaging

In Chapter 6.2, only small amounts and small sized calcification candidates were identified with the exception of Sample 2 region 2. Therefore, in this chapter, longer projections with gratings and without gratings are compared, as in clinically used task specialized X-ray setups, calcifications are measured only using projections. It should be noted that those clinical X-ray images of the extracted tumor are acquired for the complete extracted material without embedding it for preservation, for example in materials like formalin.
First, 40 consecutive phase-stepping scans were recorded using $U = 39\,\mathrm{kVp}$, $I = 16\,\mathrm{mA}$, $\mathrm{Th} = 20\,\mathrm{keV}$ and $t = 10\,\mathrm{s}$ and 7 phase-steps with 5 per G_0-period, resulting in phase-stepping scan time of $t_{\mathrm{projection}} \approx 70\,\mathrm{s}$. For each object scan a separate reference scan was recorded, and the mean of the 40 projections calculated. The resulting transmission image is shown in Figure 54a and only yields the calcification of region 3 and no finer

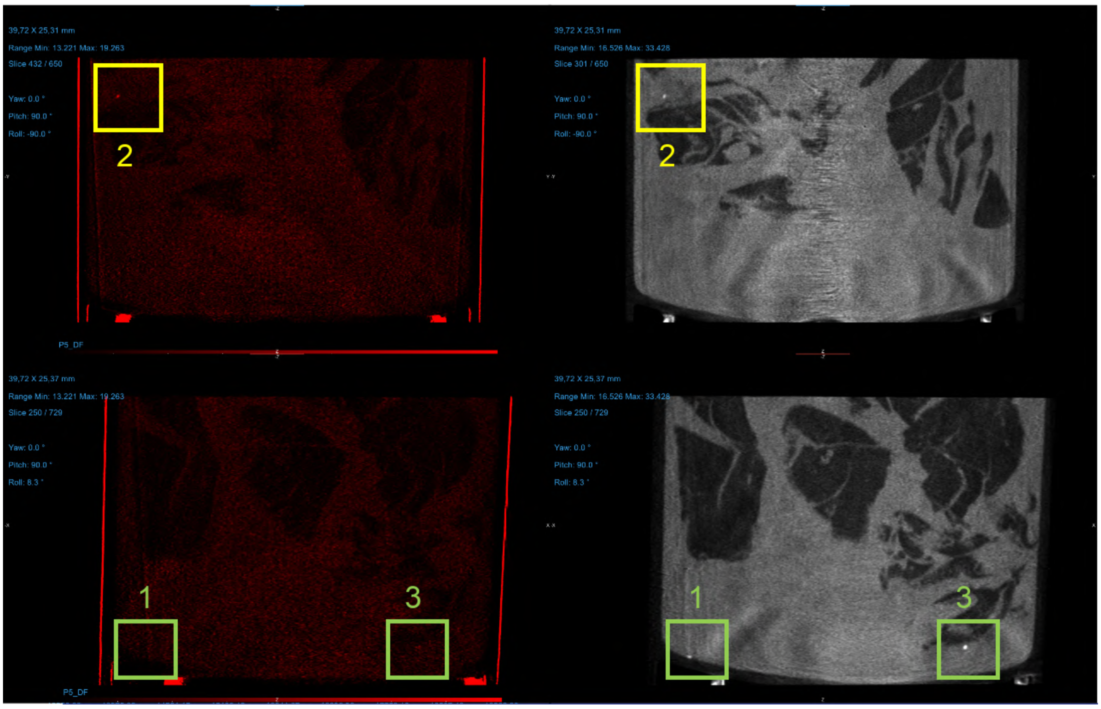

Figure 53: Slices of the reconstructed volumes of Sample 5 displaying the position and surrounding of regions 1, 2, and 3. (Upper and lower left) dark-field and (upper and lower right) transmission image.

details, but highlights the disadvantages of transmission imaging for samples with different thicknesses.

On the left and right, the sample is less thick, which yields a lower signal compared to the full sample thickness in the middle. In addition, in the middle there is a mixture of tissue, calcifications, and formalin, which produces an overall lower signal compared to only formalin. Consequently, the calcifications are only visible because they are surrounded by larger amounts of tissue. In the dark-field image, shown in Figure 54b, also the objects of regions 2 and 6 are well visible and thickness dependence detail loss is far suppressed, as primarily only the statistics are reduced. In addition, a slight contrast that might be attributed to tissue and formalin is also visible, which is slightly reduced around the object in region 2.

Afterwards, the gratings were removed and 40 consecutive images were recorded using $U = 30\,\mathrm{kVp}$, $I = 12\,\mathrm{mA}$, $\mathrm{Th} = 20\,\mathrm{keV}$ and $t_{\mathrm{projection}} = 10\,\mathrm{s}$. Ideally, the same dose and the same spectra arriving at the object should be used for the comparison. However, the spectra downstream of the G_0 was not measured, and its energy-dependent absorption not tried to recreate, and only the tube voltage and current were reduced to account for the increased flux due to no gratings. $U = 30\,\mathrm{kVp}$ was chosen as it is closer to the typical energies used in mammography [Rin+73]. The resulting transmission image of Sample 2 is shown in Figure 55. The color-scale of Figure 55a shows a broader distribution of values to display the full sample, while for Figure 55b this is narrowed to enhance the contrast of calcifications. Those only yield the calcification of region 3 and no finer details and no significant improved image quality as Figure 54a. The absorption

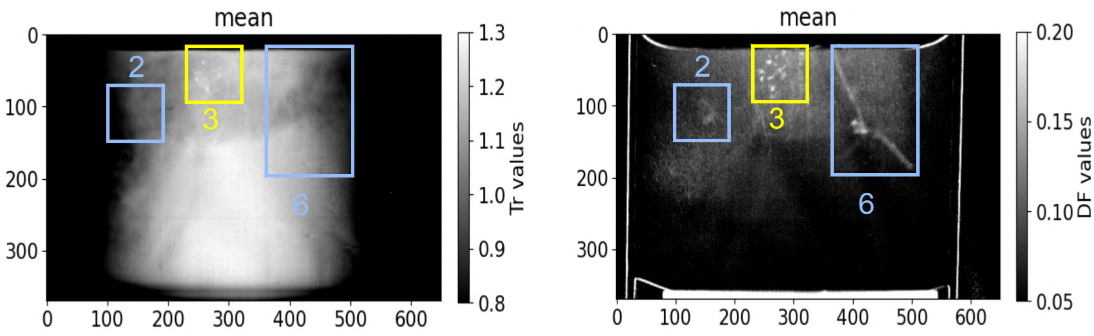

(a). (b).

Figure 54: Transmission (a) and dark-field (b) image of a projection of Sample 2.

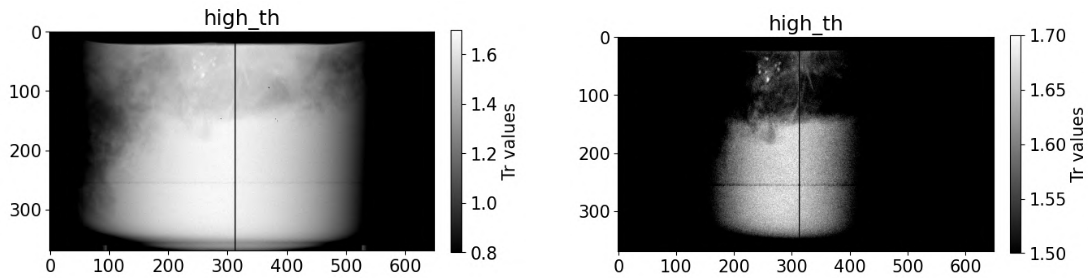

(a). (b).

Figure 55: Transmission image of Sample 2 acquired as a conventional X-ray image, without the use of a Talbot-Lau interferometer. In (a) the visible contrast was adjusted to display the edges of the sample. In (b) the windowed range was reduced to highlight objects within the tissue.

values are expectedly different, since a lower tube voltage was used, in addition to more lower energy photons remain in the spectrum without gratings, that are more likely to get absorbed in the sample. As a consequence, the the dark-field image yields a much improved contrast of objects within mostly homogeneous material with different X-ray path lengths in the object. Furthermore, using CT reconstructions instead of projections allows for a massively improved contrast of objects and tissue, as well as allow a determination of their position in the volume.

Discussion of formalin sample results

In the formalin samples, several candidates for calcifications and also candidates for microcalcification clouds could be found. The latter most notable candidates are in Sample 2 region 2 and Sample 3 region 4. Interestingly, nearly all candidates for calcifications were found at the edge between tissue and formalin, where the calcifications were expected to be within the tissue. This could be either a selection bias, where only the neighboring lamella was always selected, or it could also be that formalin fills the calcification regions differently compared to solid tissue. For example, an empty milk duct with calcifications might be filled with formalin, which then shows a

formalin signature in the transmission. Also, several contaminations were found from the preparation of the sample, which can degrade the reconstruction if they reach larger signals than the rest of the sample.
The main limitation in investigating the formalin samples was the lack of ground truth, since calcifications had only been confirmed in neighboring lamellae. Therefore, only possible calcifications could be observed as there is no confirmation. As such, only the transmission and dark-field signal in both reconstructions could be compared and not a calcification in both modalities.

7 Samples embedded in paraffin

This chapter presents nine tissue samples embedded in paraffin. The samples were provided by the "Pathologie Uniklinikum Erlangen" and analyzed using histological staining as ground truth and their correlation to the dark-field and transmission CT reconstructions determined.

Pathologic procedure of sample preparation

In the pathological procedure, the lamella are first fixed in formalin to preserve the cellular structure. After fixation, the lamella is dehydrated, cut to smaller disks, and cleared to prepare for embedding molten paraffin wax. When the paraffin block has solidified, very thin sections are cut from the surface of the paraffin block using a microtome, usually 3 to 5 µm thick. These sections are then placed on slides for staining to highlight tumors or calcifications and then examined under a microscope. Commonly, the Hematoxylin-Eosin (HE) staining is used for this purpose [Par07]. However, in this thesis the Von-Kossa-stain is evaluated as it highlights calcifications.

Von-Kossa-stain

The Von-Kossa-stain allows the detection of mineralized calcium deposits, such as calcium phosphate and calcium carbonate, in tissue sections. Applying a silver nitrate solution to the tissue causes the silver ions to react with the phosphate and carbonate anions of the mineralized calcium deposits. Light exposure reduces the bound silver to metallic silver, which appears black in light microscopy [Sch21]. The morphology of the calcifications allows for tendencies of benign and malignant lesions [Par07]. This is beyond the scope of this work, and it is focused on their density and size. An example of calcifications in the Von-Kossa-stain is shown in Figure 56. In the center is a milk duct that has within its clearly defined edge a white film and contains calcifications, which allows a classification as DCIS. The calcifications are sparsely distributed inside the milk duct, where on the middle right a larger calcification cluster is located. On the left is a larger calcification with a maximum diameter of $\approx$ 400µm. Since this calcification contains many sharp, line-like edges, it appears that during the section cut tearing occurred, making a clear classification of the surrounding tissue difficult. Calcifications that extend outside the milk duct may indicate invasive breast cancer, but such features have not been further investigated.
An example of invasive cancer in that has breached through its original cell and is spreading into adjacent tissue is shown in Figure 57. This shows mainly cell nuclei, whereas their breaching decided their malignancy [Par07].

Sample selection and sectioning procedure

Initially, the pathology used HE-stained sections to select DCIS samples. After the selection of a sample, a new section was cut for Von-Kossa-staining. This section cut begins with an approximately 150-250 µm cut to create a flat surface. Therefore, the structures of both stained sections appear significantly different, and the details of the HE-stained sections cannot be correlated to the CT reconstruction of the surface of the

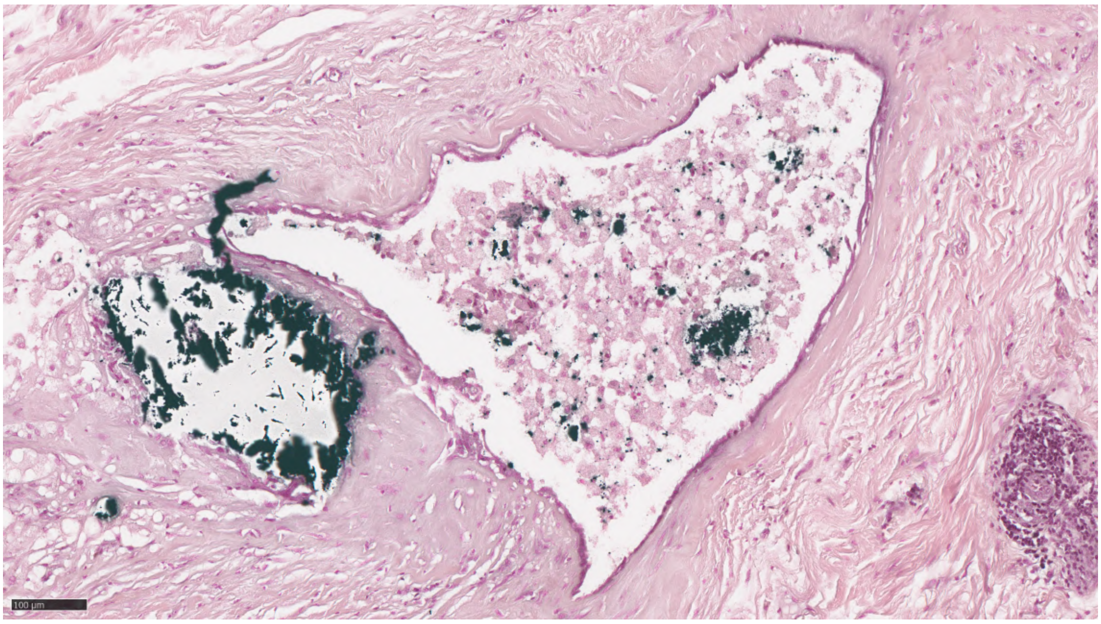

Figure 56: Calcification of the Von-Kossa-stained section of sample 12. The displayed area is 1900 µm × 960 µm.

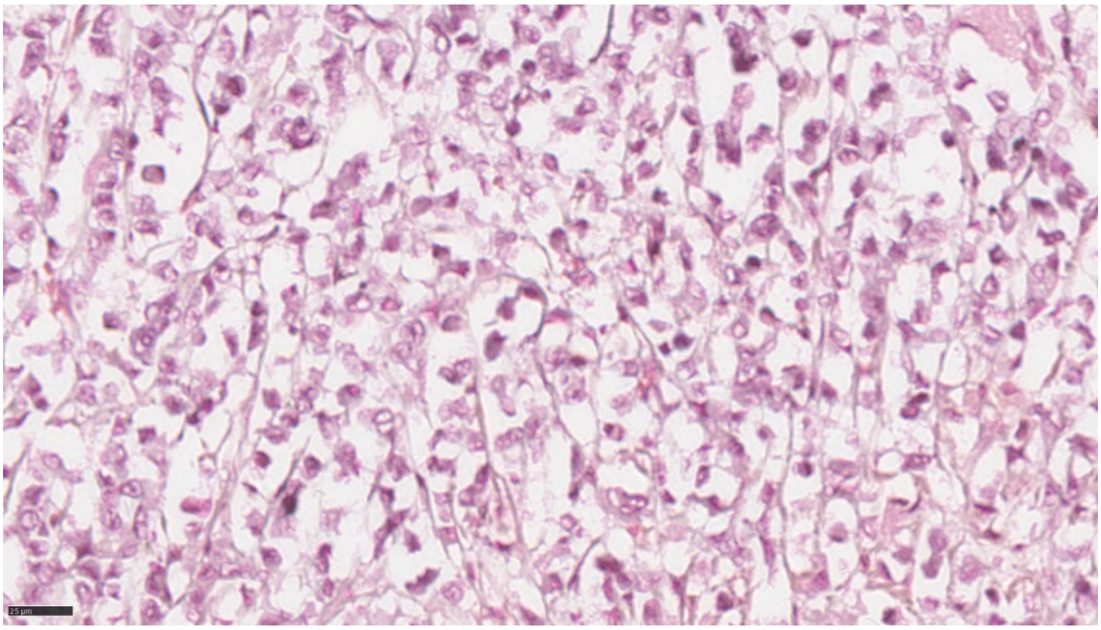

Figure 57: Invasive cancer spreading into adjacent tissue. The displayed area is (425 µm × 240 µm).

paraffin. The Von-Kossa should be 3 to 5 µm away from the surface, which allows a correlation of calcifications.

(a). (b). (c).

Figure 58: Sides of the paraffin sample. (a) Paraffin side with the tissue embedded, (b) plastic backside of the sample with the identification removed, (c) thickness of the sample. Overall the sample has dimensions 3.9 cm x 2.6 cm x 0.8 cm, whereas the paraffin in the samples has thickness of up to 40 mm.

7.1 Sample structure and ground truth

The provided paraffin blocks containing the tissue sample are fixed to a plastic holder during wax hardening, as shown in Figure 58. Figure 58a shows the paraffin with the tissue embedded, Figure 58b shows the plastic backside of the sample with the identification removed, and Figure 58c shows the thickness of the sample. Overall the sample has dimensions 3.9 cm x 2.6 cm x 0.8 cm.

The paraffin blocks were then measured using the Talbot-Lau interferometer in CT setup 2 to create dark-field and transmission CT reconstructions. Since the stained sections are cut off before the CTs were measured, they were not in the investigated sample, but near its surface. As such they do not yield the perfect ground truth of calcification positions, size, density, and grain size for the CT measurements. In addition the stained sections have thicknesses of 3 to 5 µm, while the CT voxel size is $\approx 60\,\mu m$. This approach could be improved by creating another stained selection from within the sample after a CT measurement was performed. However, this would still lead to an averaging of structures with the much larger voxel size compared to the ground truth. After the CT measurement, multiple consecutively stained sections could be performed to approximate a total thickness of 60 µm. However, this approach would be time-intensive, and the sectioning process often introduces tears that render the section unusable.

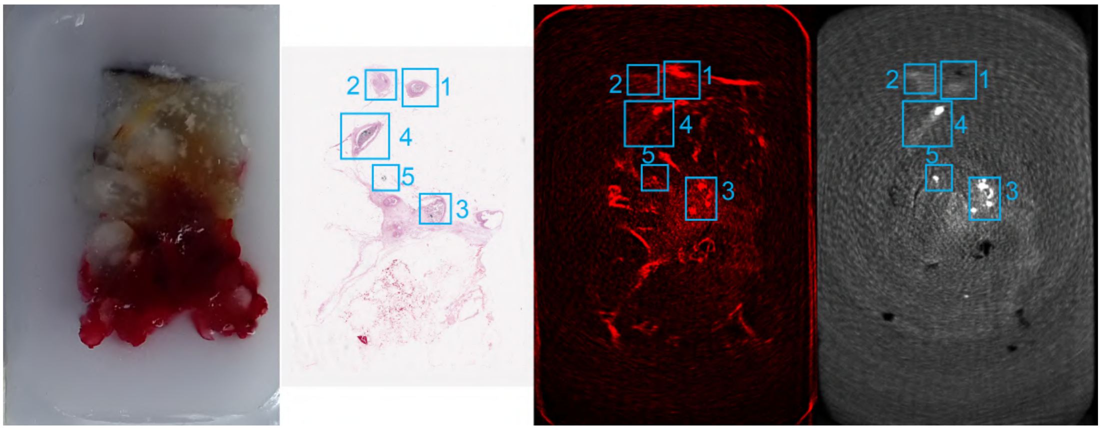

(a) (b) (c) (d)

Figure 59: Optical image (a), Von-Kossa-stained section (b), dark-field image (c), and transmission image (d) of Sample 6. For the dark-field and transmission images, a maximum slab of the paraffin surface with a thickness of 180 µm from the CT-reconstructed volume is shown.

7.2 Overview samples embedded in paraffin

All samples were first measured with the surface parallel to the sample holder and the paraffin positioned in the highest visibility region. For the measurement parameters $U = 39\,\text{kVp}$, $\text{Th} = 20\,\text{keV}$, $I = 16\,\text{mA}$, $t = 10\,\text{s}$, $a_{\text{step}} = 0.5°$, $a_{\text{sector}} = 185°$ and 7 phase-steps with 5 per G_0-period were used, resulting in an overall measurement time of roughly 71 min.
Those measurements revealed, that only three of the nine samples allowed for a well matching correlation of calcifications between the Von-Kossa-stained section and the surface of the paraffin sample in the dark-field and transmission CT reconstruction. Therefore, sample 6 and sample 7 are presented to showcase poorly matching structures between Von-Kossa-stained section and CT reconstruction. Only the images of the well matching samples 10, 12, and 13 are listed, as they were measured again over a longer duration and adjusted parameters to reach better reconstruction quality.

Sample 6

The comparison of the Von-Kossa-stained section with the dark-field and transmission image of Sample 6 is shown in Figure 59. The optical image is shown in Figure 59a, the Von-Kossa-stained section in Figure 59b, the dark-field in 59c and the transmission image in 59d. The dark-field image uniquely exhibits several line-like structures that could indicate tears in the paraffin or inhomogeneities while hardening of the paraffin. In addition, there are dark-signals that can be correlated to the edges of very low absorbing structures in the transmission, which indicate air-transition or air-bubbles.
For this sample, the Von-Kossa-stained section only shows a few similar structures compared to the optical or dark-field image, which makes correlations difficult. To compare milk ducts containing calcifications, their expected area in the dark-field and transmission is marked. Region 1 contains diffuse calcifications that range in sizes of a few µm to up to ≈ 37 µm, as shown in Figure 60a. This region does not yield a

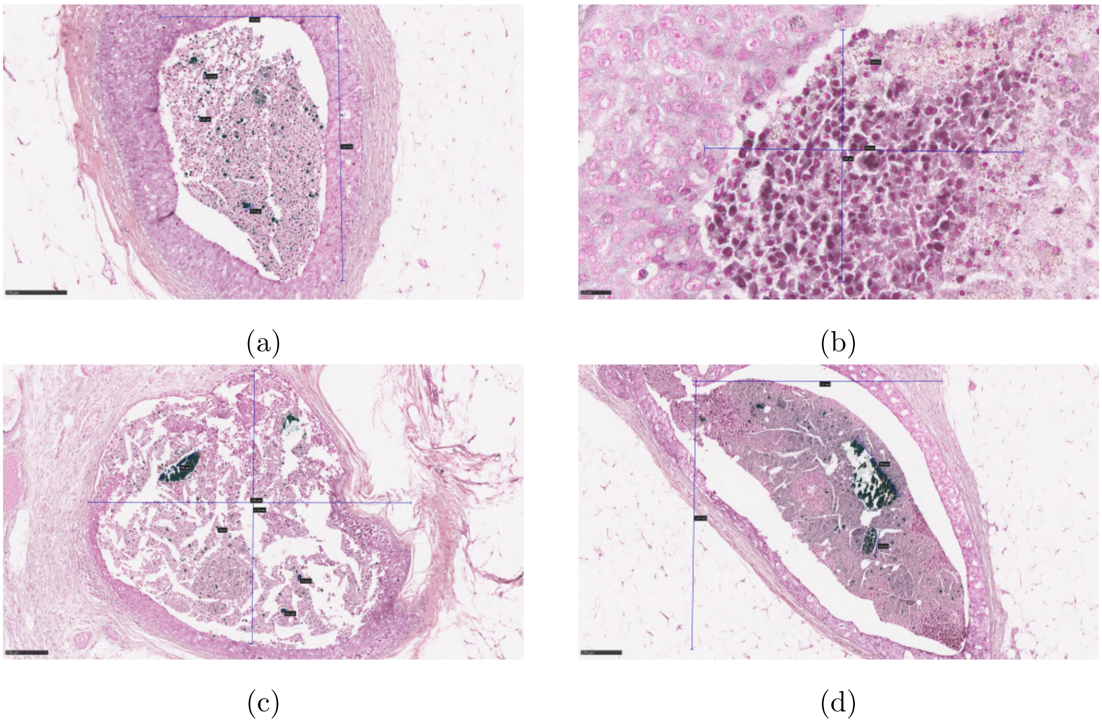

Figure 60: 90° rotated Von-Kossa-stained section close-ups of region 1 (a), region 2 (b), region 3 (c), and region 4 (d) marked in Figure 59a.

corresponding dark-field signal, but shows a slight increase in transmission signal. A similar transmission signal is in region 2, which could correspond to a milk duct shown in Figure 60b. However, this region yields either no calcifications or only very diffuse calcifications that cannot be clearly identified by their color with diameters less than 600 nm. Therefore, this region should not contain any measurable calcifications, and the signal originates most likely from slightly denser tissue.

Region 3 contains several larger calcifications that are visible in both the dark-field and transmission images and can be approximately matched to Figure 60c. This shows a large calcification with a length of 290 µm, but also several calcifications that appear torn. Additionally, there are many longer sharp white areas that indicate tearing during the section cut. Since in the Von-Kossa-stained section some calcifications have a much larger signal area in the transmission and dark-field, during the section cut some calcifications could broken out to only remain in the paraffin block. The opposite of this, is also expected to happen for some cases. In Region 4 only a larger calcification is visible in the dark-field and transmission, but two larger calcifications are in the Von-Kossa-stained section as illustrated in Figure 60d. This could either be due to the spatial resolution of the CT, tears in the stained section or the spatial distance between the stained section and the surface. In region 5, a larger calcification is visible in dark-field and transmission, which is shown in detail in Figure 61. Unusually, this is not surrounded by a milk duct, which could also just be because of a larger tear.

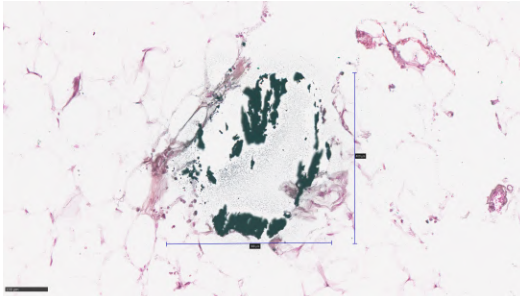

Figure 61: Von-Kossa-stained section close-up of region 5 marked in Figure 59a.

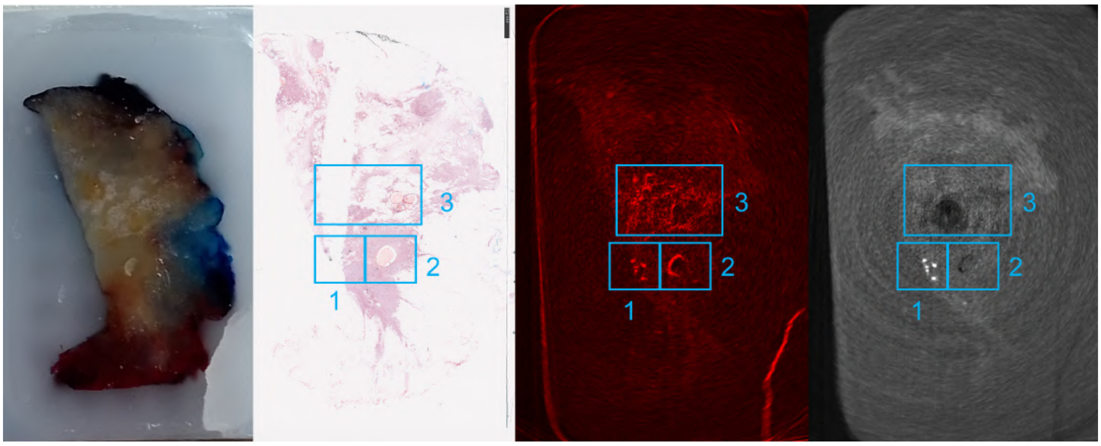

(a) (b) (c) (d)

Figure 62: Optical image (a), Von-Kossa-stained section (b), dark-field image (c), and transmission image (d) of Sample 6. For the dark-field and transmission images, a maximum slab of the paraffin surface with a thickness of 180 µm from the CT-reconstructed volume is shown.

Sample 7

The comparison of the Von-Kossa-stained section with the dark-field and transmission image of Sample 7 is shown in Figure 62. The optical image is shown in Figure 62a, the Von-Kossa-stained section in Figure 62b, the dark-field in 62c and the transmission image in 62d. The Von-Kossa-stained section shows a tear starting exactly at location of several calcifications, which makes an exact comparison largely impossible.

Those calcifications can also be identified in region 1 of the dark-field and transmission image. Furthermore, the edge of a milk duct in the in the Von-Kossa-stain can be seen in the dark-field in region 2, which has a lower transmission signal, indicating a possible air-gap in the milk duct. In region 3, a larger structure is visible uniquely in the dark-field. In the Von-Kossa-stained section, there is mostly fat tissue and no calcifications. This dark-field structure continues through the whole sample in this region, so surface roughness can be excluded as its origin. Another explanation could be tissue not being perfectly embedded in paraffin, but its exact cause could not be identified.

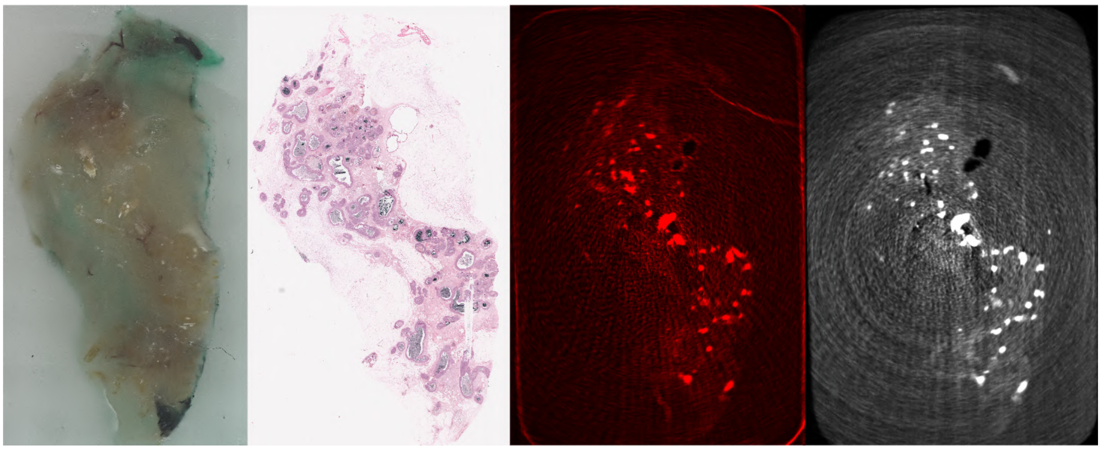

(a) (b) (c) (d)

Figure 63: Optical image (a), Von-Kossa-stained section (b), dark-field image (c), and transmission image (d) of Sample 10. For the dark-field and transmission images, a maximum slab of the paraffin surface with a thickness of 180 µm from the CT-reconstructed volume is shown.

Sample 10

The comparison of the Von-Kossa-stained section with the dark-field and transmission image of Sample 10 is shown in Figure 63. The optical image is shown in Figure 63a, the Von-Kossa-stained section in Figure 63b, the dark-field in 63c and the transmission image in 63d. The correlation of calcifications with dark-field and transmission signals are presented in detail with an additional measurements with adjusted parameters in Chapter 7.3.1.

Sample 12

A comparison of the Von-Kossa-stained section with the dark-field and transmission images of Sample 12 is shown in Figure 64. The optical image is shown in Figure 64a, the Von-Kossa-stained section in Figure 64b, the dark-field image in Figure 64c, and the transmission image in Figure 64d. The correlation of calcifications with dark-field and transmission signals continued in Chapter 7.3.2.

Sample 13

A comparison of the Von-Kossa-stained section with the dark-field and transmission images of Sample 13 is shown in Figure 65. The optical image is shown in Figure 65a, the Von-Kossa-stained section in Figure 65b, the dark-field image in Figure 65c, and the transmission image in Figure 65d. The correlation of calcifications with dark-field and transmission signals continued in Chapter 7.3.3.

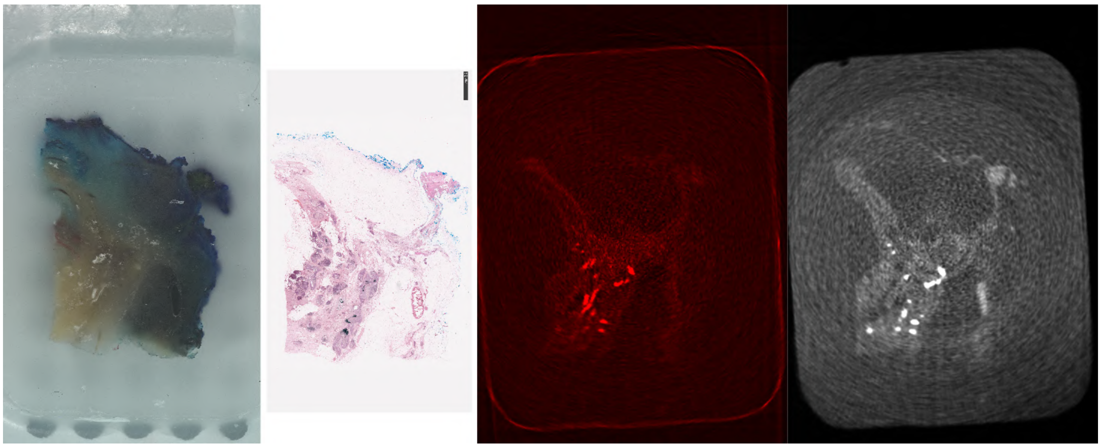

(a) (b) (c) (d)

Figure 64: Optical image (a), Von-Kossa-stained section (b), dark-field image (c), and transmission image (d) of Sample 12. For the dark-field and transmission images, a maximum slab of the paraffin surface with a thickness of 180 µm from the CT-reconstructed volume is shown.

7.3 Correlation of Von-Kossa-stained sections with dark-field and transmission signals

In this chapter are the calcifications in the Von-Kossa-stained section directly correlated with the dark-field and transmission signals by creating an overlayed image of them. For this purpose, the promising samples 10, 12, and 13 were remeasured with improved parameters. First, a sample holder was used that allows the surface of the sample to be perpendicular to the holder instead of parallel. This shifts the ring artifacts of the CT reconstruction from the observed surface to the height of the sample. The disadvantages of this sample position are an effectively smaller field of view and a larger variation in the X-ray path length through the sample, which could cause beam hardening artifacts. The reduced field of view only does not contain the full tissue for Sample 10 and no significant beam hardening artifacts were observed. Secondly, the measurement time was substantially increased using the measurement parameters $U = 39\,\mathrm{kVp}$, $\mathrm{Th} = 20\,\mathrm{keV}$, $I = 16\,\mathrm{mA}$, $t = 30\,\mathrm{s}$, $a_{\mathrm{step}} = 0.2°$, $a_{\mathrm{sector}} = 360°$ and 7 phase-steps with 5 per G_0-period. This results in an overall measurements of $\approx 928\,\mathrm{min}$. All dark-field and transmission images were 180 µm thick maximum slabs of the surface, whereas this partially contains the free field, which is invisible in maximum slabs, and allows the illustration of the whole surface.

7.3.1 Overlay Sample 10

The dark-field image used for the overlay, with the positions marked in red for calculating the transformation matrix, is shown in Figure 66a, and the corresponding transmission image in Figure 66b. The Von-Kossa-stained section with the corresponding positions marked in red is shown in Figure 66c. The positions were determined using clearly identifiable corresponding structures in both images, while maximizing the distance between them to reduce the relative error. Then the points are adjusted to ensure

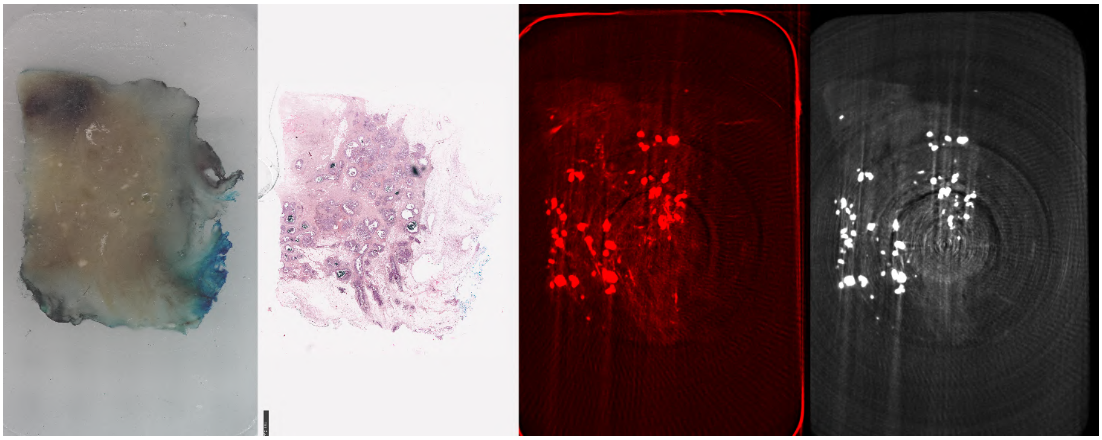

(a) (b) (c) (d)

Figure 65: Optical image (a), Von-Kossa-stained section (b), dark-field image (c), and transmission image (d) of Sample 13. For the dark-field and transmission images, a maximum slab of the paraffin surface with a thickness of 180 µm from the CT-reconstructed volume is shown.

equal scaling of the transformation matrix in the x- and y-directions. Before overlaying, the dark-field image was colored red, and the values below a certain threshold in both the dark-field and transmission images removed to highlight high-signal structures and remove paraffin-related signals. Through this cut off correlated objects can be well displayed, but some signals or contrasts can be overstated. As such after correlation the dark-field and transmission signal should be compared individually. The resulting overlay of the images is shown in Figure 66d. Two areas are marked in the overlay image and are investigated in greater detail below. The upper left is the area with the overlay matched area, since a well matching overlay could only be created for the upper left and lower left area individually and not the full area. The second area was selected because it yields the most significant dark-field signal without a transmission signal. The upper left area is shown in Figure 67 with the object marked depending on whether they are identifiable in dark-field and transmission.

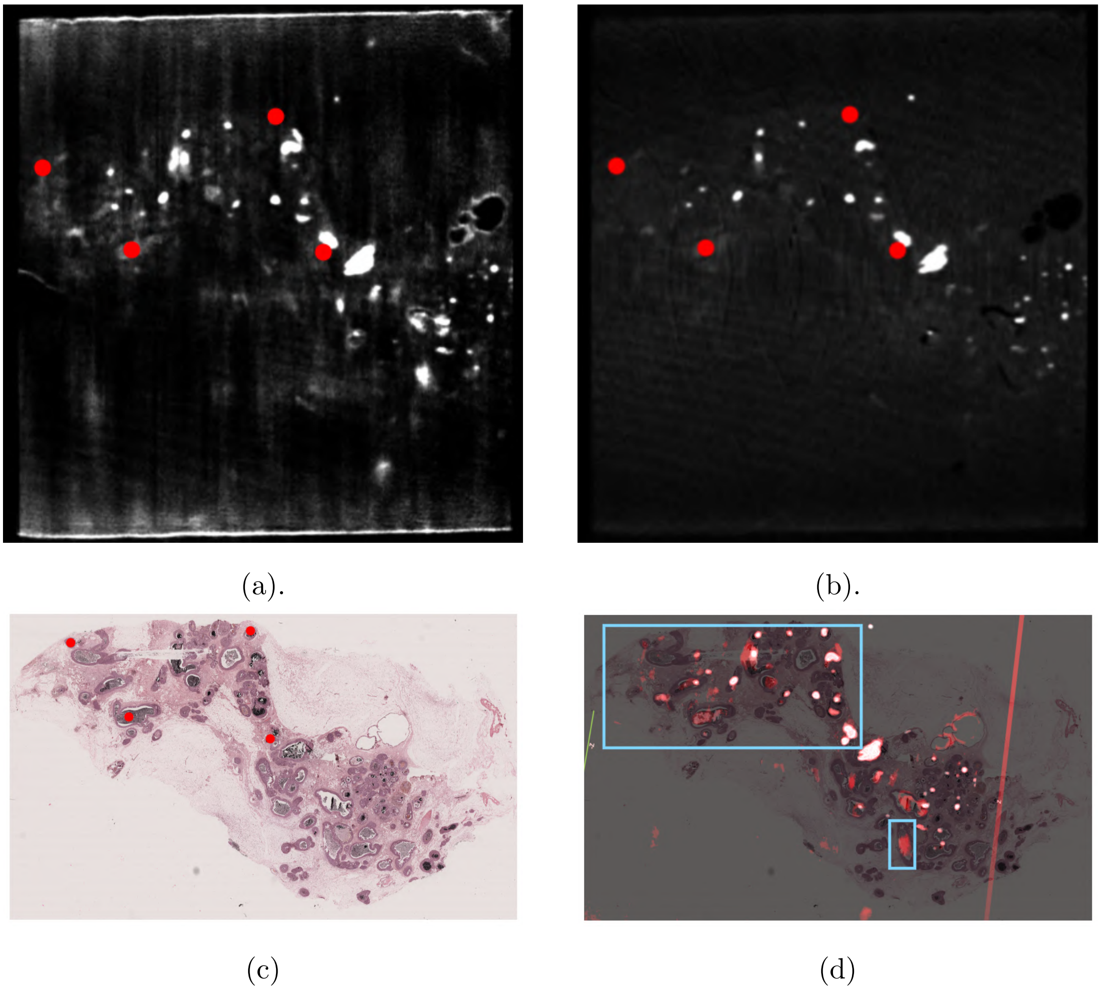

Figure 66: (a) Dark-field maximum slab and (b) transmission maximum slab used for an overlay with (c) the Von-Kossa-stained section of sample 10. (d) The resulting overlay with the dark-field colored (red) and transmission (white).

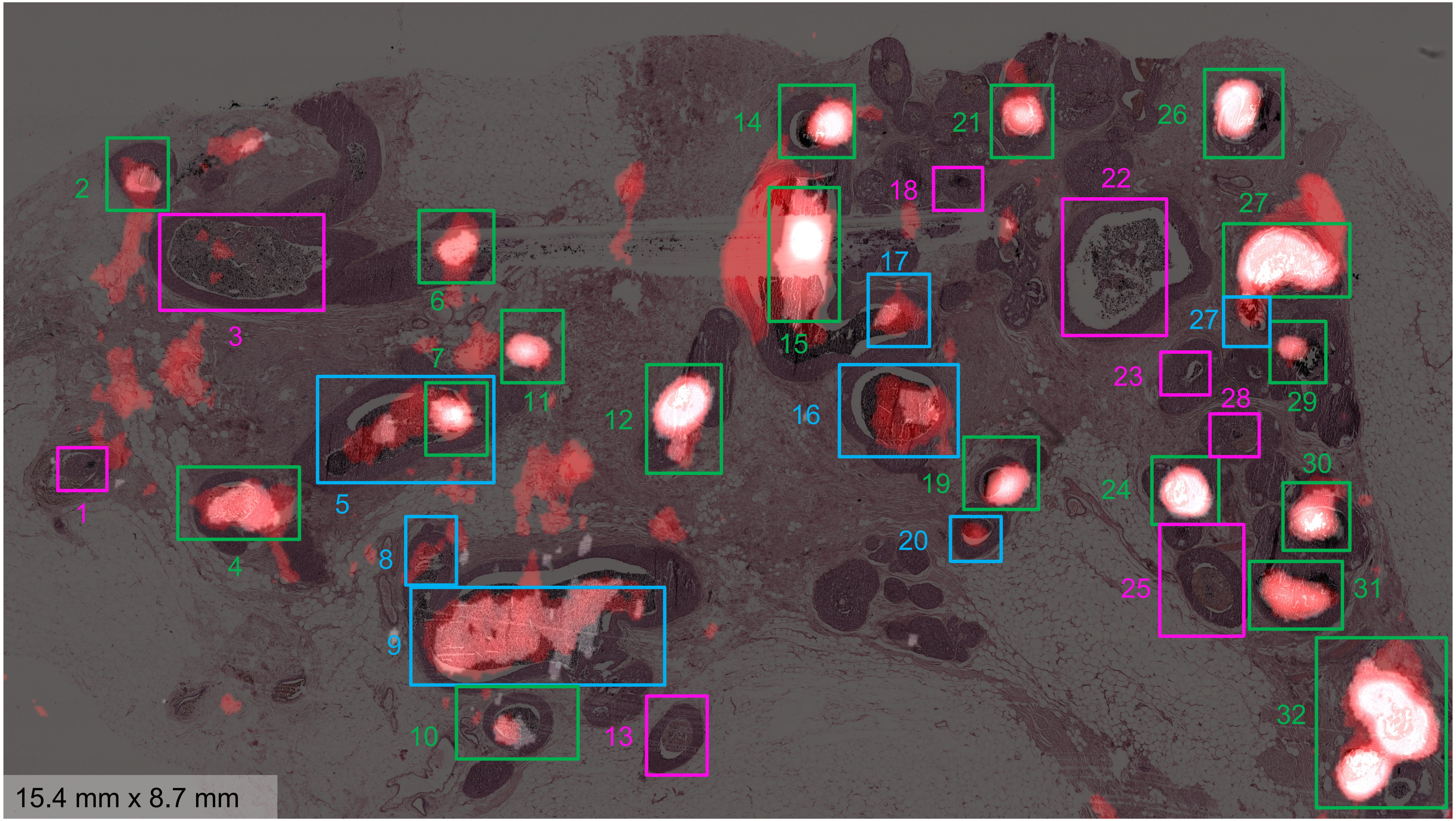

Figure 67: Upper left area of the Von-Kossa-stained section of sample 10 overlaid with the dark-field (red) and transmission (white). Larger clearly identifiable calcifications are marked according to their measured dark-field and transmission signal. Green indicates objects clearly visible in both dark-field and transmission, blue indicates objects visible in dark-field but not clearly identifiable as calcifications in transmission, and pink indicates regions without significant dark-field or transmission signal.

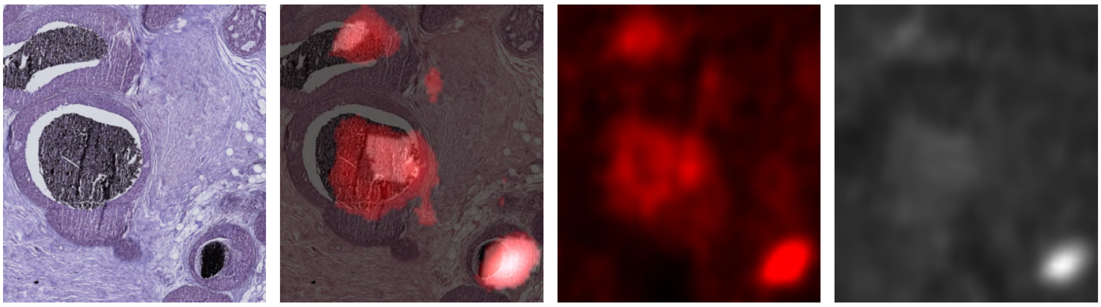

(a) (b) (c) (d)

Figure 68: Close-up view of Objects 16, 17, and 19 in the Von-Kossa-stained section (a), overlay image (b), dark-field image (c), and transmission image (d).

Green rectangles indicate objects that are clearly visible in both the dark-field and transmission images. Blue rectangles indicate objects that are clearly visible in the dark-field image but cannot be reliably identified as calcifications in the transmission image, and pink rectangles indicate calcifications visible in the Von-Kossa-stained section that do not produce significant dark-field or transmission signals. 32 clear identifiable regions could be found in this $15.4\,\mathrm{mm} \times 8.7\,\mathrm{mm}$ area from which several representative cases of objects are further evaluated.

First, to demonstrate the differences between the objects marked blue and green, the region containing objects 16, 17 and 19 is shown as a close-up in different modalities in Figure 68. Figure 68a shows the Von-Kossa-stained section, Figure 68b the overlay image, Figure 68c the dark-field image, and Figure 68d the transmission image.

Object 19 contains very dense calcifications that appear nearly solid, which does not allow a proper size estimation of its calcifications, and is well visible in both dark-field and transmission. In contrast, Object 16 and Object 17 only have a small area with both dark-field and transmission signal in the overlayed image, whereas the signal in the transmission is overstated due to the cut-off of values in the overlayed image. Only small parts of the objects have values above the threshold that removes paraffin signals. Therefore, they do not have a significant contrast and could not be properly identified. In addition, to the dark-field signal having a much larger contrast, also their signal area is much larger. Object 17 contains diffuse calcifications of up to $\approx 10\,\mu\mathrm{m}$, whereas Object 16 contains diffuse calcifications of up to $\approx 20\,\mu\mathrm{m}$ with a non-circular larger calcification with a maximum diameter of $\approx 62\,\mu\mathrm{m}$.

Another example of this is Object 5, which is presented rotated by $90°$ in Figure 69. Figure 69a shows the Von-Kossa-stained section, Figure 69b shows the overlaid image, Figure 69c shows only the dark-field image, and Figure 69d shows only the transmission image. This shows a high-contrast signal in dark-field and transmission continued by a tail only visible in the dark-field. A second area with a transmission signal is also visible in the overlay image. However, this would not be identifiable from the transmission image alone. At the location of the high-contrast signal there are tears in the Von-Kossa-stained section so its calcification composition is unknown and the tail has calcification diameters of up to $\approx 13\,\mu\mathrm{m}$.

Among the objects not yielding a dark-field and transmission signals, Objects 3 and 22 are investigated as they were the largest ones. Objects 1, 18, 23, 28 have so few

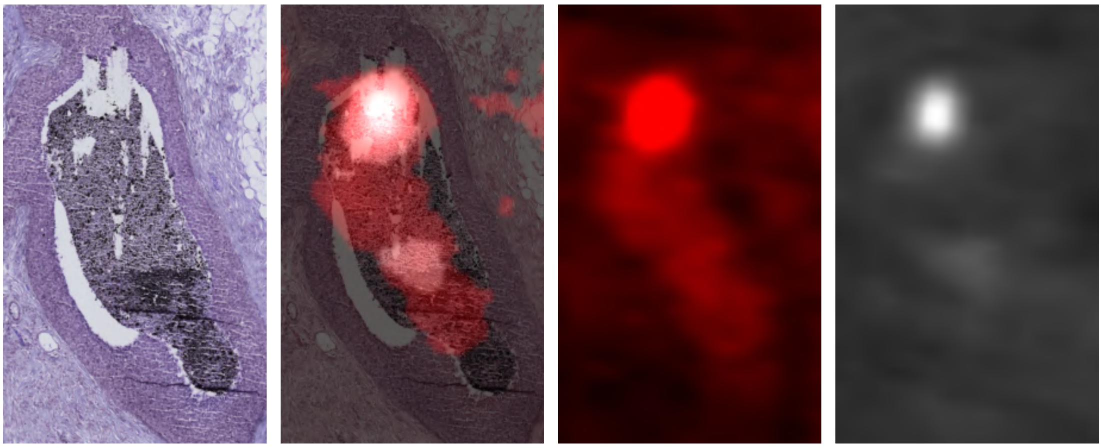

(a) (b) (c) (d)

Figure 69: Close-up view of Object 5 in the Von-Kossa-stained section (a), overlay image (b), dark-field image (c), and transmission image (d).

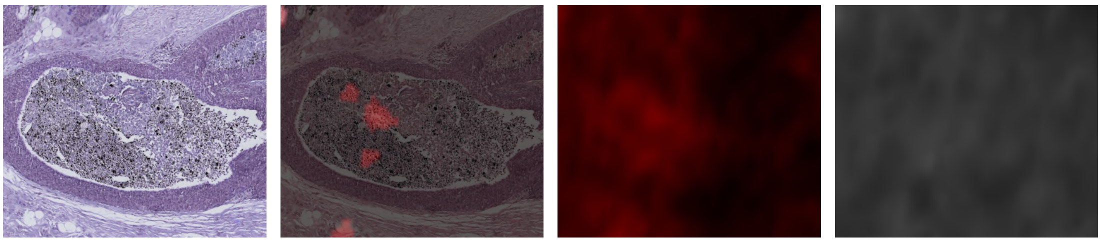

(a) (b) (c) (d)

Figure 70: Close-up view of Object 3 in the Von-Kossa-stained section (a), overlay image (b), dark-field image (c), and transmission image (d).

calcifications that no signal is necessarily expected.

Object 3 is shown in Figure 70. Figure 70a shows the Von-Kossa-stained section, Figure 70b shows the overlaid image, Figure 70c shows only the dark-field image, and Figure 70d shows only the transmission image. This shows no significant signal corresponding to the object in the dark-field and transmission. In the dark-field some areas are above the threshold, but its signal is below other uncorrelated signals. Hence, it cannot be identified as in the dark-field detected calcification object. This object contained diffuse calcifications of up to $\approx 26\,\mu m$.

Object 22 is presented in Figure 71. Figure 71a shows the Von-Kossa-stained section, Figure 71b shows the overlaid image, Figure 71c shows only the dark-field image, and Figure 71d shows only the transmission image. This shows no significant signal corresponding to the object in the dark-field and transmission, and contained calcifications of up to $\approx 15\,\mu m$, while the calcifications in this object were the most spread out, or least dense compared to the other investigated objects.

Finally, the object marked lower right area of Figure 66 is presented. This is outside of the matched overlay, but can still be decently correlated. This area was only selected because it exhibits a significant dark-field signal without a corresponding transmission

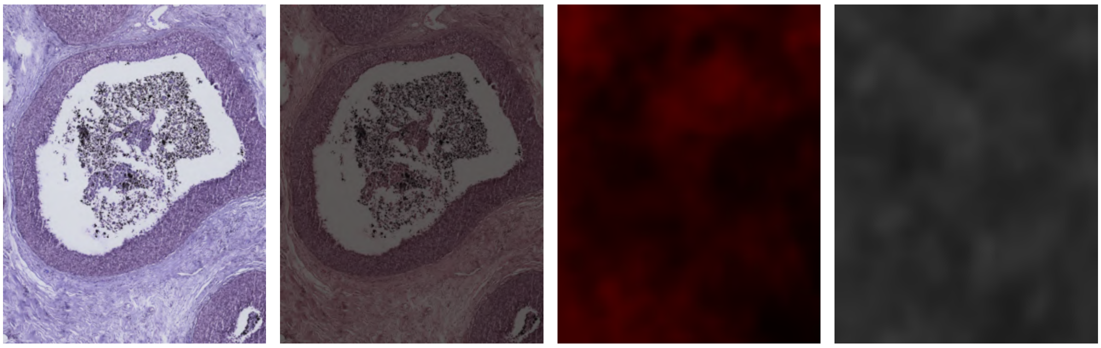

(a) (b) (c) (d)

Figure 71: Close-up view of Object 22 in the Von-Kossa-stained section (a), overlay image (b), dark-field image (c), and transmission image (d).

signal. It is presented in Figure 72, whereas Figure 71a shows the Von-Kossa-stained section, Figure 71b shows the overlaid image, Figure 71c shows only the dark-field image, and Figure 71d shows only the transmission image. This shows a significant dark-field signal and no transmission signal. The transmission image shows a darker line structure, which could indicate an air-gap, but it does not match the dark-field signal. Therefore, it is assumed that the dark-field signal originates from the calcifications, which have diameters of up to $\approx 25\,\mu\text{m}$

7.3.2 Overlay Sample 12

Similarly to Sample 10, a well matching overlaid image could be created for Sample 12 using the Von-Kossa-stained section in Figure 73a, the dark-field image in Figure 73b, and the transmission image in Figure 73c. For this longer measurement, the sample position has not yet been adjusted. As such, ring artifacts are still visible in the reconstructed plane. The resulting overlaid image is shown in Figure 74. This overlaid image contains many objects with calcifications that can be correlated to a dark-field and transmission signal. However, no significantly different object compared to the calcification objects in Sample 10 is found. Therefore, none are presented in detail.

7.3.3 Overlay Sample 13

A well matching overlaid image could be created for Sample 13 using the Von-Kossa-stained section in Figure 75a, the dark-field image in Figure 75b, and the transmission image in Figure 75c. The resulting overlaid image is shown in Figure 76. This shows many calcifications that can be correlated with the dark-field and transmission, which has compared to Sample 10 a trend of having more solid calcifications. To investigate such trends, it might be interesting to analyze the stages of cancer. Only the object marked in blue yields a signal that differs from those observed in Sample 10. The corresponding Von-Kossa-stained section is shown in detail in Figure 77a, the overlay image in Figure 77b, the dark-field image in Figure 77c, and the transmission image in Figure 77d. This object exhibits a strong dark-field signal over a broad area, while only minor amounts of calcifications are in the two milk ducts at the bottom of the image. These calcifications alone are unlikely to explain such a strong dark-field signal inside

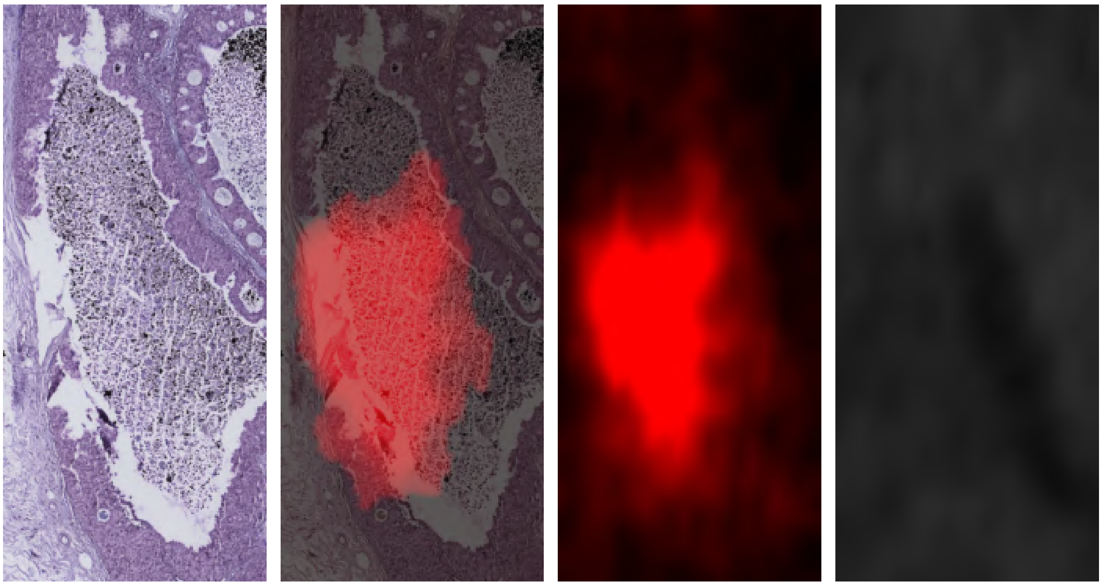

(a) (b) (c) (d)

Figure 72: Close-up view of the right area marked in Figure 66d in the Von-Kossa-stained section (a), overlay image (b), dark-field image (c), and transmission image (d).

the milk ducts. Therefore, either the dark-field signal is caused by surface roughness, which might also be directly caused by empty milk ducts, or the calcifications were torn in the Von-Kossa-stained section. In the middle of the right side, there is a larger calcification with higher contrast in the transmission image.

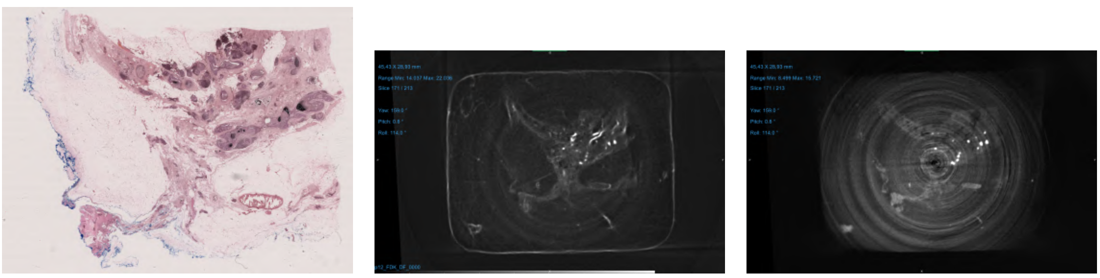

(a). (b). (c).

Figure 73: (a) Von-Kossa-stained section of Sample 12. 180 µm maximum slab of the dark-field (b) and transmission (c) paraffin surface.

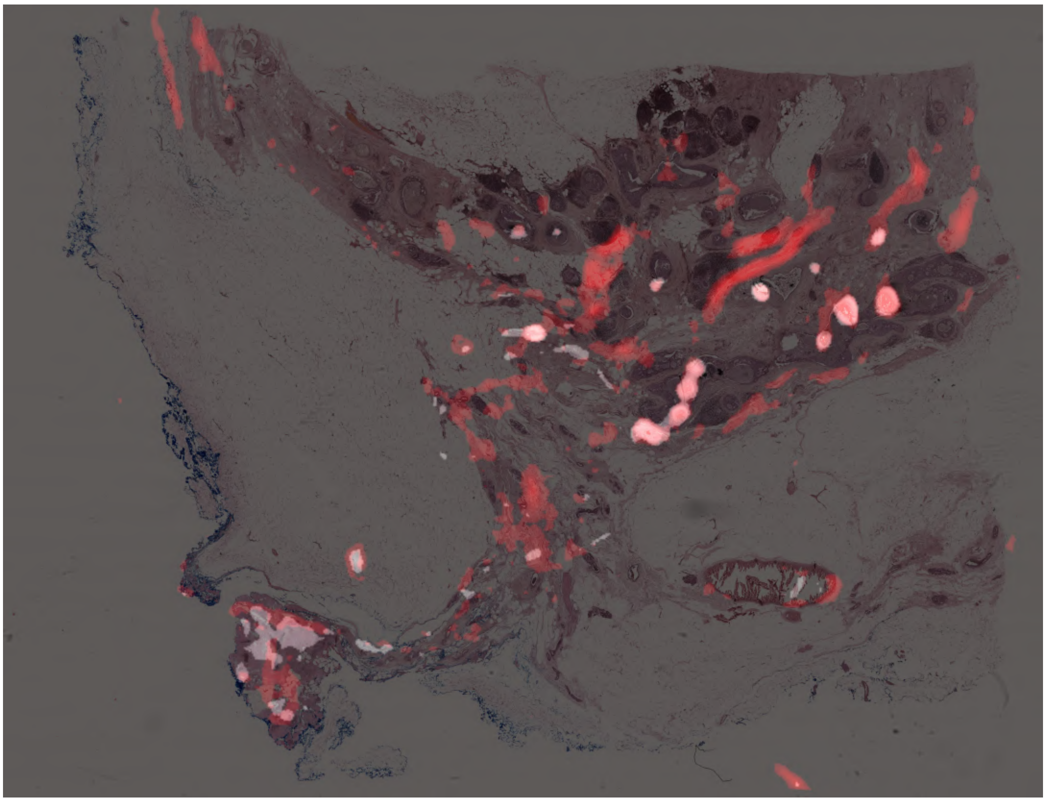

Figure 74: Overlaid image of the images presented in Figure 73. Dark-field signals above a threshold are marked red and transmission signals white.

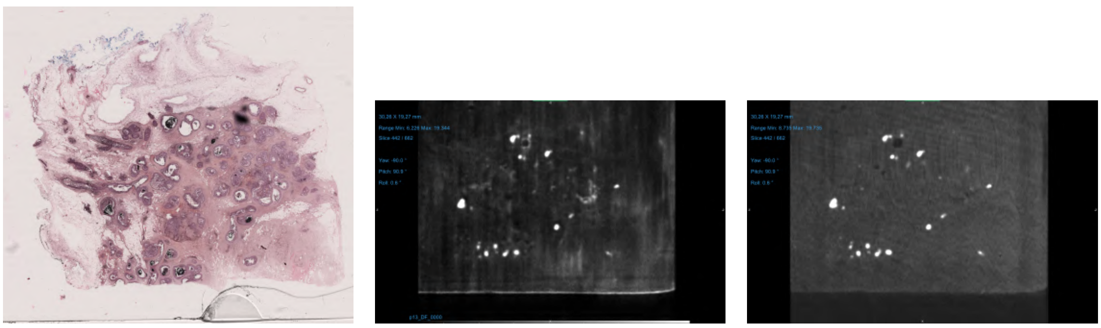

(a). (b). (c).

Figure 75: (a) Von-Kossa-stained section of Sample 13. 180 µm maximum slab of the dark-field (b) and transmission (c) paraffin surface.

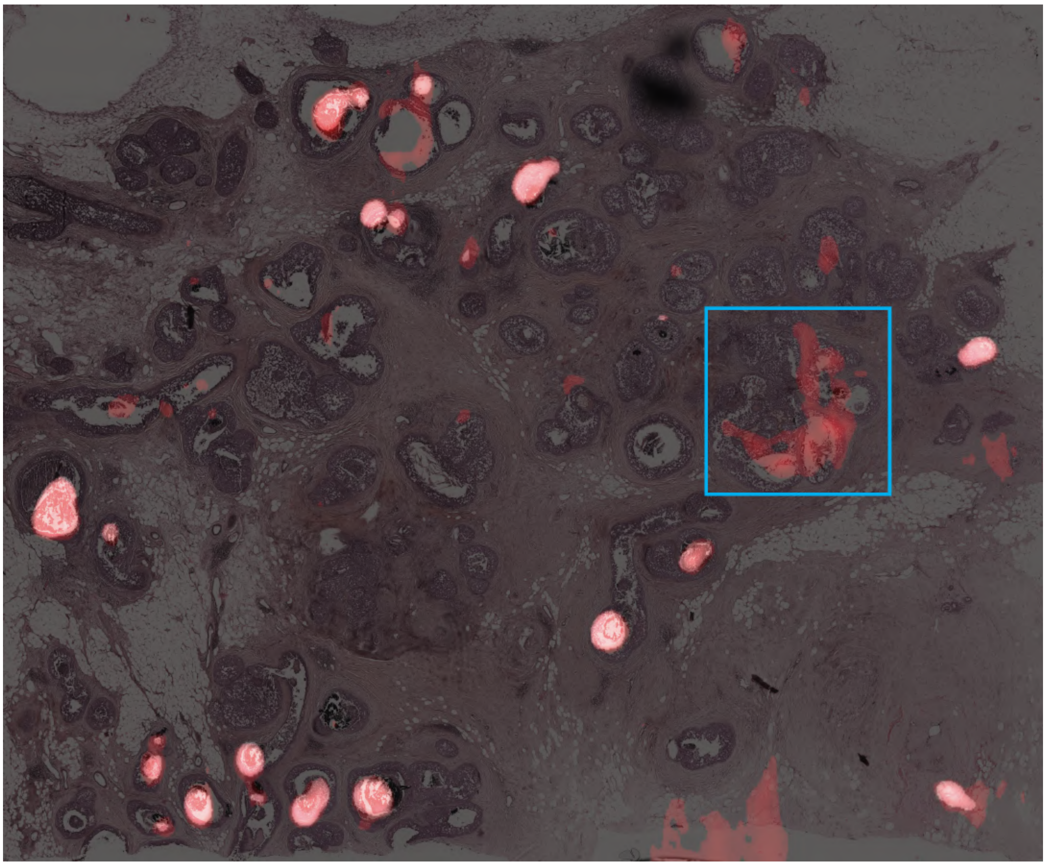

Figure 76: Overlaid image of the images presented in Figure 75. Dark-field signals above a threshold are marked red and transmission signals white.

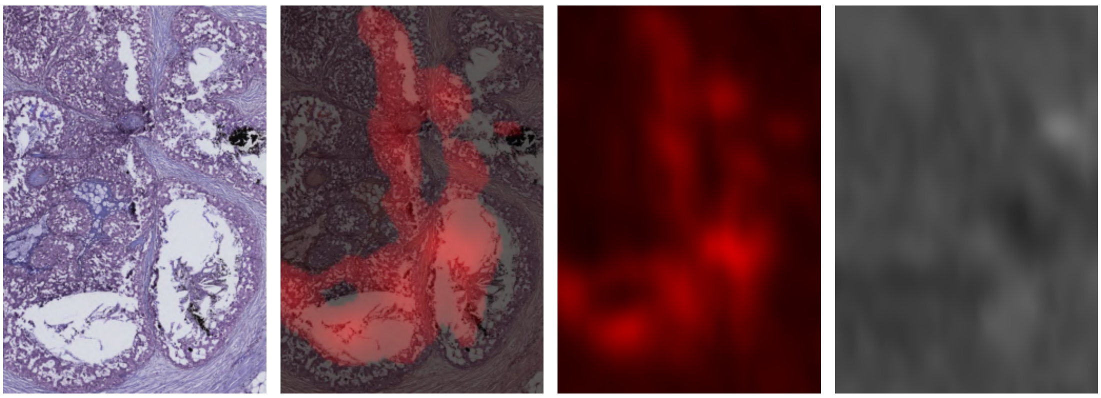

(a) (b) (c) (d)

Figure 77: Close-up view of the area marked in Figure 7.3.3 in the Von-Kossa-stained section (a), overlay image (b), dark-field image (c), and transmission image (d).

7.4 Object sizes in Sample 13

In this chapter, the size distribution of calcifications within Sample 13 is analyzed. For this purpose, regions within the 3D paraffin volume obtained from the CT reconstruction with transmission signals above a certain threshold were classified as objects. A slice of the transmission CT reconstruction, cut to the tissue region, is shown in Figure 78a. The corresponding classified object with the background removed is shown in Figure 78b. Selecting objects from the transmission reconstruction removes any false

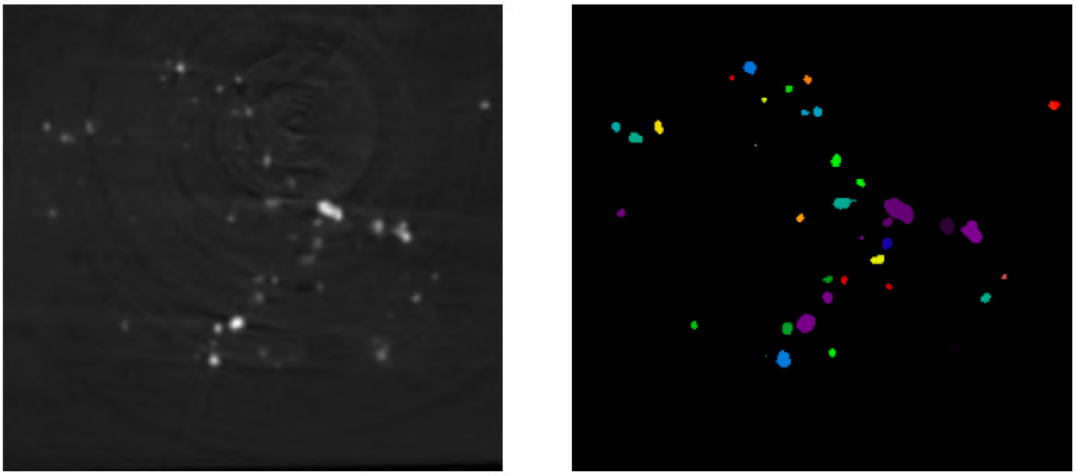

(a). (b).

Figure 78: (a) Slice of the reconstructed transmission volume. (b) Detected objects above a threshold, with each object marked in a different color.

classification of tears in the paraffin, surface roughness, and air-bubbles, but may also exclude calcifications only visible in the dark-field. Since no ground truth inside the paraffin block exists, such dark-field signals can only be excluded for special cases, such as line-like tears in the paraffin.
An example of a selected object is shown in Figure 79, whereas each sub-figure presents a different plane through the center of the classified object.

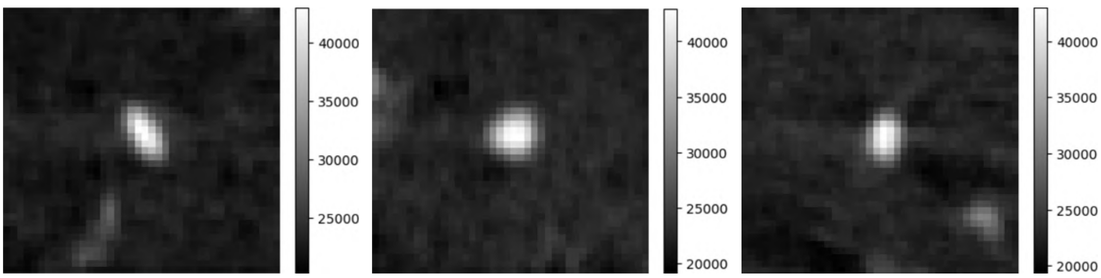

(a). (b). (c).

Figure 79: Images of planes through an object for the reconstructed dark-field volume for the xy-plane (a), the yz-plane (b), the xz-plane (c).

Using the same coordinates, a line plot is determined for every plane through the center and smoothed with a Savitzky-Golay filter. This is done for both dark-field and transmission values, whereas for the dark-field a Gaussian fit is applied to determine its width, as shown in Figure 80. The Gaussian fit used was [Squ01]

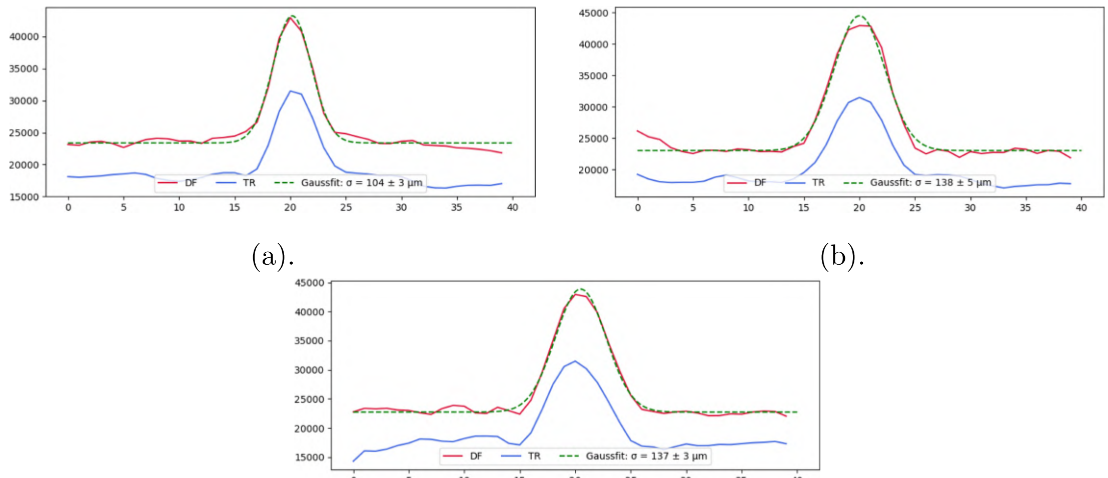

(a). (b).

(c).

Figure 80: Line plots through the center of an object for the reconstructed dark-field and transmission volume for the x-direction (a), the y-direction (b), the z-direction (c). The lines were smoothed by a Savitzky-Golay filter and a Gauss-fit was applied to the dark-field object.

$$f(x) = A \exp\left(-\frac{(x-\mu)^2}{2\sigma^2}\right), \tag{50}$$

where A is the amplitude, σ the width and μ the peak position. The widths determined for each plane are shown in a histogram in Figure 81. Figure 81a presents the width in the x-direction, Figure 81b the width in the y-direction, and Figure 81c the width in the z-direction.

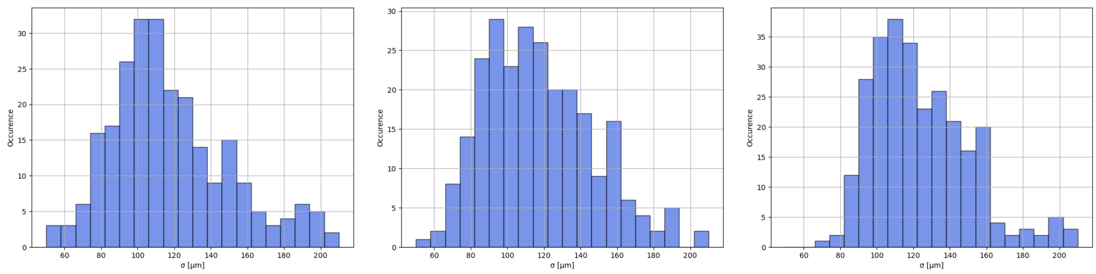

(a). (b). (c).

Figure 81: Histogram of the widths determined by a Gauss-fit of calcification objects within Sample 13. (a) Distribution of widths in x-direction, (b) distribution of widths in y-direction, and (c) depicts the distribution of widths in z-direction.

The histograms of each direction show significantly different distributions, indicating that most calcifications are not spherical.

Discussion of paraffin sample results

Using the Von-Kossa-stained sections as ground truth the main problem of the formalin samples could be addressed. The Von-Kossa-stained sections are not within the measured sample, but next to it, which could introduce differences in the resulting correlation. The dark-field and transmission reconstruction of samples 10, 12, and 13 could be well correlated to the Von-Kossa-stained section. In the correlation of those, calcification objects visible in transmission and dark-field, visible only in dark-field, with higher contrast in transmission, and not visible in both could be found. From the nine samples six could not be well correlated to due to tears in the Von-Kossa-stained section, tears inside the paraffin embedding of the tissue, surface roughness, and air-transitions contaminating the dark-field signal. Since for some samples, the paraffin embedding the tissue showed strong contamination of tears, surface roughness, and air-transitions also visible in the dark-field signal, a determination of calcification without the Von-Kossa-stained section is prone to false positives, and a ground truth necessary till a proper discrimination is established.

8 Conclusion

This thesis demonstrates the experimental optimization of a grating-based dark-field CT system and evaluation of breast cancer samples provided by the "Pathologie Uniklinikum Erlangen". This was motivated by the limited sensitivity of conventional X-ray imaging to microstructures such as microcalcifications, commonly found in DCIS and invasive breast cancer, and the increased sensitivity of the dark-field modality to detect them.
In Chapter 5 two different grating setups were used, and their acquisition parameters and signal quality in the form of the visibility systematically investigated. No clear optimum and only compromises for a specific parameter could be determined, with exception of the focal spot size, where the improved spatial resolution of $f = 1\,\mathrm{mm}$ results in clearly better images. Using phase-stepping scans the tube voltage and threshold were determined by the highest counts a visibility of $\approx 30\%$. For the frame time, the standard deviation in the free-field of a dark-field image did not decrease exactly as with a Poisson-statistics expected. The phase-stepping scan configuration of 7 phase-steps with 5 per G_0-period was selected, as it lead to a sufficiently decreased the standard-deviation of its visibility compared to 6 phase-steps with 5 per G_0-period. The standard-deviation decreases with more phase-steps, but this also further increases the scan time, and a compromise between standard-deviation of the visibility and scan time has to be chosen. Furthermore, using CT reconstruction, the impact of angle step size, angle sector, and frame time on the SNR of a aluminum-oxide powder region was compared, which resulted in smaller angle step sizes reaching significantly larger SNRs.
Chapter 6 presents the evaluation of five samples embedded in formalin. Using the scanner to record projection of the top view, resulted in no detection of objects. Using CTs, this showed promising candidates for microcalcifications, but as no exact pathological truth of the samples exists, object with a more pronounced dark-field signal cannot be classified.
In Chapter 7 the limited ground truth was addressed, by correlating histological Von-Kossa-stained sections next to the surface of sample with its surface in the CT reconstruction. From the nine samples only three allowed for a well correlated overlaid image of the stained section and the dark-field and transmission. The well correlated samples showed calcification objects visible in transmission and dark-field, visible only in dark-field, with higher contrast in transmission, and not visible in both. Since for some samples, the paraffin embedding the tissue showed strong contamination of tears, surface roughness, and air-transitions also visible in the dark-field signal, a determination of calcification without the Von-Kossa-stained section is prone to false positives. Further, the Von-Kossa-stained sections of some samples were degraded by tears of the section and break outs of calcifications, which also worsens the correlation to the imaging modalities.
In conclusion, this thesis establishes the experimental basis for the evaluation of pathological samples using dark-field CT. Using CT measurements, the locations of calcifications could be determined in the dark-field and transmission modality. By comparison to Von-Kossa-stained sections diffuse calcification clouds only identifiable in the dark-field could be found. For future clinical applications, analyzing dark-field reconstructions without an underlying ground truth creates the challenge to reliably differentiate microcalcifications and without increasing the number of false positives.

Bibliography

[Ami+22] A. Aminzadeh et al. “Imaging Breast Microcalcifications Using Dark-Field Signal in Propagation-Based Phase-Contrast Tomography”. In: *IEEE Transactions on Medical Imaging* 41.11 (2022), pp. 2980–2990. DOI: 10.1109/TMI.2022.3175924.

[Ant+13] Gisela Anton et al. “Grating-based dark-field imaging of human breast tissue”. In: *Zeitschrift für Medizinische Physik* 23.4 (2013), pp. 228–235. DOI: 10.1016/j.zemedi.2013.01.001.

[AST25] ASTRA Toolbox Developers. *ASTRA Toolbox*. GPU-accelerated toolbox for 2D and 3D tomography reconstruction. Accessed: 2026-05-31. 2025. URL: https://astra-toolbox.com/.

[Bal25] Nora Balewski. *Qualitätsmessungen eines Talbot-Lau-Scanners und Strukturanalyse mittels Dunkelfeldbildgebung*. Bachelorarbeit aus der Physik. Betreuer: Prof. Dr. Stefan Funk; Abgabedatum: 13.02.2025. Feb. 2025.

[Bec+10] M. Bech et al. “Quantitative x-ray dark-field computed tomography”. In: *Physics in Medicine and Biology* 55.18 (2010), pp. 5529–5539. DOI: 10.1088/0031-9155/55/18/017.

[BS23] Julien Berta and David Sarrut. “Monte Carlo Simulations”. In: *Computational Nuclear Oncology and Radiomics*. CRC Press, 2023.

[Buz08a] Thorsten M. Buzug. *Computed Tomography: From Photon Statistics to Modern Cone-Beam CT*. Berlin, Heidelberg: Springer, 2008.

[Buz08b] Thorsten M. Buzug. *Computed Tomography: From Photon Statistics to Modern Cone-Beam CT*. Berlin, Heidelberg: Springer, 2008.

[Com26] Comet Technologies Canada Inc. *Dragonfly 3D View*. 3D visualization, rendering, and animation software for volumetric imaging data. Accessed: 2026-05-31. 2026. URL: https://dragonfly.comet.tech/en/products/dragonfly-3d-view.

[Fri25] Luca Fritsch. “Development of image acquisition and alignment methods for X-ray dark-field and phase-contrast imaging”. Master thesis. Erlangen, Germany: Erlangen Centre for Astroparticle Physics, Department of Physics, Friedrich-Alexander-Universität Erlangen-Nürnberg, 2025.

[Gre08] Walter Greiner. *Klassische Elektrodynamik*. Theoretische Physik, Band 3. Frankfurt am Main: Wissenschaftlicher Verlag Harri Deutsch, 2008.

[Hel+18] Katharina Hellbach et al. “X-Ray Dark-field Imaging to Depict Acute Lung Inflammation in Mice”. In: *Scientific Reports* 8 (2018), p. 2096. DOI: 10.1038/s41598-018-20358-5.

[HGD93] B. L. Henke, E. M. Gullikson, and J. C. Davis. “X-Ray Interactions: Photoabsorption, Scattering, Transmission, and Reflection at E = 50–30,000 eV, Z = 1–92”. In: *Atomic Data and Nuclear Data Tables* 54.2 (1993), pp. 181–342. ISSN: 0092-640X. DOI: 10.1006/adnd.1993.1013.

[Kae+17] S. Kaeppler et al. “Improved reconstruction of phase-stepping data for Talbot-Lau x-ray imaging”. In: *Journal of Medical Imaging* 4.3 (2017), p. 034005. DOI: 10.1117/1.JMI.4.3.034005.

[Koe+16] T. Koenig et al. “On the origin and nature of the grating interferometric dark-field contrast obtained with low-brilliance x-ray sources”. In: *Physics in Medicine and Biology* 61.9 (2016), p. 3427. DOI: 10.1088/0031-9155/61/9/3427.

[Kri12] Hanno Krieger. *Grundlagen der Strahlungsphysik und des Strahlenschutzes*. 4th ed. Wiesbaden: Vieweg+Teubner Verlag, 2012. ISBN: 978-3-8348-2238-3. DOI: 10.1007/978-3-8348-2238-3.

[KS01] Avinash C. Kak and Malcolm Slaney. *Principles of Computerized Tomographic Imaging*. Philadelphia: SIAM, 2001. DOI: 10.1137/1.9780898719277.

[KS88] Avinash C. Kak and Malcolm Slaney. *Principles of Computerized Tomographic Imaging*. New York: IEEE Press, 1988.

[KS+97] C. Kimme-Smith et al. “Breast calcification and mass detection with mammographic anode-filter combinations of molybdenum, tungsten, and rhodium”. In: *Radiology* 203.3 (June 1997), pp. 679–683. DOI: 10.1148/radiology.203.3.9169688.

[Lau48] E. Lau. “Beugungserscheinungen an Doppelrastern”. In: *Annalen der Physik* 437.7–8 (1948), pp. 417–423. DOI: 10.1002/andp.19484370709.

[Lel+15] Michael M. Lell et al. “Evolution in Computed Tomography: The Battle for Speed and Dose”. In: *Investigative Radiology* 50.9 (2015), pp. 629–644. DOI: 10.1097/RLI.0000000000000172.

[Lud20] Veronika Ludwig. “Development of image acquisition and alignment methods for X-ray dark-field and phase-contrast imaging”. PhD thesis. Erlangen, Germany: Erlangen Centre for Astroparticle Physics, Department of Physics, Friedrich-Alexander-Universität Erlangen-Nürnberg, 2020.

[Lyn+11] S. K. Lynch et al. “Interpretation of dark-field contrast and particle-size selectivity in grating interferometers”. In: *Applied Optics* 50.22 (2011), pp. 4310–4319. DOI: 10.1364/ao.50.004310.

[MIT26] MITOS GmbH. *X-AID: CT Reconstruction Software*. Multi-GPU-based computed tomography (CT) reconstruction software for industrial X-ray imaging. Accessed: 2026-05-31. 2026. URL: https://www.mitos.de/.

[MRA+13] Thilo Michel, Jens Rieger, Gisela Anton, et al. “On a dark-field signal generated by micrometer-sized calcifications in phase-contrast mammography”. In: *Physics in Medicine and Biology* 58.8 (2013), pp. 2713–2732. DOI: 10.1088/0031-9155/58/8/2713.

[Mus+88] G. Musiol et al. *Kern- und Elementarteilchenphysik*. Verlag Harri Deutsch, 1988.

[Pag06] David Paganin. *Coherent X-ray Optics*. Oxford, New York: Oxford University Press, 2006. ISBN: 9780198567288.

[Par07] Ellen Shaw de Paredes. *Atlas of Mammography*. 3rd ed. Rev. ed. of: Atlas of Film-Screen Mammography, 2nd ed. (1992). Lippincott Williams & Wilkins, 2007. ISBN: 978-0-7817-6433-9.

[Pfe+06] F. Pfeiffer et al. "Phase retrieval and differential phase-contrast imaging with low-brilliance X-ray sources". In: *Nature Physics* 2.4 (2006), pp. 258–261. DOI: 10.1038/nphys265.

[Pfe+08] Franz Pfeiffer et al. "Hard X-ray dark-field imaging using a grating interferometer". In: *Nature Materials* 7 (2008), pp. 134–137. DOI: 10.1038/nmat2096.

[Pov+14] Bogdan Povh et al. *Teilchen und Kerne: Eine Einführung in die physikalischen Konzepte*. Springer Spektrum Berlin, Heidelberg, 2014. DOI: 10.1007/978-3-642-37822-5.

[Rad17] Johann Radon. "Über die Bestimmung von Funktionen durch ihre Integralwerte längs gewisser Mannigfaltigkeiten". In: *Berichte über die Verhandlungen der Königlich-Sächsischen Akademie der Wissenschaften zu Leipzig, Mathematisch-Physische Klasse* 69 (1917), pp. 262–277.

[Ray81] L. Rayleigh. "XXV. On copying diffraction-gratings, and on some phenomena connected therewith". In: *The London, Edinburgh, and Dublin Philosophical Magazine and Journal of Science* 11.67 (1881), pp. 196–205. DOI: 10.1080/14786448108626995.

[Rin+73] James M. Rini et al. "A Comparison of Tungsten and Molybdenum as Target Material for Mammographic X-Ray Tubes". In: *Radiology* 106.3 (Mar. 1973), pp. 657–661. DOI: 10.1148/106.3.657.

[Sar+23] Thomas Sartoretti et al. "Photon-counting detector CT: early clinical experience review". In: *British Journal of Radiology* 96.1147 (2023), p. 20220544. DOI: 10.1259/bjr.20220544.

[Sch20] Stephan Schreiner. "Design and Characterization of a Portable Talbot Interferometer for Imaging High Energy Density Experiments". Master's Thesis in Physics. Erlangen, Germany: Erlangen Centre for Astroparticle Physics, Department of Physics, Nov. 2020.

[Sch21] Marlon R. Schneider. "Von Kossa and his staining technique". In: *Cell and Tissue Research* 386.3 (2021). Published online 20 November 2021, pp. 1–3. DOI: 10.1007/s00441-021-03515-2.

[SMJ19] Rebecca L. Siegel, Kimberly D. Miller, and Ahmedin Jemal. "Cancer statistics, 2019". In: *CA: A Cancer Journal for Clinicians* 69.1 (2019), pp. 7–34. DOI: 10.3322/caac.21551.

[Squ01] G. L. Squires. *Practical Physics*. 4th ed. Cambridge University Press, 2001. ISBN: 978-0-521-77940-1. DOI: 10.1017/cbo9781139164498.

[Str14] M. Strobl. "General solution for quantitative dark-field contrast imaging with grating interferometers". In: *Scientific Reports* 4 (2014), p. 7243. DOI: 10.1038/srep07243.

[Tal36] H. Talbot. “Facts relating to optical science”. In: *Philosophical Magazine Series 3* 9.56 (1836), pp. 401–407. DOI: 10.1080/14786443608649032.

[Tra22] Philip Maurice Trapp. “Novel Methods for the Reduction of Systematic and Statistical Measurement Deviations and Spatial Resolution Optimization in X-Ray Computed Tomography”. Dissertation (Dr. rer. nat.) Heidelberg, Germany: Ruprecht Karl University of Heidelberg, 2022.

[Wol16] Andreas Wolf. “Untersuchungen zu einer iterativen CT-Rekonstruktion in der gitterbasierten Röntgenbildgebung”. Master’s Thesis in Physics. Erlangen, Germany: Erlangen Centre for Astroparticle Physics, Department of Physics, Apr. 2016.

[Wor26] World Health Organization. *Breast cancer*. https://www.who.int/news-room/fact-sheets/detail/breast-cancer. Accessed: 2026-05-27. 2026.

[YVM15] W. Yashiro, P. Vagovic, and A. Momose. “Effect of beam hardening on a visibility-contrast image obtained by X-ray grating interferometry”. In: *Optics Express* 23.18 (2015), pp. 23462–23471. DOI: 10.1364/OE.23.023462.

[Zan+11] I. Zanette et al. “Interlaced phase stepping in phase-contrast X-ray tomography”. In: *Applied Physics Letters* 98.9 (2011), p. 094101. DOI: 10.1063/1.3559616.

Declaration of Originality

I, Markus Kraft, student registration number: 22820503, hereby confirm that I completed the submitted work independently and without the unauthorized assistance of third parties and without the use of undisclosed and, in particular, unauthorized aids. This work has not been previously submitted in its current form or in a similar form to any other examination authorities and has not been accepted as part of an examination by any other examination authority.

Where the wording has been taken from other people's work or ideas, this has been properly acknowledged and referenced. This also applies to drawings, sketches, diagrams and sources from the Internet.

In particular, I am aware that the use of artificial intelligence is forbidden unless its use an aid has been expressly permitted by the examiner. This applies in particular to chatbots (especially ChatGPT) and such programs in general that can complete the tasks of the examination or parts thereof on my behalf.

Any infringements of the above rules constitute fraud or attempted fraud and shall lead to the examination being graded "fail" ("nicht bestanden").

Place, Date	Signature